

Simultaneous Measurement of Oscillation Parameters in Beam and Atmospheric Neutrino Data from Tokai-to-Kamioka and Super-Kamiokande Experiments

Daniel Robert Clement Barrow

Magdalen College, Oxford University

¹⁰ A Dissertation Submitted to Oxford University

¹¹ for the Degree of Doctor of Philosophy

¹²

13 **Simultaneous Measurement of**

14 **Oscillation Parameters in Beam and**

15 **Atmospheric Neutrino Data from**

16 **Tokai-to-Kamioka and**

17 **Super-Kamiokande Experiments**

18 *Abstract*

19 Lorem ipsum dolor sit amet, consectetur adipiscing elit, sed do eiusmod tempor incididunt ut labore et dolore magna aliqua. Nulla aliquet porttitor lacus luctus accumsan tortor posuere. Pulvinar neque laoreet suspendisse interdum. Sem viverra aliquet eget sit. Nunc sed velit dignissim sodales ut eu sem integer vitae. At erat pellentesque adipiscing commodo elit at imperdiet dui accumsan. Fames ac turpis egestas integer eget aliquet nibh. Scelerisque eu ultrices vitae auctor eu augue. Purus non enim praesent elementum facilisis leo vel. Sollicitudin nibh sit amet commodo. Vitae auctor eu augue ut. Vel quam elementum pulvinar etiam. A condimentum vitae sapien pellentesque habitant morbi tristique senectus. Viverra accumsan in nisl nisi scelerisque eu ultrices. Sed viverra ipsum nunc aliquet bibendum enim. Sit amet purus gravida quis. In vitae turpis massa

³² sed elementum tempus egestas sed sed. Vivamus arcu felis bibendum
³³ ut tristique et egestas. Senectus et netus et malesuada fames ac turpis.
³⁴ Ac auctor augue mauris augue.

35 Declaration

36 This dissertation is the result of my own work, except where ex-
37 plicit reference is made to the work of others, and has not been sub-
38 mitted for another qualification to this or any other university. This
39 dissertation does not exceed the word limit for the respective Degree
40 Committee.

41 Daniel Robert Clement Barrow

42 ©The copyright of this thesis rests with the author and is made available under a Creative
43 Commons Attribution Non-Commercial No Derivatives licence. Researchers are free to copy,
44 distribute or transmit the thesis on the condition that they attribute it, that they do not use
45 it for commercial purposes and that they do not alter, transform or build upon it. For any
46 reuse or redistribution, researchers must make clear to others the licence terms of this work.

47

Acknowledgements

48 at pretium nibh ipsum. Eget nunc scelerisque viverra mauris in aliquam. Arcu vitae
49 elementum curabitur vitae nunc sed velit dignissim. Sed arcu non odio euismod lacinia
50 at quis risus sed. Vitae tempus quam pellentesque nec nam aliquam sem et tortor.
51 Viverra aliquet eget sit amet tellus cras adipiscing. Purus sit amet luctus venenatis
52 lectus magna. In aliquam sem fringilla ut morbi tincidunt augue. Fermentum dui
53 faucibus in ornare. Aliquam malesuada bibendum arcu vitae elementum curabitur
54 vitae nunc sed.

55 Ultricies leo integer malesuada nunc vel risus commodo. Tellus cras adipiscing
56 enim eu turpis egestas pretium. Dictumst quisque sagittis purus sit amet volutpat
57 consequat mauris nunc. Vitae congue mauris rhoncus aenean vel elit scelerisque
58 mauris pellentesque. Vel facilisis volutpat est velit egestas dui id ornare. Suscipit
59 adipiscing bibendum est ultricies. At in tellus integer feugiat scelerisque varius
60 morbi enim. Cras semper auctor neque vitae tempus. Commodo sed egestas egestas
61 fringilla phasellus faucibus. Cras pulvinar mattis nunc sed blandit. Pretium viverra
62 suspendisse potenti nullam ac tortor vitae. Purus sit amet volutpat consequat. Orci
63 sagittis eu volutpat odio facilisis mauris. Sit amet massa vitae tortor condimentum
64 lacinia quis. Commodo sed egestas egestas fringilla phasellus. Sed libero enim sed
65 faucibus turpis. Vitae tempus quam pellentesque nec.

66 Blandit massa enim nec dui. Viverra tellus in hac habitasse platea dictumst vestibulu-
67 lum. Bibendum enim facilisis gravida neque convallis. Sagittis nisl rhoncus mattis
68 rhoncus urna neque. Nisl rhoncus mattis rhoncus urna neque. Ac tortor vitae purus
69 faucibus ornare. Aenean sed adipiscing diam donec adipiscing tristique risus. Sapien
70 nec sagittis aliquam malesuada bibendum. Et leo duis ut diam quam nulla. Tellus
71 rutrum tellus pellentesque eu tincidunt tortor aliquam nulla facilisi. Fermentum leo

⁷² vel orci porta non pulvinar neque. Eget sit amet tellus cras adipiscing enim eu. Sed
⁷³ viverra tellus in hac habitasse platea dictumst vestibulum.

⁷⁴ Sit amet consectetur adipiscing elit. At varius vel pharetra vel turpis nunc eget
⁷⁵ lorem. Elit scelerisque mauris pellentesque pulvinar pellentesque habitant morbi
⁷⁶ tristique senectus. Odio euismod lacinia at quis risus sed vulputate odio. Vitae suscipit
⁷⁷ tellus mauris a diam maecenas sed enim ut. Dignissim convallis aenean et tortor at
⁷⁸ risus viverra. Diam sollicitudin tempor id eu. Erat velit scelerisque in dictum. Blandit
⁷⁹ cursus risus at ultrices. Ac tortor vitae purus faucibus ornare suspendisse sed.

Contents

| | | |
|-----|---|----------|
| 81 | 1 Neutrino Oscillation Physics | 1 |
| 82 | 1.1 Discovery of Neutrinos | 1 |
| 83 | 1.2 Theory of Neutrino Oscillation | 3 |
| 84 | 1.2.1 Three Flavour Oscillations | 3 |
| 85 | 1.2.2 The MSW Effect | 7 |
| 86 | 1.3 Neutrino Oscillation Measurements | 9 |
| 87 | 1.3.1 Solar Neutrinos | 9 |
| 88 | 1.3.2 Atmospheric Neutrinos | 12 |
| 89 | 1.3.3 Accelerator Neutrinos | 15 |
| 90 | 1.3.4 Reactor Neutrinos | 18 |
| 91 | 1.4 The Super-Kamiokande Experiment | 20 |
| 92 | 1.4.1 The SK Detector | 21 |
| 93 | 1.4.2 Calibration | 24 |
| 94 | 1.4.3 Data Acquisition and Triggering | 28 |
| 95 | 1.4.4 Cherenkov Radiation | 30 |
| 96 | 1.5 The Tokai to Kamioka Experiment | 32 |
| 97 | 1.5.1 The Neutrino Beam | 34 |
| 98 | 1.5.2 The Near Detector at 280m | 37 |
| 99 | 1.5.2.1 Fine Grained Detectors | 39 |
| 100 | 1.5.2.2 Time Projection Chambers | 41 |
| 101 | 1.5.2.3 π^0 Detector | 42 |
| 102 | 1.5.2.4 Electromagnetic Calorimeter | 44 |
| 103 | 1.5.2.5 Side Muon Range Detector | 45 |
| 104 | 1.5.3 The Interactive Neutrino GRID | 45 |

| | | |
|-----|--|-----|
| 105 | 2 Bayesian Statistics and Markov Chain Monte Carlo Techniques | 47 |
| 106 | 2.1 Bayesian Statistics | 48 |
| 107 | 2.2 Monte Carlo Simulation | 49 |
| 108 | 2.2.1 Markov Chain Monte Carlo | 51 |
| 109 | 2.2.2 Metropolis-Hastings Algorithm | 54 |
| 110 | 2.2.3 MCMC Optimisation | 55 |
| 111 | 2.3 Understanding the MCMC Results | 59 |
| 112 | 2.3.1 Marginalisation | 59 |
| 113 | 2.3.2 Parameter Estimation and Credible Intervals | 60 |
| 114 | 2.3.3 Application of Bayes' Theorem | 62 |
| 115 | 2.3.4 Comparison of MCMC Output to Expectation | 63 |
| 116 | 3 Simulation, Reconstruction and Event Selections | 65 |
| 117 | 3.1 Simulation | 65 |
| 118 | 3.2 Event Reconstruction at SK | 70 |
| 119 | 3.3 Event Selection at SK | 80 |
| 120 | 4 Oscillation Probability Calculation | 85 |
| 121 | 4.1 Overview | 86 |
| 122 | 4.2 Treatment of Fast Oscillations | 93 |
| 123 | 4.3 Calculation Engine | 102 |
| 124 | 4.4 Matter Density Profile | 103 |
| 125 | 4.5 Production Height Averaging | 110 |
| 126 | Bibliography | 114 |
| 127 | List of Figures | 125 |
| 128 | List of Tables | 133 |

¹³⁰ **Chapter 1**

¹³¹ **Neutrino Oscillation Physics**

¹³² When first proposed, neutrinos were expected to be massless fermions that only in-
¹³³ teract through weak and gravitational forces. This meant they were very difficult to
¹³⁴ detect as they can pass through significant amounts of matter without interacting. De-
¹³⁵ spite this, experimental neutrino physics has developed with many different detection
¹³⁶ techniques and neutrino sources being used today. In direct tension with **the** standard
¹³⁷ model physics, neutrinos have been determined to oscillate between different lepton
¹³⁸ flavours, requiring them to have mass.

¹³⁹ **The observation techniques which lead to the discovery of the neutrino are doc-**
¹⁴⁰ **umented in section 1.1.** The theory underpinning neutrino oscillation is described in
¹⁴¹ section 1.2. This section includes the approximations which can be made to simplify
¹⁴² the understanding of neutrino oscillation in a two-flavour approximation as well
¹⁴³ as how the medium in which neutrinos propagate can manipulate the oscillation
¹⁴⁴ probability. **Past**, current, and future neutrino experiments are detailed in section 1.3,
¹⁴⁵ including the reactor, atmospheric, and long-baseline accelerator neutrino sources that
¹⁴⁶ have been used to successfully constrain oscillation **parameters determination**.

¹⁴⁷ **1.1 Discovery of Neutrinos**

¹⁴⁸ At the start of the 20th century, the electrons emitted from the β -decay of the nucleus
¹⁴⁹ were found to have a continuous energy spectrum [1,2]. This observation seemingly
¹⁵⁰ broke the energy conservation invoked within that period's nuclear models. Postulated

in 1930 by Pauli as the solution to this problem, the neutrino (originally termed “neutron”) was theorized to be an electrically neutral spin-1/2 fermion with a mass of the same order of magnitude as the electron [3]. This neutrino was to be emitted with the electron in β -decay to alleviate the apparent breaking of energy conservation. As a predecessor of **the today's** weak interaction model, Fermi's theory of β -decay developed the understanding by coupling the four constituent particles; electron, proton, neutron, and neutrino, into a consistent model [4].

Whilst Pauli was not convinced of the ability to detect neutrinos, **the first observations of the particle were made in the mid-1950s when neutrinos from a reactor were observed via the inverse β -decay (IBD) process, $\bar{\nu}_e + p \rightarrow n + e^+$ [5, 6]. The detector consisted of two parts: a neutrino interaction medium and a liquid scintillator.** The interaction medium was built from two water tanks. These were loaded with cadmium chloride to allow increased efficiency of neutron capture. The positron emitted from IBD annihilates, $e^+ + e^- \rightarrow 2\gamma$, generating a prompt signal and the neutron is captured on the cadmium via $n + ^{108}Cd \rightarrow ^{109^*}Cd \rightarrow ^{109}Cd + \gamma$, producing a delayed signal. **The experiment observed an increase in the neutrino event rate when the reactor was operating compared to when it was switched off, in much the same way as modern reactor neutrino experiments operate. An increase in the coincidence rate was observed when the reactor was operating which was interpreted as interactions from neutrinos generated in the reactor.**

After the discovery of the ν_e , the natural question of how many flavours of neutrino exist was asked. In 1962, a measurement of the ν_μ was conducted at the Brookhaven National Laboratory [7]. A proton beam was directed at a beryllium target, generating a π -dominated beam which then decayed via $\pi^\pm \rightarrow \mu^\pm + (\nu_\mu, \bar{\nu}_\mu)$, and the subsequent interactions of the ν_μ were observed. **As the subsequent interaction of the neutrino generates muons rather than electrons, it was determined the ν_μ was**

177 **fundamentally different from ν_e .** The final observation to be made was that of the
178 ν_τ from the DONUT experiment [8]. Three neutrinos seem the obvious solution as it
179 mirrors the known number of charged lepton (as they form weak isospin doublets) but
180 there could be evidence of more. Several neutrino experiments have found anomalous
181 results [9, 10] which could be attributed to sterile neutrinos however cosmological
182 observations indicate the number of neutrino species $N_{eff} = 2.99 \pm 0.17$ [11]. DB:
183 Need to determine how N_{eff} is calculated.

184 1.2 Theory of Neutrino Oscillation

185 As direct evidence of beyond Standard Model physics, a neutrino generated with
186 lepton flavour α can change into a different lepton flavour β after propagating some
187 distance. This phenomenon is called neutrino oscillation and requires that neutrinos
188 must have a non-zero mass (as seen in subsection 1.2.1). This **observation** is direct
189 evidence of beyond standard model physics. This behaviour has been characterised
190 by the Pontecorvo-Maki-Nakagawa-Sakata (PMNS) [12–14] mixing matrix which
191 describes how the flavour and mass of neutrinos are associated. This is analogous to
192 the Cabibbo-Kobayashi-Maskawa (CKM) [15] matrix measured in quark physics.

193 1.2.1 Three Flavour Oscillations

194 The PMNS parameterisation defines three flavour eigenstates, ν_e , ν_μ and ν_τ (indexed
195 ν_α), which are **assigned based upon eigenstates of** the weak interaction **flavour states**
196 and three mass eigenstates, ν_1 , ν_2 and ν_3 (indexed ν_i). Each mass eigenstate is the
197 superposition of all three flavour states,

$$|\nu_i\rangle = \sum_{\alpha} U_{\alpha i} |\nu_{\alpha}\rangle. \quad (1.1)$$

198 Where U is the PMNS matrix which **is unitary and connects correlates** the mass
199 and flavour eigenstates.

200 ~~Neutrinos interact with leptons of the same weak flavour eigenstate rather than~~
201 ~~mass eigenstate. The weak interaction couples to flavour eigenstates so neutrinos~~
202 ~~interact with leptons of the same flavour.~~ The propagation of a neutrino flavour
203 eigenstate, in a vacuum, can be re-written as a plane-wave solution to the time-
204 dependent Schrödinger equation,

$$|\nu_{\alpha}(t)\rangle = \sum_i U_{\alpha i}^{*} |\nu_i\rangle e^{-i\phi_i}. \quad (1.2)$$

205 The probability of observing a neutrino of flavour eigenstate β from one which
206 originated as flavour α can be calculated as,

$$P(\nu_{\alpha} \rightarrow \nu_{\beta}) = |\langle \nu_{\beta} | \nu_{\alpha}(t) \rangle|^2 = \sum_{i,j} U_{\alpha i}^{*} U_{\beta i} U_{\alpha j} U_{\beta j}^{*} e^{-i(\phi_j - \phi_i)} \quad (1.3)$$

207 The ϕ_i term can be expressed in terms of the energy, E_i , and magnitude of the
208 three momenta, p_i , of the neutrino, $\phi_i = E_i t - p_i x$ (t and x being time and position
209 coordinates). Therefore,

$$\phi_j - \phi_i = E_j t - E_i t - p_j x + p_i x. \quad (1.4)$$

²¹⁰ For a relativistic particle, $E_i \gg m_i$,

$$p_i = \sqrt{E_i^2 - m_i^2} \approx E_i - \frac{m_i^2}{2E_i}. \quad (1.5)$$

²¹¹ Making the approximations that neutrinos are relativistic, the mass eigenstates
²¹² were created with the same energy and that $x = L$, where L is the distance traveled by
²¹³ the neutrino, Equation 1.4 then becomes

$$\phi_j - \phi_i = \frac{\Delta m_{ij}^2 L}{2E}, \quad (1.6)$$

²¹⁴ where $\Delta m_{ij}^2 = m_i^2 - m_j^2$. This, **teamed combined** with further use of unitarity
²¹⁵ relations results in Equation 1.3 becoming

$$P(\nu_\alpha \rightarrow \nu_\beta) = \delta_{\alpha\beta} - 4 \sum_{i>j} \Re \left(U_{\alpha i}^* U_{\beta i} U_{\alpha j} U_{\beta j}^* \right) \sin^2 \left(\frac{\Delta m_{ij}^2 L}{4E} \right) + (-) 2 \sum_{i>j} \Im \left(U_{\alpha i}^* U_{\beta i} U_{\alpha j} U_{\beta j}^* \right) \sin \left(\frac{\Delta m_{ij}^2 L}{2E} \right). \quad (1.7)$$

²¹⁶ Where $\delta_{\alpha\beta}$ is the Kronecker delta function and the negative sign **on the last term** is
²¹⁷ included for the oscillation probability of antineutrinos.

²¹⁸ Typically, the PMNS matrix is parameterised into three mixing angles, a charge
²¹⁹ parity (CP) violating phase δ_{CP} , and two Majorana phases $\alpha_{1,2}$,

$$U = \underbrace{\begin{pmatrix} 1 & 0 & 0 \\ 0 & c_{23} & s_{23} \\ 0 & -s_{23} & c_{23} \end{pmatrix}}_{\text{Atmospheric, Accelerator}} \underbrace{\begin{pmatrix} c_{13} & 0 & s_{13}e^{-i\delta_{CP}} \\ 0 & 1 & 0 \\ -s_{13}e^{-i\delta_{CP}} & 0 & c_{13} \end{pmatrix}}_{\text{Reactor, Accelerator}} \underbrace{\begin{pmatrix} c_{12} & s_{12} & 0 \\ -s_{12} & c_{12} & 0 \\ 0 & 0 & 1 \end{pmatrix}}_{\text{Reactor, Solar}} \underbrace{\begin{pmatrix} e^{i\alpha_1/2} & 0 & 0 \\ 0 & e^{i\alpha_2/2} & 0 \\ 0 & 0 & 1 \end{pmatrix}}_{\text{Majorana}}. \quad (1.8)$$

²²⁰ Where $s_{ij} = \sin(\theta_{ij})$ and $c_{ij} = \cos(\theta_{ij})$. The oscillation parameters are often
²²¹ grouped; (1,2) as “solar”, (2,3) as “atmospheric” and (1,3) as “reactor”. Many
²²² neutrino experiments aim to measure the PMNS parameters from a wide array of
²²³ origins, as is the purpose of this thesis.

²²⁴ The Majorana phase, $\alpha_{1,2}$, **containing matrix** included within **the fourth matrix**
²²⁵ **in** Equation 1.8 is only included for completeness. For an oscillation analysis ex-
²²⁶ periment, **any term in this oscillation probability calculation containing this phase**
²²⁷ **disappears any terms containing thtis phase disappear** due to taking the expectation
²²⁸ value of the PMNS matrix. **Measurements of these phases are typically performed**
²²⁹ **by experiments searching for neutrino-less double β -decay [16].**

²³⁰ A two flavour approximation can be **attained obtained** when one assumes the third
²³¹ mass eigenstate is degenerate with another. As discussed in section 1.3, it is found
²³² that $\Delta m_{21}^2 \ll |\Delta m_{31}^2|$. This results in the two flavour approximation being reasonable
²³³ for understanding the features of the oscillation. In this two flavour case, the mixing
²³⁴ matrix becomes,

$$U_{2 \text{ Flav.}} = \begin{pmatrix} \cos(\theta) & \sin(\theta) \\ -\sin(\theta) & \cos(\theta) \end{pmatrix}. \quad (1.9)$$

²³⁵ This culminates in the oscillation probability,

$$\begin{aligned} P(\nu_\alpha \rightarrow \nu_\alpha) &= 1 - \sin^2(2\theta) \sin^2\left(\frac{\Delta m^2 L}{4E}\right), \\ P(\nu_\alpha \rightarrow \nu_\beta) &= \sin^2(2\theta) \sin^2\left(\frac{\Delta m^2 L}{4E}\right). \end{aligned} \quad (1.10)$$

²³⁶ **For Where** $\alpha \neq \beta$. For a fixed neutrino energy, the oscillation probability is a sinusoidal function depending upon the distance over which the neutrino propagates. The ²³⁷ frequency and amplitude of oscillation are dependent upon **the ratio of the** $\Delta m^2 / 4E$ ²³⁸ and $\sin^2 2\theta$, respectively. **The oscillation probabilities presented thus far assume** ²³⁹ **c = 1, where c is the speed of light in vacuum. In more familiar units**, the maximum ²⁴⁰ oscillation probability for a fixed value of θ is given at $L[\text{km}] / E[\text{GeV}] \sim 1.27 / \Delta m^2$. ²⁴¹ It is this calculation that determines the best L/E value for a given experiment to be ²⁴² designed around for measurements of a specific value of Δm^2 . ²⁴³

²⁴⁴ 1.2.2 The MSW Effect

²⁴⁵ The theory of neutrino oscillation in a vacuum **is has been** described in subsection 1.2.1. ²⁴⁶ However, the beam neutrinos and atmospheric neutrinos originating from below the ²⁴⁷ horizon propagate through matter in the Earth. The coherent scattering of neutrinos ²⁴⁸ from a material target modifies the Hamiltonian of the system. This results in a change ²⁴⁹ in the oscillation probability. Notably, charged current scattering ($\nu_e + e^- \rightarrow \nu_e + e^-$,

250 propagated by a W boson) only affects electron neutrinos **compared to whereas** the
251 neutral current scattering ($\nu_l + l^- \rightarrow \nu_l + l^-$, propagated by a Z^0 boson) interacts
252 through all neutrino flavours equally. In the two-flavour **limit approximation**, the
253 effective mixing parameter becomes

$$\sin^2(2\theta) \rightarrow \sin^2(2\theta_m) = \frac{\sin^2(2\theta)}{(A/\Delta m^2 - \cos(2\theta))^2 + \sin^2(2\theta)}, \quad (1.11)$$

254 where $A = 2\sqrt{2}G_F N_e E$, **with** N_e is the electron density of the medium and G_F is
255 Fermi's constant. It is clear to see that there exists a value of $A = \Delta m^2 \cos(2\theta)$ for
256 $\Delta m^2 > 0$ which results in a divergent mixing parameter. This resonance is **due to**
257 **termed** the Mikheyev-Smirnov-Wolfenstein (MSW) effect (or more colloquially, the
258 matter resonance) which regenerates the electron neutrino component of the neutrino
259 flux [17–19]. The density at which the resonance occurs is given by

$$N_e = \frac{\Delta m^2 \cos(2\theta)}{2\sqrt{2}G_F E}. \quad (1.12)$$

260 At densities lower than this critical value, the oscillation probability will be much
261 closer to that of vacuum oscillation. **For antineutrinos, $N_e \rightarrow -N_e$ [20].** The reso-
262 nance occurring from the MSW effect depends on the sign of Δm^2 . Therefore, any
263 neutrino oscillation experiment which observes neutrinos and antineutrinos which
264 have propagated through matter can have some sensitivity to the ordering of the
265 neutrino mass eigenstates.

²⁶⁶ 1.3 Neutrino Oscillation Measurements

²⁶⁷ As evidence of beyond standard model physics, the 2015 Nobel Prize in Physics was
²⁶⁸ awarded to the Super-Kamiokande (SK) [21] and Sudbury Neutrino Observatory
²⁶⁹ (SNO) [22] collaborations for the first definitive observation of solar and atmospheric
²⁷⁰ neutrino oscillation [23]. Since then, the field has seen a wide array of oscillation
²⁷¹ measurements from a variety of neutrino sources. As seen in subsection 1.2.1, the
²⁷² neutrino oscillation probability is dependent on the ratio of the propagation baseline, L ,
²⁷³ to the neutrino energy, E . It is this ratio that determines the type of neutrino oscillation
²⁷⁴ a particular experiment is sensitive to.

²⁷⁵ As illustrated in Figure 1.1, there are many neutrino sources that span a wide
²⁷⁶ range of energies. The least energetic neutrinos are from diffuse supernovae and
²⁷⁷ terrestrial neutrinos at $O(1)$ MeV whereas the most energetic neutrinos originate from
²⁷⁸ atmospheric and galactic neutrinos of $> O(1)$ TeV.

²⁷⁹ 1.3.1 Solar Neutrinos

²⁸⁰ Solar neutrinos are emitted from fusion reaction chains at the center of the Sun. The
²⁸¹ solar neutrino flux, given as a function of neutrino energy for different fusion and
²⁸² decay chains, is illustrated in Figure 1.2. Whilst proton-proton fusion generates the
²⁸³ largest flux of neutrinos, the neutrinos are of low energy and are difficult to reconstruct
²⁸⁴ due to the IBD interaction threshold of 1.8MeV. Consequently, most experiments focus
²⁸⁵ on the neutrinos from the decay of 8B (via $^8B \rightarrow ^8Be^* + e^+ + \nu_e$), which are higher
²⁸⁶ energy.

²⁸⁷ The first measurements of solar neutrinos observed a significant reduction in the
²⁸⁸ event rate compared to predictions from the Standard Solar Model [26, 27]. The

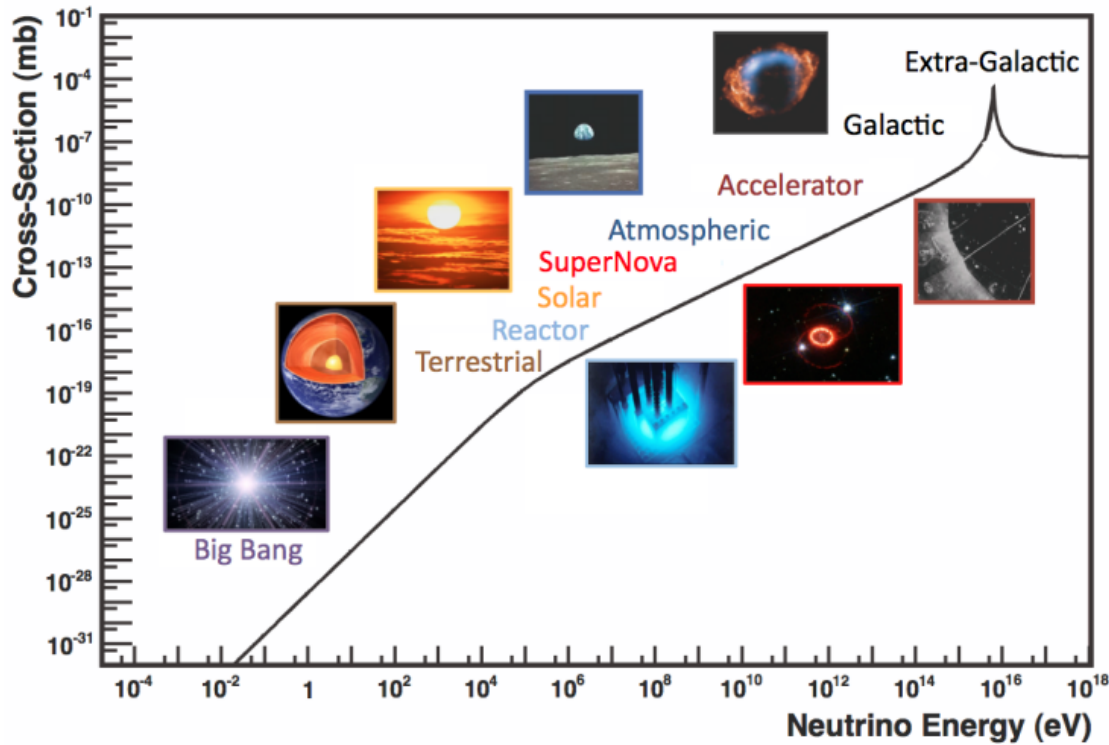


Figure 1.1: The cross-section of neutrinos from various natural and man-made sources as a function of neutrino energy. Taken from [24]

289 proposed solution to this “solar neutrino problem” was $\nu_e \leftrightarrow \nu_\mu$ oscillations in a
 290 precursory version of the PMNS model [28]. The Kamiokande [29], Gallex [30] and
 291 Sage [31] experiments confirmed the ~ 0.5 factor deficit of solar neutrinos.

292 The conclusive solution to this problem was determined by the SNO collabora-
 293 tion [32]. Using a deuterium water target to observe 8B neutrinos, the event rate of
 294 charged current (CC), neutral current (NC), and elastic scattering (ES) interactions
 295 (Given in Equation 1.13) was simultaneously measured. CC events can only occur
 296 for electron neutrinos, whereas the ~~other interaction NC channels are~~ is agnostic
 297 to neutrino flavour (~~Although , and~~ the ES reaction ~~is more sensitive has a slight~~
 298 ~~excess sensitivity~~ to electron neutrino interactions). This meant that there were direct
 299 measurements of the ν_e and ν_x neutrino flux. It was concluded that the CC and ES
 300 interaction rates were consistent with the deficit previously observed. Most impor-

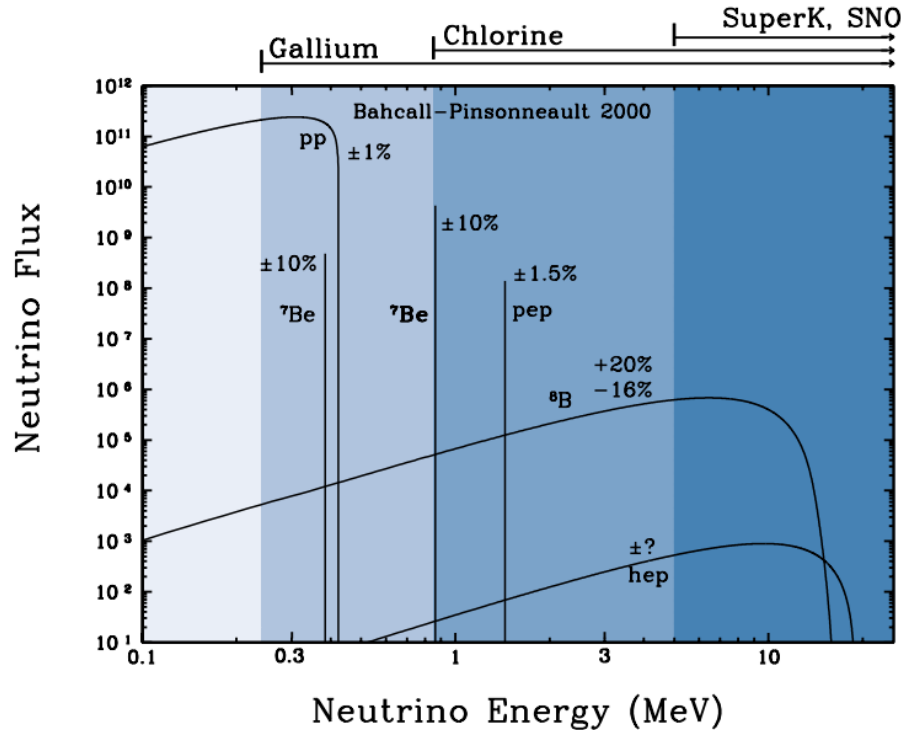


Figure 1.2: The solar neutrino flux as a function of neutrino energy for various fusion reactions and decay chains as predicted by the Standard Solar Model. Taken from [25].

tantly, the NC reaction rate was only consistent with the others under the hypothesis of flavour transformation.

$$\nu_e + d \rightarrow p + p + e^- \quad (CC)$$

$$\nu_x + d \rightarrow p + n + \nu_x \quad (NC) \quad (1.13)$$

$$\nu_x + e^- \rightarrow \nu_x + e^- \quad (ES)$$

Many experiments have since measured the neutrino flux of different interaction chains within the sun [33–35]. The most recent measurement was that of CNO neutrinos which were recently observed with 5σ significance by the Borexino collaboration. Future neutrino experiments aim to further these spectroscopic measurements of different fusion chains within the Sun [36–38]. Solar neutrinos act as an irreducible

³⁰⁸ background for dark matter experiments like DARWIN but oscillation parameter
³⁰⁹ measurements can be made [39].

³¹⁰ **1.3.2 Atmospheric Neutrinos**

³¹¹ The interactions of primary cosmic ray protons in Earth's upper atmosphere generate
³¹² showers of energetic hadrons. These are mostly pions and kaons which when they
³¹³ decay produce a natural source of neutrinos spanning energies of MeV to TeV [40].

³¹⁴ **This** The main decay is via

$$\begin{aligned} \pi^\pm &\rightarrow \mu^\pm + (\nu_\mu, \bar{\nu}_\mu) \\ \mu^\pm &\rightarrow e^\pm + (\nu_\mu, \bar{\nu}_\mu) + (\nu_e, \bar{\nu}_e) \end{aligned} \tag{1.14}$$

³¹⁵ such that for a single pion decay, three neutrinos are typically produced. The
³¹⁶ atmospheric neutrino flux energy spectra as predicted by the Bartol [41], Honda
³¹⁷ [42–44], and FLUKA [45] models are illustrated in Figure 1.3. The flux distribution
³¹⁸ peaks at an energy of $O(10)\text{GeV}$. The uncertainties associated with these models
³¹⁹ are dominated by the hadronic production of kaon and pions as well as the primary
³²⁰ cosmic flux.

³²¹ Unlike long-baseline experiments which have a fixed baseline, the distance at-
³²² mospheric neutrinos propagate is dependent upon the zenith angle at which they
³²³ interact. This is illustrated in Figure 1.4. Neutrinos that are generated directly above
³²⁴ the detector ($\cos(\theta) = 1.0$) have a baseline equivalent to the height of the atmosphere
³²⁵ whereas neutrinos that interact directly below the detector ($\cos(\theta) = -1.0$) have to
³²⁶ travel a length equal to the diameter of the Earth. This means atmospheric neutrinos
³²⁷ have a baseline that varies from $O(20)\text{km}$ to $O(6 \times 10^3)\text{km}$. Any neutrino generated

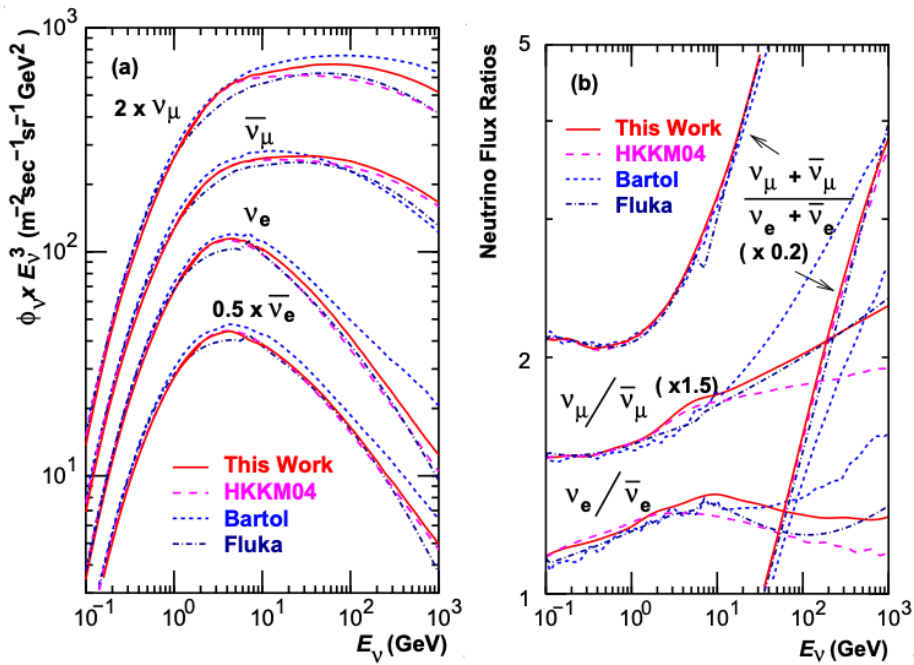


Figure 1.3: Left panel: The atmospheric neutrino flux for different neutrino flavours as a function of neutrino energy as predicted by the 2007 Honda model (“This work”) [42], the 2004 Honda model (“HKKM04”) [43], the Bartol model [41] and the FLUKA model [45]. Right panel: The ratio of the muon to electron neutrino flux as predicted by all the quoted models. Both figures taken from [42].

328 at or below the horizon will be subject to matter effects as they propagate through the
 329 Earth.

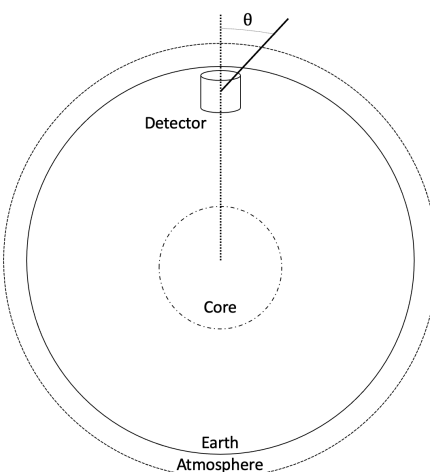


Figure 1.4: A diagram illustrating the definition of zenith angle as used in the Super Kamiokande experiment [46].

Figure 1.5 highlights the neutrino flux as a function of the zenith angle for different slices of neutrino energy. For medium to high-energy neutrinos (and to a lesser degree for low-energy neutrinos), the flux is approximately symmetric around $\cos(\theta) = 0$. To the accuracy of this approximation, the systematic uncertainties associated with atmospheric flux for comparing upward-going and down-going neutrino cancels. This allows the down-going events, which are mostly insensitive to oscillation probabilities, to act as an unoscillated prediction (similar to a near detector in an accelerator neutrino experiment).

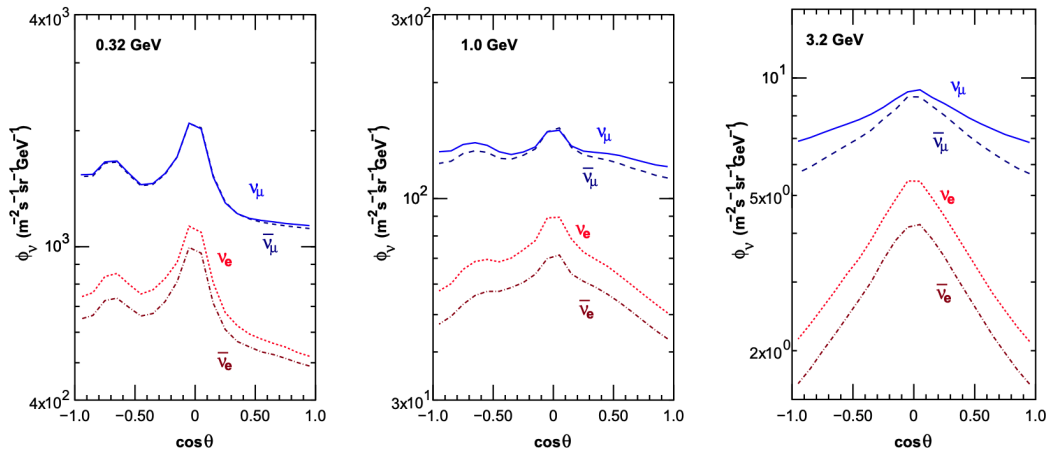


Figure 1.5: Prediction of $\nu_e, \bar{\nu}_e, \nu_\mu, \bar{\nu}_\mu$ fluxes as a function of zenith angle as calculated by the HKKM model [44]. The left, middle and right panels represent three values of neutrino energy, 0.32GeV, 1.0GeV and 3.2GeV respectively. Predictions for other models including Bartol [41], Honda [42] and FLUKA [45] are given in [46].

Precursory hints of atmospheric neutrinos were observed in the mid-1960s searching for $\nu_\mu + X \xrightarrow{(-)} X^* + \mu^\pm$ [47], although it was called an anomaly at the time of measurement. This was succeeded with the IMB-3 [48] and Kamiokande [49] experiments which measured the ratio of muon neutrinos compared to electron neutrinos $R(\nu_\mu/\nu_e)$. Both experiments were found to have a consistent deficit of muon neutrinos, with $R(\nu_\mu/\nu_e) = 0.67 \pm 0.17$ and $R(\nu_\mu/\nu_e) = 0.60^{+0.07}_{-0.06} \pm 0.05$. Super-Kamiokande (SK) [46] extended this analysis by fitting oscillation parameters in $P(\nu_\mu \rightarrow \nu_\tau)$ which found best fit parameters $\sin^2(2\theta) > 0.92$ and $1.5 \times 10^{-3} < \Delta m^2 < 3.4 \times 10^{-3}$ eV².

Since then, atmospheric neutrino experiments have been making precision measurements of the $\sin^2(\theta_{23})$ and Δm_{32}^2 oscillation parameters. Atmospheric neutrino oscillation is dominated by $P(\nu_\mu \rightarrow \nu_\tau)$, where SK observed a 4.6σ discovery of ν_τ appearance [50]. Figure 1.6 illustrates the current estimates on the atmospheric mixing parameters from a wide range of atmospheric and accelerator neutrino observatories.

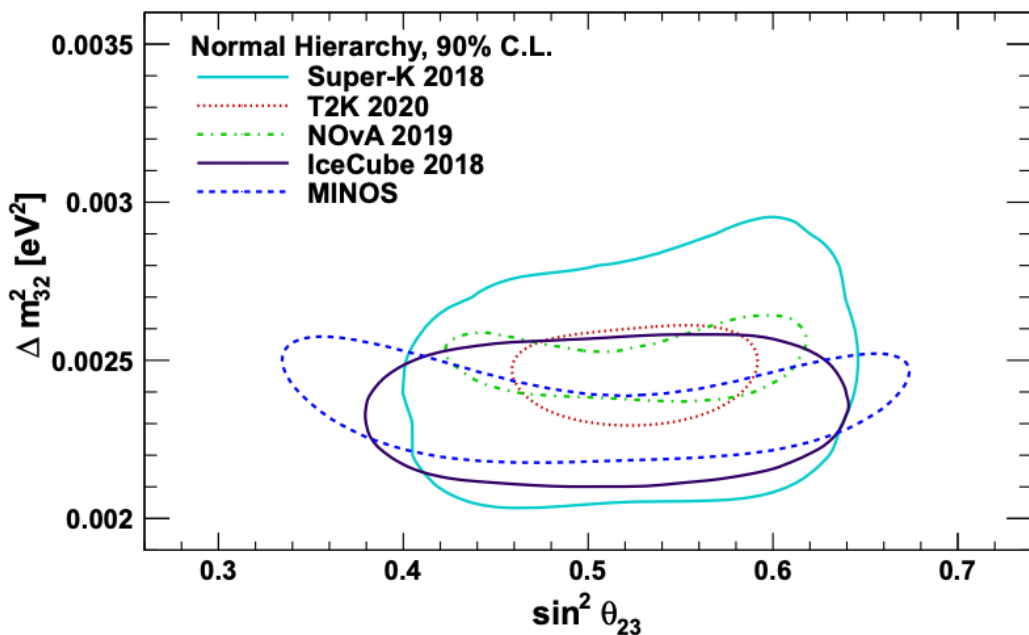


Figure 1.6: Constraints on the atmospheric oscillation parameters, $\sin^2(\theta_{23})$ and Δm_{32}^2 , from atmospheric and long baseline experiments: SK [51], T2K [52], NO ν A [53], IceCube [54] and MINOS [55]. Figure taken from [56].

1.3.3 Accelerator Neutrinos

The concept of using a man-made “neutrino beam” was first realised in 1962 [57]. Since then, many experiments have followed which all use the same fundamental concepts. Typically, a proton beam is aimed at a target producing charged mesons that decay to neutrinos. The mesons can be sign-selected by the use of magnetic focusing horns to generate a neutrino or antineutrino beam. Pions are the primary meson that decay and depending on the orientation of the magnetic field, a muon (anti-)neutrino

beam is generated via $\pi^+ \rightarrow \mu^+ + \nu_\mu$ or $\pi^- \rightarrow \mu^- + \bar{\nu}_\mu$. The decay of muons and kaons does result in an irreducible intrinsic electron neutrino background. In T2K, this background contamination is $O(< 1\%)$ [58]. There is also an approximately $\sim 5\%$ “wrong-sign” neutrino background of $\bar{\nu}_\mu$ generated via the same decays. DB: Need to mention that the beam in proton, not antineutrino so the numu flux is higher in the numubar beam

~~The energy of each neutrino in the beam is dependent on the energy of the initial proton beam. Therefore, tuning the proton energy allows Tuning the proton energy in the beam and using beam focusing techniques allows~~ the neutrino energy to be set to a value that maximises the disappearance oscillation probability in the L/E term in Equation 1.10. This means that accelerator experiments are typically more sensitive to the mixing parameters as compared to a natural neutrino source. However, the disadvantage compared to atmospheric neutrino experiments is that the baseline has to be shorter due to the lower flux. Consequently, there is typically less sensitivity to matter effects and the ordering of the neutrino mass eigenstates.

A neutrino experiment measures

$$R(\vec{x}) = \Phi(E_\nu) \times \sigma(E_\nu) \times \epsilon(\vec{x}) \times P(\nu_\alpha \rightarrow \nu_\beta), \quad (1.15)$$

where $R(\vec{x})$ is the event rate of neutrinos at position \vec{x} , $\Phi(E_\nu)$ is the flux of neutrinos with energy E_ν , $\sigma(E_\nu)$ is the cross-section of the neutrino interaction and $\epsilon(\vec{x})$ is the efficiency **and resolution** of the detector. In order to leverage the most out of an accelerator neutrino experiment, the flux and cross-section systematics need to be constrained. This is typically done via the use of a “near detector”, situated at a baseline

379 of $O(1)$ km. This detector observes the unoscillated neutrino flux and constrains the
380 parameters used within the flux and cross-section model.

381 The first accelerator experiments to precisely measure oscillation parameters were
382 MINOS [59] and K2K [60]. These experiments confirmed the $\nu_\mu \rightarrow \nu_\mu$ **oscillations**
383 ν_μ **disappearance** seen in atmospheric neutrino experiments by finding consistent
384 **mixing** parameter values for $\sin^2(\theta_{23})$ and Δm_{23}^2 . The current generation of accelera-
385 tor neutrino experiments, T2K and NO ν A extended this field by observing $\bar{\nu}_\mu \rightarrow \bar{\nu}_e$
386 and lead the sensitivity to atmospheric mixing parameters as seen in Figure 1.6 [61].
387 The two experiments differ in their peak neutrino energy, baseline, and detection
388 technique. The NO ν A experiment is situated at a baseline of 810km from the NuMI
389 beamline which delivers 2GeV neutrinos. The T2K neutrino beam is peaked around
390 0.6GeV and propagates 295km. The NO ν A experiment also uses functionally iden-
391 tical detectors (near and far) which allow the approximate cancellation of detector
392 systematics whereas T2K uses a plastic scintillator technique at the near detector and
393 a water Cherenkov far detector. The future generation experiments DUNE [62] and
394 Hyper-Kamiokande [63] will succeed these experiments as the high-precision era of
395 neutrino oscillation parameter measurements develops.

396 Several anomalous results have been observed in the LSND [9] and MiniBooNE [10]
397 detectors which were designed with purposefully short baselines. Parts of the neu-
398 trino community attributed these results to oscillations induced by a fourth “sterile”
399 neutrino [64] but several searches in other experiments, MicroBooNE [65] and KAR-
400 MEN [66], found no hints of additional neutrino species. The solution to the anomalous
401 results **are is** still being determined.

402 1.3.4 Reactor Neutrinos

403 As illustrated in the first discovery of neutrinos (section 1.1), nuclear reactors are a very
 404 useful man-made source of electron antineutrinos. For reactors that use low-enriched
 405 uranium ^{235}U as fuel, the antineutrino flux is dominated by the β -decay fission of ^{235}U ,
 406 ^{238}U , ^{239}Pu and ^{241}Pu [67] as illustrated in Figure 1.7.

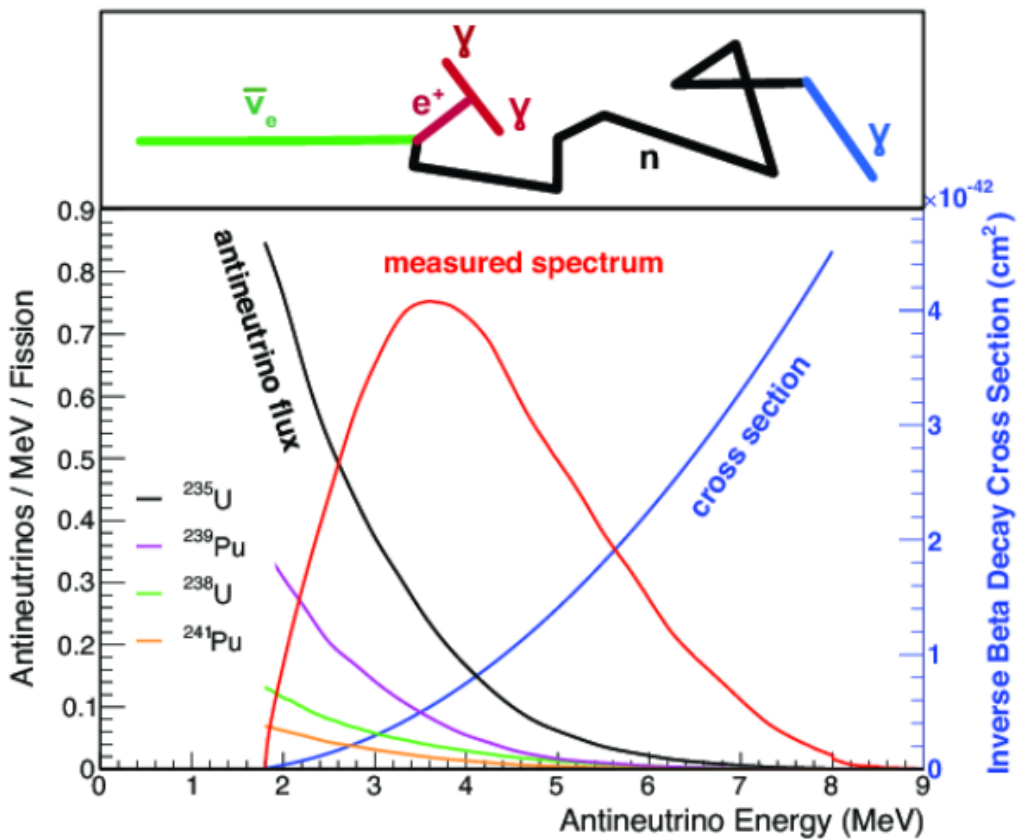


Figure 1.7: Reactor electron antineutrino fluxes for ^{235}U (Black), ^{238}U (Green), ^{239}Pu (Purple), and ^{241}Pu (Orange) isotopes. The inverse β -decay cross-section (Blue) and corresponding measurable neutrino spectrum (Red) are also given. Top panel: Schematic of Inverse β -decay interaction including the eventual capture of the emitted neutron. This capture emits a γ -ray which provides a second signal of the event. Taken from [68].

407 Due to their low energy, reactor electron antineutrinos predominantly interact
 408 via the inverse β -decay (IBD) interaction. The typical signature contains two signals
 409 delayed by $O(200)\mu\text{s}$; firstly the prompt photons from positron annihilation, and

410 secondly the photons emitted ($E_{tot}^\gamma = 2.2\text{MeV}$) from de-excitation after neutron capture
411 on hydrogen. Searching for both signals improves the detector's ability to distinguish
412 between background and signal events [69]. Recently, SK included gadolinium dopants
413 into the ultra-pure water to increase the energy released from the photon cascade to
414 $\sim 8\text{MeV}$ and reduce the time of the delayed signal to $\sim 28\mu\text{s}$.

415 There are many short baseline experiments ($L \sim O(1)\text{km}$) that have measured the
416 $\sin^2(\theta_{13})$ and Δm_{23}^2 oscillation parameters. Daya Bay [70], RENO [71] and Double
417 Chooz [72] have all provided precise measurements, with the first discovery of a
418 non-zero θ_{13} made by Daya Bay and RENO (and ~~complimented complemented~~ by
419 T2K [72]). The constraints on $\sin^2(\theta_{13})$ by the reactor experiments lead the field and
420 are often used as external inputs to accelerator neutrino experiments to improve their
421 sensitivity to δ_{CP} and mass hierarchy determination. JUNO-TAO [73], a small collabora-
422 ration within the larger JUNO experiment, is a next-generation reactor experiment that
423 aims to precisely measure the isotopic antineutrino yields from the different fission
424 chains. Alongside this, it aims to explain the '5MeV excess' [74–76] by conducting a
425 search for sterile neutrinos with a mass scale of around 1eV.

426 Kamland [77] is the only experiment to have observed reactor neutrinos using a
427 long baseline (flux weighted averaged baseline of $L \sim 180\text{km}$) which allows it to have
428 sensitivity to Δm_{12}^2 . Combined with the SK solar neutrino experiment, the combined
429 analysis puts the most stringent constraint on Δm_{12}^2 [78] ~~which is used as a prior~~
430 ~~uncertainty within accelerator neutrino experiments.~~

431 DB: Include a conclusion section with PDG results chapterT2K and SK Experiment
432 Overview

433 As the successor of the Kamiokande experiment, the Super-Kamiokande (SK)
434 collaboration has been leading atmospheric neutrino oscillation analyses for over
435 two decades. The detector has provided some of the strongest constraints on proton

decay **limits** and **as well as** the first precise measurements of the Δm_{23}^2 and $\sin^2(\theta_{23})$ neutrino oscillation parameters. **Despite this, the The** ability of the detector to low-energy neutrino events has been significantly improved with the recent gadolinium doping of the ultra-pure water target. **section 2.1 describes the history, detection technique, and operation of the SK detector. The history, detection technique, and operation of the SK detector is described in section 1.4.**

The Tokai-to-Kamioka (T2K) experiment was one of the first long-baseline experiments to use both neutrino and antineutrino beams to precisely measure the charge parity violation within the neutrino sector. With the SK detector observing the oscillated neutrino flux, the T2K experiment observed the first hints of a non-zero $\sin^2(\theta_{13})$ measurement and continues to lead the field with the constraints it provides on $\sin^2(\theta_{13})$, $\sin^2(\theta_{23})$, Δm_{23}^2 and δ_{CP} . **section 2.2 documents the The** techniques which T2K uses in generating its neutrino beam as well as the near-detector used to constrain the flux and cross-section parameters **invoked within the systematic models used in this analysis are documented in section 1.5.**

1.4 The Super-Kamiokande Experiment

The SK experiment began taking data in 1996 [79] and has had many modifications throughout its lifespan. There have been seven defined periods of data taking as noted in Table 1.1. Data taking began in SK-I which ran for five years. Between the SK-I and SK-II periods, a significant proportion of the PMTs were damaged during maintenance. Those that survived were equally distributed throughout the detector in the SK-II era, which resulted in a reduced photo-coverage. From SK-III onwards, repairs to the detector meant the full suite of PMTs was operational. Before the start of SK-IV, the data acquisition and electronic systems were upgraded. Between

⁴⁶⁰ SK-IV and SK-V, a significant effort was placed into tank open maintenance and
⁴⁶¹ repair/replacement of defective PMTs, a task for which the author of this thesis was
⁴⁶² required. Consequently, the detector conditions were significantly different between
⁴⁶³ the two operational periods. SK-VI saw the start of the 0.01% gadolinium doped
⁴⁶⁴ water. SK-VII, which started during the writing of this thesis, has increased the
⁴⁶⁵ gadolinium concentration to 0.03% for continued operation. [DB: Link to Linyan's talk](#)
⁴⁶⁶ [from Nu2022](#).

| Period | Start Date | End Date | Live-time (days) |
|--------|----------------|----------------|------------------|
| I | April 1996 | July 2001 | 1489.19 |
| II | October 2002 | October 2005 | 798.59 |
| III | July 2006 | September 2008 | 518.08 |
| IV | September 2008 | May 2018 | 3244.4 |
| V | January 2019 | July 2020 | 461.02 |
| VI | July 2020 | May 2022 | 583.3 |
| VII | May 2022 | Ongoing | N/A |

Table 1.1: The various SK periods and respective live-time. The SK-VI live-time is calculated until 1st April 2022. SK-VII started during the writing of this thesis.

⁴⁶⁷ 1.4.1 The SK Detector

⁴⁶⁸ The basic structure of the Super-Kamiokande (SK) detector is a cylindrical tank with a
⁴⁶⁹ diameter 39.3m and height 41.1m filled with ultrapure water [80]. A diagram of the
⁴⁷⁰ significant components of the SK detector is [Illustrated given](#) in Figure 1.8. The SK
⁴⁷¹ detector is situated in the Kamioka mine in Gifu, Japan. The mine is underground with
⁴⁷² roughly 1km rock overburden (2.7km water equivalent overburden) [81]. At this depth,
⁴⁷³ the rate of cosmic ray muons is significantly decreased to a value of $\sim 2\text{Hz}$. The top of
⁴⁷⁴ the tank is covered with stainless steel which is designed as a working platform for
⁴⁷⁵ maintenance, calibration, and location for high voltage and data acquisition electronics.

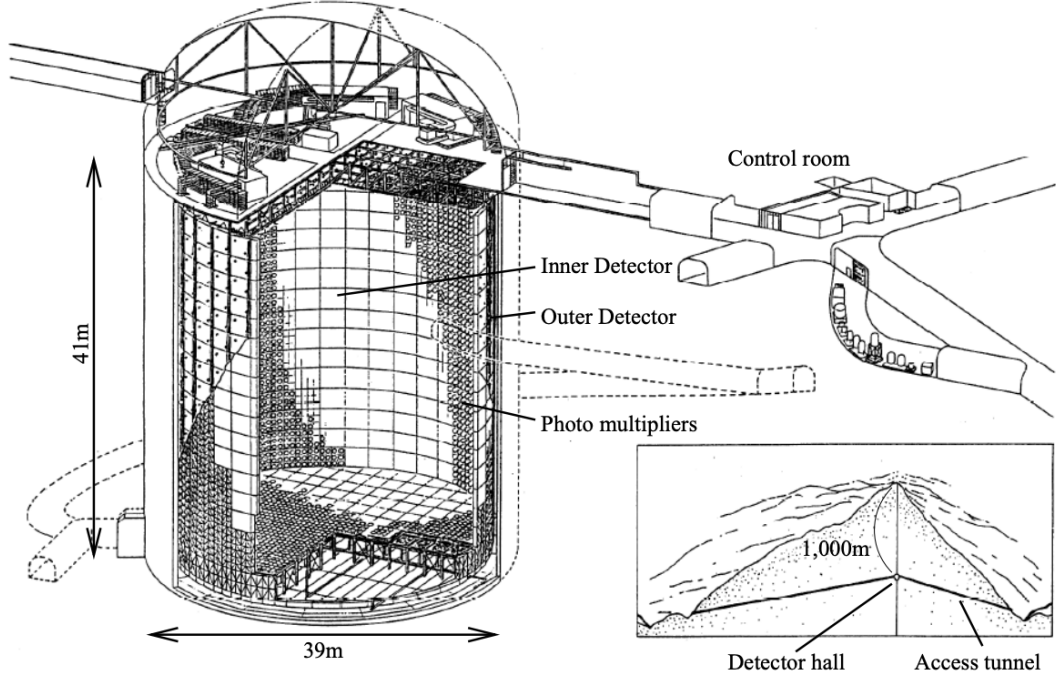


Figure 1.8: A schematic diagram of the Super-Kamiokande Detector. Taken from [82].

476 A smaller cylindrical structure (36.2m diameter, 33.8m height) is situated inside the
 477 tank, with an approximate 2m gap between this structure and the outer tank wall. The
 478 purpose of this structure is to support the photomultiplier tubes (PMTs). The volume
 479 inside and outside the support structure is referred to as the inner detector (ID) and
 480 outer detector (OD), respectively. In the SK-IV era, the ID and OD are instrumented
 481 by 11,129 50cm and 1,885 20cm PMTs respectively [80]. The ID contains a 32kton
 482 mass of water. Many analyses performed at SK use a “fiducial volume” defined by the
 483 volume of water inside the ID excluding some distance to the ID wall. This reduces the
 484 volume of the detector which is sensitive to neutrino events but reduces radioactive
 485 backgrounds and allows for better reconstruction performance. The nominal fiducial
 486 volume is defined as the area contained inside 2m from the ID wall for a total of
 487 22.5kton water [83].

488 The two regions of the detector (ID and OD) are optically separated with opaque
 489 black plastic. The purpose of this is to determine whether a track entered or exited

490 the ID. This allows cosmic ray muons and partially contained events to be tagged and
491 separated from neutrino events entirely contained within the ID. This black plastic is
492 also used to cover the area between the ID PMTs to reduce photon reflection from the
493 ID walls. Opposite to this, the OD is lined with a reflective material to allow photons to
494 reflect around inside the OD until collected by one of the PMTs. Furthermore, each OD
495 PMT is backed with $50 \times 50\text{cm}$ plates of wavelength shifting acrylic which increases
496 the efficiency of light collection [81].

497 In the SK-IV data-taking period, the photocathode coverage of the detector, or the
498 fraction of the ID wall instrumented with PMTs, is $\sim 40\%$ [81]. The PMTs have a
499 quantum efficiency (the ratio of detected electrons to incident photons) of $\sim 21\%$ for
500 photons with wavelengths of $360\text{nm} < \lambda < 390\text{nm}$. The proportion of photoelectrons
501 that produce a signal in the dynode of a PMT, termed the collection efficiency, is
502 $> 70\%$ [81]. The PMTs used within SK are most sensitive to photons with wavelength
503 $300\text{nm} \leq \lambda \leq 600\text{nm}$ [81]. One disadvantage of using PMTs as the detection media
504 is that the Earth's geomagnetic field can modify its response. Therefore, a set of
505 compensation coils is built around the inner surface of the detector to mitigate this
506 effect [84].

507 As mentioned, the SK detector is filled with ultrapure water, which in a perfect
508 world would contain no impurities. However, bacteria and organic compounds can
509 significantly degrade the water quality. This decreases the attenuation length, which
510 reduces the total number of photons that hit a PMT. To combat this, a sophisticated
511 water treatment system has been developed [81, 85]. UV lights, mechanical filters,
512 and membrane degasifiers are used to reduce the bacteria, suspended particulates,
513 and radioactive materials from the water. The flow of water within the tank is also
514 critical as it can remove stagnant bacterial growth or build-up of dust on the surfaces
515 within the tank. Gravity drifts impurities in the water towards the bottom of the

516 tank which, if left uncontrolled, can create asymmetric water conditions between
 517 the top and bottom of the tank. Typically, the water entering the tank is cooled
 518 below the ambient temperature of the tank to control convection and inhibit bacteria
 519 growth. Furthermore, the **rate of** dark noise hits within PMTs is sensitive to the PMT
 520 temperature [86] so controlling the temperature gradients within the tank is beneficial
 521 for stable measurements.

522 SK-VI is the first phase of the SK experiment to use gadolinium dopants within the
 523 ultrapure water [DB: Link to Linyan's talk at Nu2022](#). As such, the SK water system
 524 had to be replaced to avoid removing the gadolinium concentrate from the ultrapure
 525 water [87]. For an inverse β -decay (IBD) interaction in a water target, the emitted
 526 neutron is thermally captured on hydrogen. This process releases 2.2MeV γ rays which
 527 are difficult to detect **due to as the resulting** Compton scattered electrons **from a γ**
 528 **ray of this energy is are** very close to the Cherenkov threshold, limiting the number of
 529 photons produced. Thermal capture of neutrons on gadolinium generates γ rays with
 530 higher energy (**8MeV [69]**) meaning they are more easily detected. SK-VI has 0.01%
 531 Gd loading (0.02% gadolinium sulphate by mass) which causes \approx 50% of neutrons
 532 emitted by IBD to be captured on gadolinium [88,89]. Whilst predominantly useful
 533 for low energy analyses, Gd loading allows better $\nu/\bar{\nu}$ separation for atmospheric
 534 neutrino event selections [90]. Efforts are currently in place to increase the gadolinium
 535 concentrate to 0.03% for \approx 75% neutron capture efficiency on gadolinium [DB: Link to](#)
 536 [Mark's talk at Nu2022](#). The final stage of loading targets 0.1% concentrate.

537 1.4.2 Calibration

538 The calibration of the SK detector is documented in [80] and summarised below. The
 539 analysis presented within this thesis is dependent upon 'high energy events' (Charged
 540 particles with $O(> 100)\text{MeV}$ momenta). These are events that are expected to generate

541 a larger number of photons such that each PMT will be hit with multiple photons.
 542 The reconstruction of these events depends upon the charge deposited within each
 543 PMT and the timing response of each individual PMT. Therefore, the most relevant
 544 calibration techniques to this thesis are outlined.

545 Before installation, 420 PMTs were calibrated to have identical charge responses
 546 and then distributed throughout the tank in a cross-shape pattern (As illustrated by
 547 Figure 1.9). These are used as a standardised measure for the rest of the PMTs installed
 548 at similar geometric positions within SK to be calibrated against. To perform this
 549 calibration, a xenon lamp is located at the center of the SK tank which flashes uniform
 550 light at 1Hz. This allows for geometrical effects, water quality variation, and timing
 551 effects to be measured in-situ throughout normal data-taking periods.

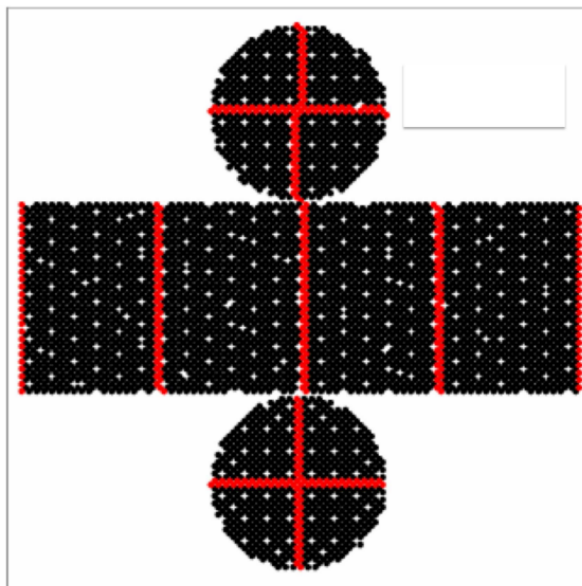


Figure 1.9: The location of “standard PMTs” (red) inside the SK detector. Taken from [80].

552 When specifically performing calibration of the detector (in out-of-data taking
 553 mode), the water in the tank was circulated to avoid top/bottom asymmetric water
 554 quality. Any non-uniformity within the tank significantly affects the PMT hit proba-
 555 bility through scattering or absorption. This becomes a dominant effect for the very

556 low-intensity light sources discussed later which are designed such that only one
557 photon is incident upon a given PMT.

558 The “gain” of a PMT is defined as the ratio of the total charge of the signal produced
559 compared to the charge of photoelectrons emitted by the photocathodes within the
560 PMT. To calibrate the signal of each PMT, the “relative” and “absolute” gain values are
561 measured. The relative gain is the variation of gain among each of the PMTs whereas
562 the absolute gain is the average gain of all PMTs.

563 The relative gain is calibrated as follows. A laser is used to generate two measure-
564 ments: a high-intensity flash that illuminates every PMT with a sufficient number of
565 photons, and a low-intensity flash in which only a small number of PMTs collect light.
566 The first measurement creates an average charge, $Q_{obs}(i)$ on PMT i , whereas the second
567 measurement ensures that each hit PMT only generates a single photoelectron. For the
568 low-intensity measurement, the number of times each PMT records a charge larger
569 than 1/4 photoelectrons, $N_{obs}(i)$, is counted. The values measured can be expressed as

$$\begin{aligned} Q_{obs}(i) &\propto I_H \times f(i) \times \epsilon(i) \times G(i), \\ N_{obs}(i) &\propto I_L \times f(i) \times \epsilon(i), \end{aligned} \tag{1.16}$$

570 Where I_H and I_L is the intensity of the high and low flashes, $f(i)$ is the acceptance
571 efficiency of the i^{th} PMT, $\epsilon(i)$ is the product of the quantum and collection efficiency
572 of the i^{th} PMT and $G(i)$ is the gain of the i^{th} PMT. The relative gain for each PMT can
573 determined by taking the ratio of these quantities.

574 The absolute gain calibration is performed by observing fixed energy γ -rays of
575 $E_\gamma \sim 9\text{MeV}$ emitted isotropically from neutron capture on a NiCf source situated at
576 the center of the detector. This generates a photon yield of about 0.004 photoelec-

577 trons/PMT/event, meaning that $> 99\%$ of PMT signals are generated from single
578 photoelectrons. A charge distribution is generated by performing this calibration over
579 all PMTs, and the average value of this distribution is taken to be the absolute gain
580 value.

581 As mentioned in subsection 1.4.1, the average quantum and collection efficiency
582 for the SK detector is $\sim 21\%$ and $> 70\%$ respectively. However, these values do differ
583 between each PMT and need to be calibrated accordingly. Consequently, the NiCf
584 source is also used to calibrate the “quantum \times collection” efficiency (denoted “QE”)
585 value of each PMT. The NiCf low-intensity source is used as the PMT hit probability
586 is proportional to the QE ($N_{obs}(i) \propto \epsilon(i)$ in Equation 1.16). A Monte Carlo prediction
587 which includes photon absorption, scattering, and reflection is made to estimate the
588 number of photons incident on each PMT and the ratio of the number of predicted
589 to observed hits is calculated. The difference is attributed to the QE efficiency of that
590 PMT. This technique is extended to calculate the relative QE efficiency by normalizing
591 the average of all PMTs which removes the dependence on the light intensity.

592 Due to differing cable lengths and readout electronics, the timing response between
593 a photon hitting the PMT and the signal being captured by the data acquisition can be
594 different between each PMT. Due to threshold triggers (Described in subsection 1.4.3),
595 the time at which a pulse reaches a threshold is dependent upon the size of the pulse.
596 This is known as the ‘time-walk’ effect and also needs to be accounted for in each PMT.
597 To calibrate the timing response, a pulse of light with width 0.2ns is emitted into the
598 detector through a diffuser. Two-dimensional distributions of time and pulse height
599 (or charge) are made for each PMT and are used to calibrate the timing response. This
600 is performed in-situ **whilst during** data taking with the light source pulsing at 0.03Hz.

601 The top/bottom water quality asymmetry is measured using the NiCf calibration
602 data and cross-referencing these results to the “standard PMTs”. The water attenuation

length is continuously measured by the rate of vertically-downgoing cosmic-ray muons which enter via the top of the tank.

1.4.3 Data Acquisition and Triggering

Dark noise is the phenomenon where a PMT registers a pulse that is consistent with a single photoelectron emitted from photon detection despite the PMT being in complete darkness. This is predominately caused by two processes. Firstly there is intrinsic dark noise which is where photoelectrons gain enough thermal energy to be emitted from the photocathode, and secondly, the radioactive decay of contaminants inside the structure of the PMT. Typical dark noise rate for PMTs used within SK are $O(3)$ kHz [81] [which equates to about 12 dark noise hits per 220ns](#). This is lower than the expected number of photons generated for a ‘high energy event’ (As described in subsection 1.4.4) but instability in this value can cause biases in reconstruction.

The analysis presented in this thesis only uses the SK-IV period of the SK experiment so this subsection focuses on the relevant points of the data acquisition and triggering systems to that SK period. The earlier data acquisition and triggering systems are documented in [91, 92].

Before the SK-IV period started, the existing front-end electronics were replaced with “QTC-Based Electrons with Ethernet, QBEE” systems [93]. When the QBEE observes a signal above a 1/4 photoelectron threshold, the charge-to-time (QTC) converter generates a rectangular pulse. The start of the rectangular pulse indicates the time at which the analog photoelectron signal was received and the width of the pulse indicates the total charge integrated throughout the signal. This is then digitized by time-to-digital converters and sent to the “front-end” PCs. The digitized signal from every QBEE is then chronologically ordered and sent to the “merger” PCs. It is

the merger PCs that apply the software trigger. Any triggered events are passed to the “organizer” PC. This sorts the data stream of multiple merger PCs into chronologically ordered events which are then saved to disk. The schematic of data flow from PMTs to disk is illustrated in Figure 1.10.

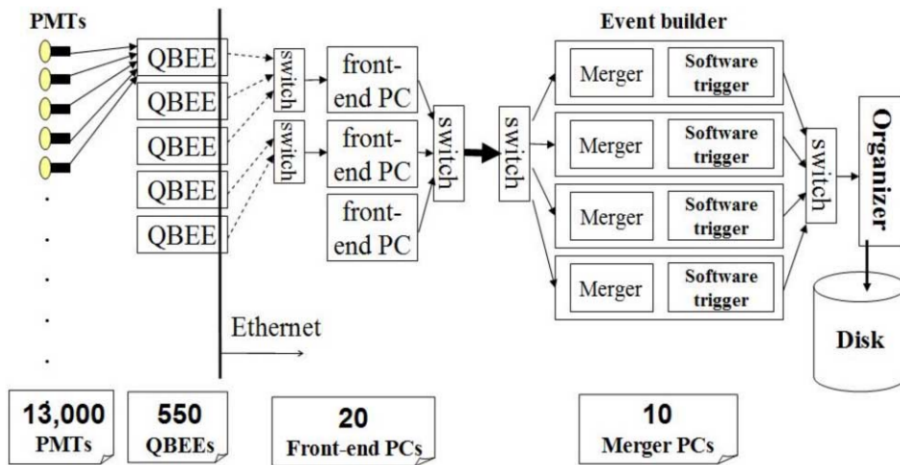


Figure 1.10: Schematic view of the data flow through the data acquisition and online system. Taken from [94].

The software trigger (described in [95]) operates by determining the number of PMT hits within a 200ns sliding window, $N_{200\mu s}$. **This window** coincides with the maximum time that a Cherenkov photon would take to traverse the length of the SK tank [92]. For lower energy events that generate fewer photons, this technique is useful for eliminating background processes like dark noise and radioactive decay which would be expected to separate in time. When the value of $N_{200\mu s}$ exceeds some threshold, a software trigger is issued. There are several trigger thresholds used within the SK-IV period which are detailed in Table 1.2. If one of these thresholds is met, the PMT hits within an extended time window are also read out and saved to disk. In the special case of an event that exceeds the SHE trigger but does not exceed the OD trigger, the AFT trigger looks for delayed coincidences of 2.2MeV gamma rays emitted from neutron capture in a $535\mu s$ window after the SHE trigger. A similar but more

⁶⁴³ complex “Wideband Intelligent Trigger (WIT)” has been deployed and is described
⁶⁴⁴ in [96].

| Trigger | Acronym | Condition | Extended time window (μs) |
|-------------------|---------|----------------|--|
| Super Low Energy | SLE | >34/31 hits | 1.3 |
| Low Energy | LE | >47 hits | 40 |
| High Energy | HE | >50 hits | 40 |
| Super High Energy | SHE | >70/58 hits | 40 |
| Outer Detector | OD | >22 hits in OD | N/A |

Table 1.2: The trigger thresholds and extended time windows saved around an event which were utilised throughout the SK-IV period. The exact thresholds can change and the values listed here represent the thresholds at the start and end of the SK-IV period.

⁶⁴⁵ 1.4.4 Cherenkov Radiation

⁶⁴⁶ Cherenkov light is emitted from any highly energetic charged particle traveling with
⁶⁴⁷ relativistic velocity, β , greater than the local speed of light in a medium [97]. Cherenkov
⁶⁴⁸ light is formed at the surface of a cone with characteristic pitch angle,

$$\cos(\theta) = \frac{1}{\beta n}. \quad (1.17)$$

⁶⁴⁹ where n is the refractive index of the medium. Consequently, the Cherenkov
⁶⁵⁰ momentum threshold, P_{thres} , is dependent upon the mass, m , of the charged particle
⁶⁵¹ moving through the **media medium**,

$$P_{thres} = \frac{m}{\sqrt{n^2 - 1}} \quad (1.18)$$

652 For water, where $n = 1.33$, the Cherenkov threshold momentum and energy for
 653 various particles are given in Table 1.3. In contrast, γ -rays are detected indirectly via
 654 the combination of photons generated by Compton scattering and pair production.
 655 The threshold for detection in the SK detector is typically higher than the threshold
 656 for photon production. This is due to the fact that the attenuation of photons in the
 657 water means that typically $\sim 75\%$ of Cherenkov photons reach the ID PMTs. Then the
 658 collection and quantum efficiencies described in subsection 1.4.1 result in the number
 659 of detected photons being lower than the number of photons which reach the PMTs.

| Particle | Threshold Momentum (MeV) | Threshold Energy (MeV) |
|----------|--------------------------|------------------------|
| Electron | 0.5828 | 0.7751 |
| Muon | 120.5 | 160.3 |
| Pion | 159.2 | 211.7 |
| Proton | 1070.0 | 1423.1 |

Table 1.3: The threshold momentum and energy for a particle to generate Cherenkov light in ultrapure water, as calculated in Equation 1.17 in ultrapure water which has refractive index $n = 1.33$.

660 The Frank-Tamm equation [98] describes the relationship between the number of
 661 Cherenkov photons generated per unit length, dN/dx , the wavelength of the photons
 662 generated, λ , and the relativistic velocity of the charged particle,

$$\frac{d^2N}{dxd\lambda} = 2\pi\alpha \left(1 - \frac{1}{n^2\beta^2}\right) \frac{1}{\lambda^2}. \quad (1.19)$$

663 where α is the fine structure constant. For a 100MeV momentum electron, approx-
 664 imately 330 photons will be produced per centimeter in the $300\text{nm} \leq \lambda \leq 700\text{nm}$
 665 region which the ID PMTs are most sensitive to [81].

⁶⁶⁶ 1.5 The Tokai to Kamioka Experiment

⁶⁶⁷ The Tokai to Kamioka (T2K) experiment is a long-baseline neutrino oscillation experi-
⁶⁶⁸ ment located in Japan. Proposed in the early 2000s [99, 100] to replace K2K [101], T2K
⁶⁶⁹ was designed to observe electron neutrino appearance whilst precisely measuring
⁶⁷⁰ the oscillation parameters associated with muon neutrino disappearance [102]. The
⁶⁷¹ experiment consists of a neutrino beam generated at the Japan Proton Accelerator
⁶⁷² Research Complex (J-PARC), a suite of near detectors situated 280m from the beam
⁶⁷³ target, and the Super Kamiokande far detector positioned at a 295km baseline. The
⁶⁷⁴ cross-section view of the T2K experiment is drawn in Figure 1.11.

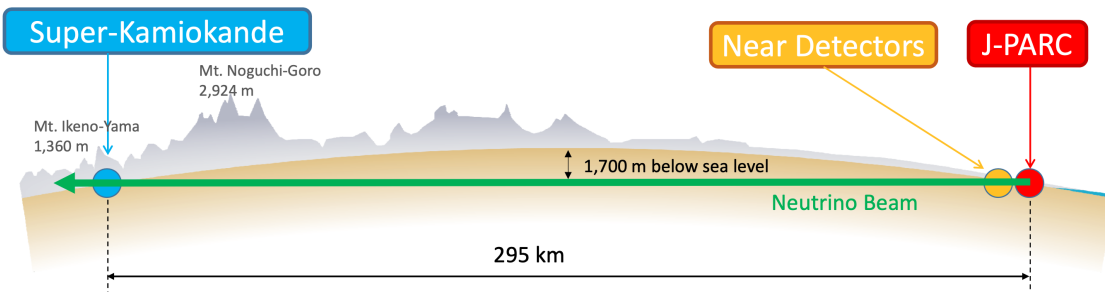


Figure 1.11: The cross-section view of the Tokai to Kamioka experiment illustrating the beam generation facility at J-PARC, the near detector situated at a baseline of 280m and the Super Kamiokande far detector situated 295km from the beam target.

⁶⁷⁵ The T2K collaboration makes world-leading measurements of the $\sin^2(\theta_{23})$, Δm_{23}^2 ,
⁶⁷⁶ and δ_{CP} oscillation parameters. Improvements in the precision and accuracy of pa-
⁶⁷⁷ rameter estimates are still being made by including new data samples and developing
⁶⁷⁸ the models which describe the neutrino interactions and detector responses [DB: Link](#)
⁶⁷⁹ to Christophe's slides from Nu2022. Electron neutrino appearance was first observed
⁶⁸⁰ at T2K in 2014 [103] ~~which accompanied a 7.3σ significance of a non-zero $\sin^2(\theta_{13})$~~
⁶⁸¹ [**measurement with \$7.3\sigma\$ significance.**](#)

682 The near detectors provide constraints on the beam flux and cross-section model
 683 parameters used within the fit by observing the unoscillated neutrino beam. There
 684 are a host of detectors situated in the near detector hall (As illustrated in Figure 1.12);
 685 ND280 (subsection 1.5.2), INGRID (subsection 1.5.3), NINJA [104], WAGASCI [105],
 686 and Baby-MIND [106]. The latter three are not currently used within the oscillation
 687 analysis presented within this thesis.

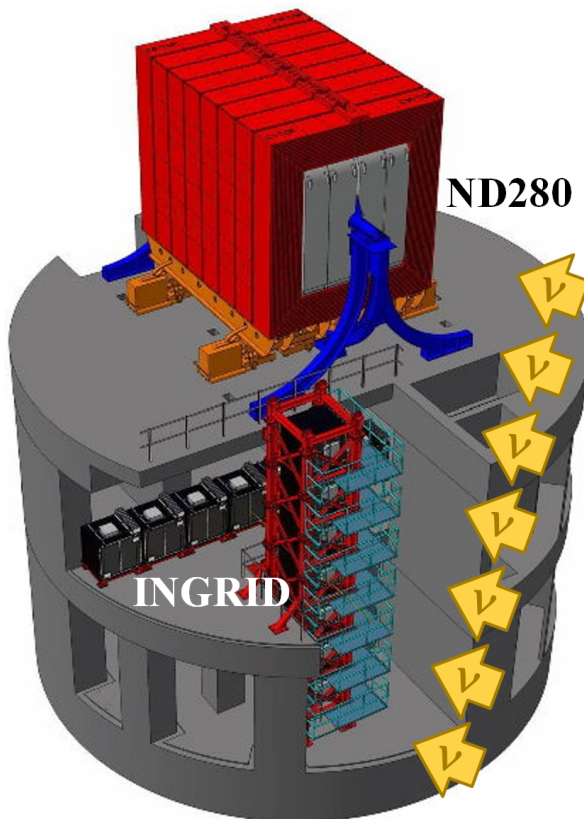


Figure 1.12: The near detector suite for the T2K experiment showing the ND280 and INGRID detectors. The distance between the detectors and the beam target is 280m.

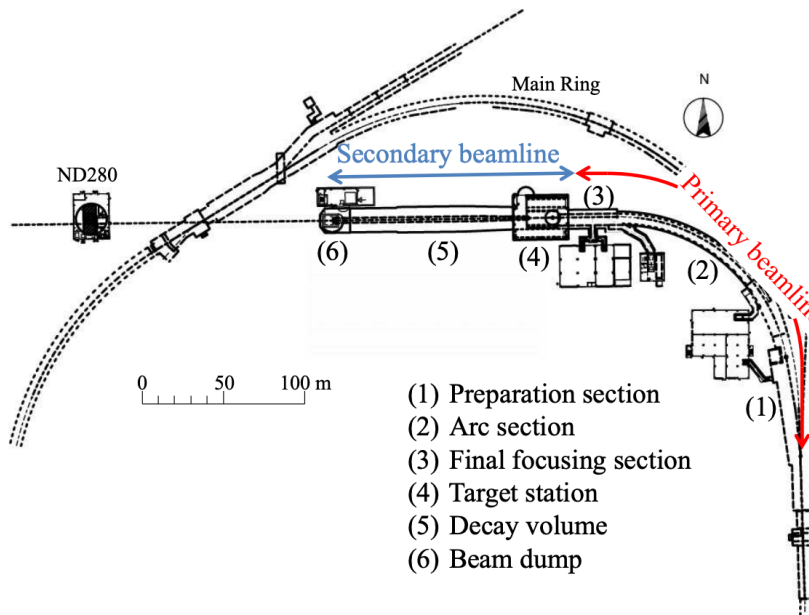
688 Whilst this thesis presents the ND280 in terms of its purpose for the oscillation
 689 analysis, the detector can also make many cross-section measurements at neutrino
 690 energies of $O(1)\text{GeV}$ for the different targets within the detector [107, 108]. These
 691 measurements are of equal importance as they can lead the way in determining the
 692 model parameters used in the interaction models for the future high-precision era of
 693 neutrino physics.

⁶⁹⁴ 1.5.1 The Neutrino Beam

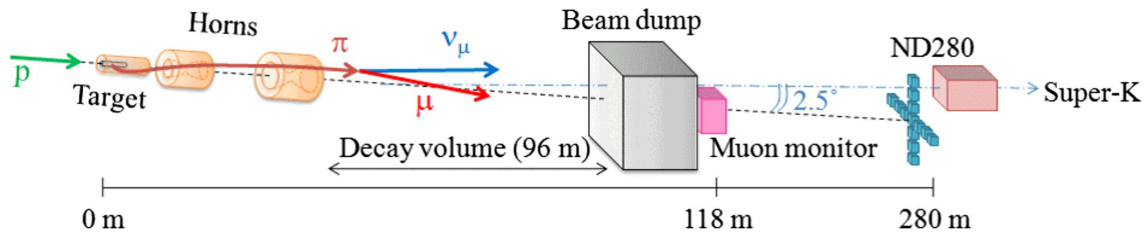
⁶⁹⁵ The neutrino beam used within the T2K experiment is described in [58, 109] and
⁶⁹⁶ summarised below. The accelerating facility at J-PARC is composed of two sections; the
⁶⁹⁷ primary and secondary beamlines. Figure 1.13 illustrates a schematic of the beamline,
⁶⁹⁸ focusing mostly on the components of the secondary beamline. The primary beamline
⁶⁹⁹ has three accelerators that progressively accelerate protons; a linear accelerator, a rapid-
⁷⁰⁰ cycling synchrotron, and the main-ring (MR) synchrotron. Once fully accelerated by
⁷⁰¹ the MR, the protons have a kinetic energy of 30GeV. Eight bunches of these protons,
⁷⁰² separated by 500ns, are extracted per “spill” from the MR and directed towards a
⁷⁰³ graphite target (A rod of length 91.4cm and diameter 2.6cm). Spills are extracted at
⁷⁰⁴ 0.5Hz with $\sim 3 \times 10^{14}$ protons contained per spill.

⁷⁰⁵ The secondary beamline consists of three main components; the target station, the
⁷⁰⁶ decay volume, and the beam dump. The target station is comprised of the target, beam
⁷⁰⁷ monitors, and three magnetic focusing horns. The proton beam interacts with the
⁷⁰⁸ graphite target to form a secondary beam of mostly pions and kaons. The secondary
⁷⁰⁹ beam travels through a 96m long decay volume, generating neutrinos through the
⁷¹⁰ following decays [58],

$$\begin{array}{ll}
\pi^+ \rightarrow \mu^+ + \nu_\mu & \pi^- \rightarrow \mu^- + \bar{\nu}_\mu \\
K^+ \rightarrow \mu^+ + \nu_\mu & K^- \rightarrow \mu^- + \bar{\nu}_\mu \\
& \rightarrow \pi^0 + e^+ + \nu_e & \rightarrow \pi^0 + e^- + \bar{\nu}_e \\
& \rightarrow \pi^0 + \mu^+ + \nu_\mu & \rightarrow \pi^0 + \mu^- + \bar{\nu}_\mu \\
K_L^0 \rightarrow \pi^- + e^+ + \nu_e & K_L^0 \rightarrow \pi^+ + e^- + \bar{\nu}_e \\
& \rightarrow \pi^- + \mu^+ + \nu_\mu & \rightarrow \pi^+ + \mu^- + \bar{\nu}_\mu \\
\mu^+ \rightarrow e^+ + \bar{\nu}_\mu + \nu_e & \mu^- \rightarrow e^- + \nu_\mu + \bar{\nu}_e
\end{array}$$



(a) Primary and secondary beamline



(b) Secondary beamline

Figure 1.13: Top panel: Bird's eye view of the most relevant part of primary and secondary beamline used within the T2K experiment. The primary beamline is the main-ring proton synchrotron, kicker magnet, and graphite target. The secondary beamline consists of the three focusing horns, decay volume, and beam dump. Figure taken from [109]. Bottom panel: The side-view of the secondary beamline including the focusing horns, beam dump and neutrino detectors. Figure taken from [110].

712 The electrically charged component of the secondary beam is focused towards the

713 far detector by the three magnetic horns. These horns direct charged particles of a

714 particular polarity towards SK whilst defocusing the oppositely charged particles.

715 This allows a mostly neutrino or mostly antineutrino beam to be used within the

716 experiment, denoted as "forward horn current (FHC)" or "reverse horn current (RHC)"

717 respectively.

Figure 1.14 illustrates the different contributions to the FHC and RHC neutrino flux.

The low energy flux is dominated by the decay of pions whereas kaon decay becomes the dominant source of neutrinos for $E_\nu > 3\text{GeV}$. The “wrong-sign” component, which is the $\bar{\nu}_\mu$ background in a ν_μ beam, and the intrinsic irreducible ν_e background are predominantly due to muon decay for $E_\nu < 2\text{GeV}$. As the antineutrino cross-section is smaller than the neutrino cross-section, the wrong-sign component is more dominant in the RHC beam as compared to that in the FHC beam.

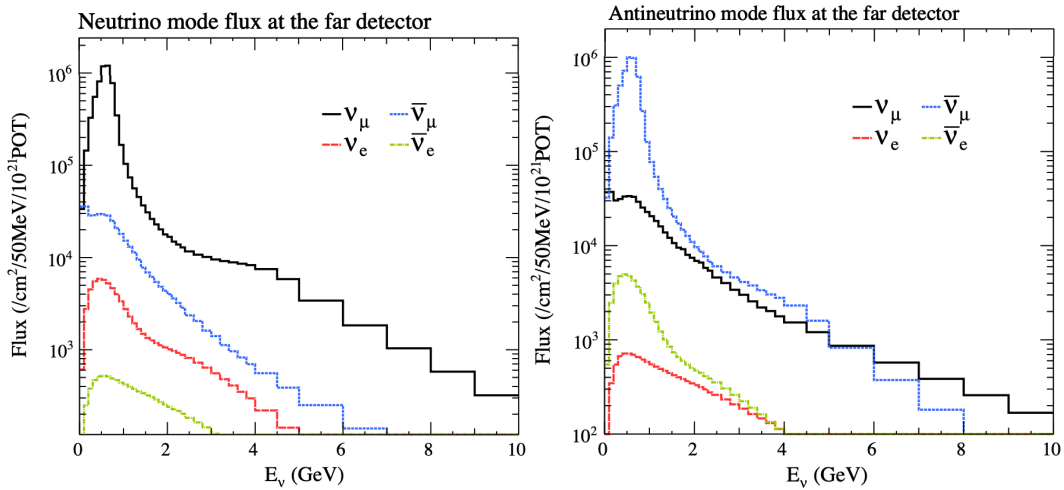


Figure 1.14: The Monte Carlo prediction of the energy spectrum for each flavour of neutrino (ν_e , $\bar{\nu}_e$, ν_μ and $\bar{\nu}_\mu$) in the neutrino dominated beam FHC mode (Left) and antineutrino dominated beam RHC mode (Right) expected at SK. Taken from [111].

The beam dump, situated at the end of the decay volume, stops all charged particles

other than highly energetic muons ($p_\mu > 5\text{GeV}$). The MuMon detector monitors the penetrating muons to determine the beam direction and intensity which is used to constrain some of the beam flux systematics within the analysis [110, 112].

The T2K experiment uses an off-axis beam to narrow the neutrino energy distribution.

This was the first implementation of this technique in a long-baseline neutrino oscillation experiment after its original proposal [113]. Pion decay, $\pi \rightarrow \mu + \nu_\mu$, is a two-body decay. Consequently, the neutrino energy, E_ν , can be determined based on the pion energy, E_π , and the angle at which the neutrino is emitted, θ ,

$$E_\nu = \frac{m_\pi^2 - m_\mu^2}{2(E_\pi - p_\pi \cos(\theta))}, \quad (1.20)$$

where m_π and m_μ are the mass of the pion and muon respectively. For a fixed energy pion, the neutrino energy distribution is dependent upon the angle at which the neutrinos are observed from the initial pion beam direction. For the 295km baseline at T2K, $E_\nu = 0.6\text{GeV}$ maximises the electron neutrino appearance probability, $P(\nu_\mu \rightarrow \nu_e)$, whilst minimising the muon disappearance probability, $P(\nu_\mu \rightarrow \nu_\mu)$. Figure 1.15 illustrates the neutrino energy distribution for a range of off-axis angles, as well as the oscillation probabilities most relevant to T2K.

1.5.2 The Near Detector at 280m

Whilst all the near detectors are situated in the same “pit” located at 280m from the beamline, the “ND280” detector is the off-axis detector which is situated at the same off-axis angle as the Super-Kamiokande far detector. It has two primary functions; firstly it measures the neutrino flux and secondly it counts the event rates of different types of neutrino interactions. Both of these constrain the flux and cross-section systematics invoked within the model for a more accurate prediction of the expected event rate at the far detector.

As illustrated in Figure 1.16, the ND280 detector consists of several sub-detectors. The most important part of the detector for this analysis is the tracker region. This is comprised of two time projection chambers (TPCs) sandwiched between three fine grain detectors (FGDs). The FGDs contain both hydrocarbon plastics and water targets for neutrino interactions and provide track reconstruction near the interaction vertex. The emitted charged particles can then propagate into the TPCs which pro-

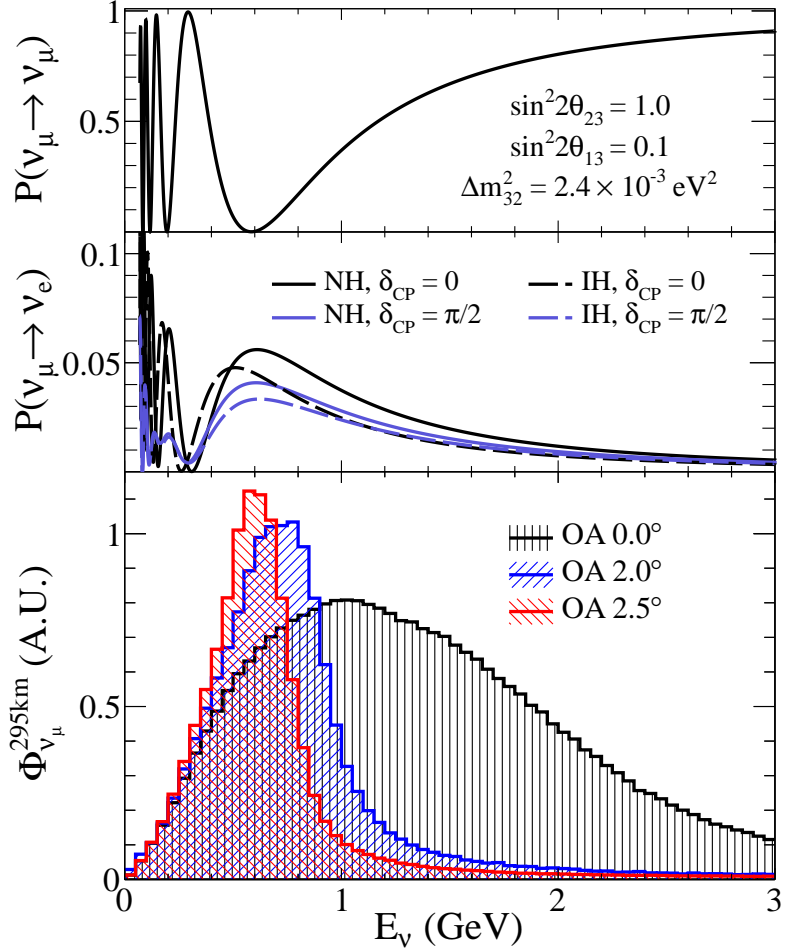


Figure 1.15: Top panel: T2K muon neutrino disappearance probability as a function of neutrino energy. Middle panel: T2K electron neutrino appearance probability as a function of neutrino energy. Bottom panel: The neutrino flux distribution for three different off-axis angles (Arbitrary units) as a function of neutrino energy.

vide particle identification and momentum reconstruction. The FGDs and TPCs are further described in subsubsection 1.5.2.1 and subsubsection 1.5.2.2 respectively. The electromagnetic calorimeter (ECAL) encapsulates the tracker region alongside the π^0 detector (P0D). The ECAL measures the deposited energy from photons emitted from interactions within the FGD. The P0D constrains the cross-section of neutral current interactions which generate neutral pions, which is one of the largest backgrounds in the electron neutrino appearance oscillation channel. The P0D and ECAL detectors are detailed in subsubsection 1.5.2.3 and subsubsection 1.5.2.4 respectively. The entire detector is located within a large yolk magnet which produces a 0.2T magnetic field.

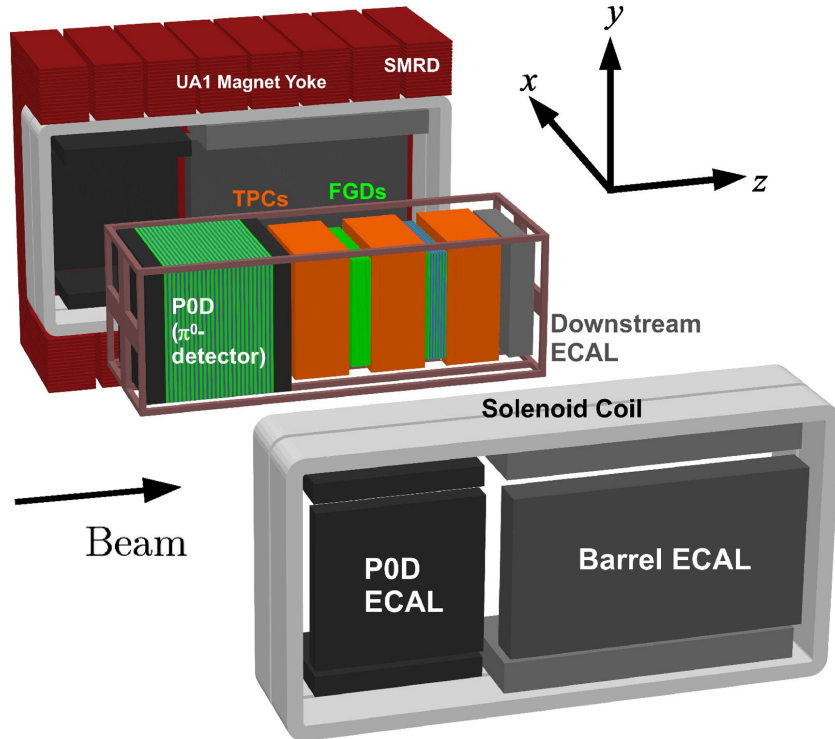


Figure 1.16: The components of the ND280 detector. The neutrino beam travels from left to right. Taken from [109].

This design of the magnet also includes a scintillating detector called the side muon range detector (SMRD) which is used to track high-angle muons as well as acting as a cosmic veto. The SMRD is described in subsubsection 1.5.2.5.

1.5.2.1 Fine Grained Detectors

The T2K tracker region is comprised of two fine grained detectors (FGD) and three Time Projection Chambers (TPC). A detailed description of the FGD design, construction, and assembly is found in [114] and summarised below. The FGDs are the primary target for neutrino interactions with a mass of 1.1 tonnes per FGD. Alongside this, the FGDs are designed to be able to track short-range particles which do not exit the FGD. Typically, short-range particles are low momentum and are observed as tracks that deposit a large amount of energy per unit length. This means the FGD needs good granularity to resolve these particles. The FGDs have the best timing resolution

⁷⁷⁶ ($\sim 3\text{ns}$) of any of the sub-detectors of the ND280 detector. As such, the FGDs are
⁷⁷⁷ used for time of flight measurements to determine forward going positively charged
⁷⁷⁸ particles from backward going negatively charged particles. Finally, any tracks which
⁷⁷⁹ pass through multiple sub-detectors are required to be track matched to the FGD.

⁷⁸⁰ Both FDGs are made from square scintillator planes of side length 186cm and width
⁷⁸¹ 2.02cm. Each plane consists of two layers of 192 scintillator bars in an XY orientation.
⁷⁸² A wave-length shift fiber is threaded through the center of each bar and is read out by
⁷⁸³ a multi-photon pixel counter (MPPC). FGD1 is the most upstream of the two FGDs
⁷⁸⁴ and contains 15 planes of carbon plastic scintillator which is a common target in
⁷⁸⁵ external neutrino scattering data. As the far detector is a pure water target, 7 of the 15
⁷⁸⁶ scintillator planes in FGD2 have been replaced with a hybrid water-scintillator target.
⁷⁸⁷ Due to the complexity of the nucleus, nuclear effects can not be extrapolated between
⁷⁸⁸ different nuclei. Therefore having the ability to take data on one target which is the
⁷⁸⁹ same as external data and another target which is the same as the far detector target is
⁷⁹⁰ beneficial for reliable model parameter estimates.

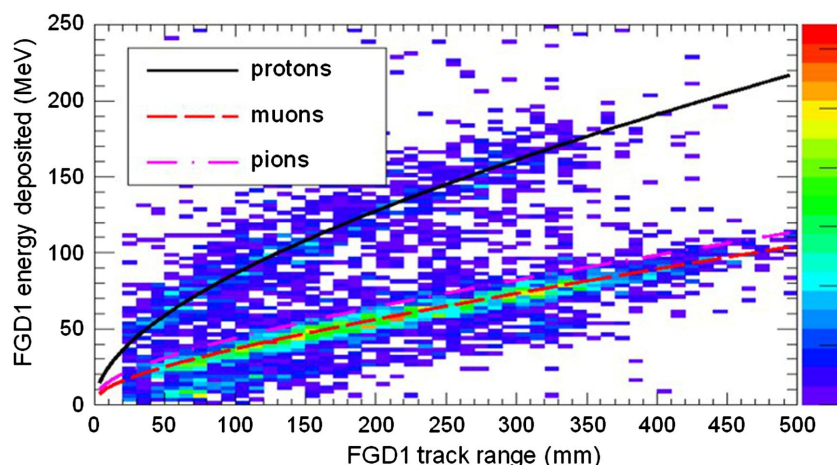


Figure 1.17: Comparison of data to Monte Carlo prediction of integrated deposited energy as a function of track length for particles that stopped in FGD1. Taken from [114].

791 The integrated deposited energy is used for particle identification. The FGD

792 can distinguish protons from other charged particles by comparing the integrated

793 deposited energy from data to Monte Carlo prediction as seen in Figure 1.17.

794 **1.5.2.2 Time Projection Chambers**

795 The majority of particle identification and momentum measurements within ND280

796 are provided by three Time Projection Chambers (TPCs) [115]. The TPCs are located

797 on either side of the FGDs. They are located inside of the magnetic field meaning the

798 momentum of a charged particle can be determined from the bending of the track.

799 Each TPC module consists of two gas-tight boxes, as shown in Figure 1.18, which

800 are made of non-magnetic material. The outer box is filled with CO₂ which acts as

801 an electrical insulator between the inner box and the ground. The inner box forms

802 the field cage which produces a uniform electric drift field of $\sim 275\text{V/cm}$ and an

803 argon gas mixture. Charged particles moving through this gas mixture ionize the gas

804 mixture. The ionised charge is drifted towards micromega detectors which measure

805 the ionization charge. The time and position information in the readout allows a

806 three-dimensional image of the neutrino interaction.

807 The particle identification of tracks that pass through the TPCs is performed using

808 dE/dx measurements. Figure 1.19 illustrates the data to Monte Carlo distributions

809 of the energy lost by a charged particle passing through the TPC as a function of the

810 reconstructed particle momentum. The resolution is $7.8 \pm 0.2\%$ meaning that electrons

811 and muons can be distinguished. This allows reliable measurements of the intrinsic ν_e

812 component of the beam.

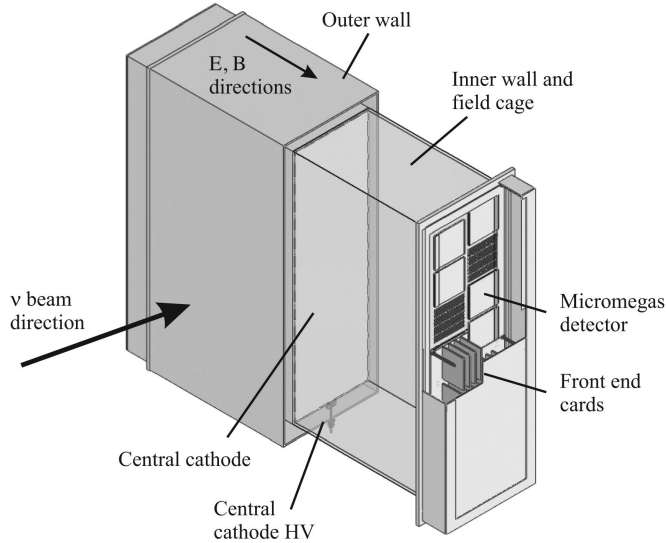


Figure 1.18: Schematic design of a Time Projection Chamber detector. Taken from [115].

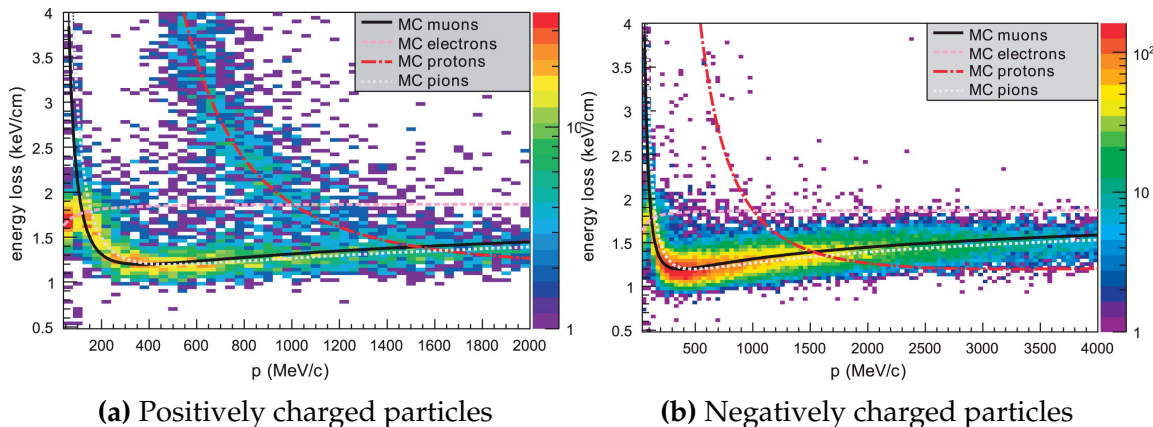


Figure 1.19: The distribution of energy loss as a function of reconstructed momentum for charged particles passing through the TPC, comparing data to Monte Carlo prediction. Taken from [115].

813 1.5.2.3 π^0 Detector

814 If one of the γ -rays from a $\pi^0 \rightarrow 2\gamma$ decay is missed at the far detector, the reconstruc-
 815 tion will determine that event to be electron-like. This is one of the main backgrounds
 816 hindering the electron neutrino appearance searches. Therefore, the π^0 detector (P0D)
 817 measures the cross-section of the neutral current induced neutral pion production on
 818 a water target.

The P0D is a cube of approximately 2.5m length. The P0D consists of layers of scintillating bars, brass and lead sheets, and water bags as illustrated in Figure 1.20. Two electromagnetic calorimeters are positioned at the most upstream and most downstream position in the sub-detector and the water target is situated in between them. The scintillator layers are built from two triangular bars orientated in opposite directions to form a rectangular layer. Each triangular scintillator bar is threaded with optical fiber which is read out by MPPCs. The high-Z brass and lead regions produce electron showers from the photons emitted in π^0 decay.

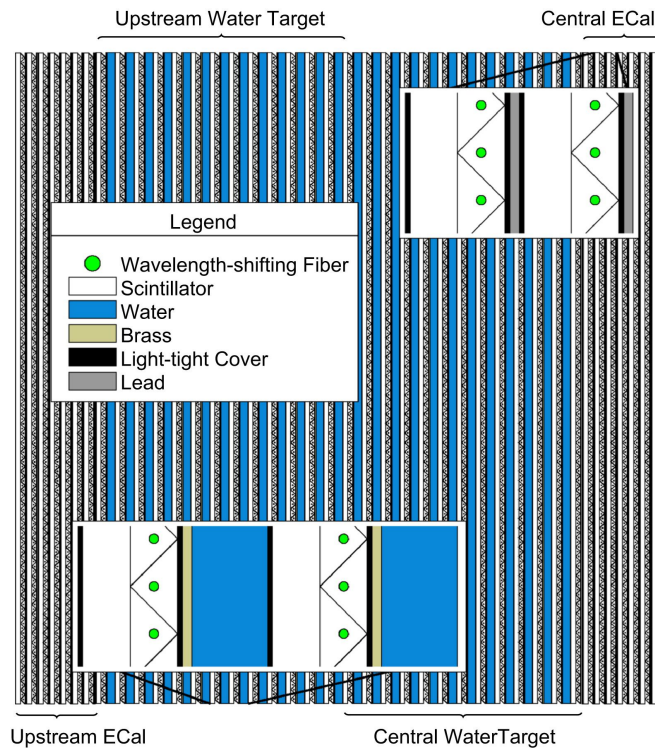


Figure 1.20: A schematic of the P0D side-view. Taken from [116].

The sub-detector can generate measurements of NC1 π^0 cross-sections on a water target by measuring the event rate both with and without the water target, with the cross-section on a water target being determined as the difference. The total active mass is 16.1 tonnes when filled with water and 13.3 tonnes when empty.

831 **1.5.2.4 Electromagnetic Calorimeter**

832 The electromagnetic calorimeter [117] (ECal) encapsulates the P0D and tracking sub-
833 detectors. Its primary purpose is to aid π^0 reconstruction from any interaction in
834 the tracker. To do this, it measures the energy and direction of photon showers from
835 $\pi^0 \rightarrow 2\gamma$ decay. It can also distinguish pion and muon tracks depending on the shape
836 of the photon shower deposited.

837 The ECal is comprised of three sections; the P0D ECal which surrounds the P0D,
838 the barrel ECal which encompasses the tracking region, and the downstream ECal
839 which is situated downstream of the tracker region. The barrel and downstream
840 ECals are tracking calorimeters that focus on electromagnetic showers from high-angle
841 particles emitted from the tracking sub-detectors. Particularly in the TPC, high-angle
842 tracks (those which travel perpendicularly to the beam-axis) can travel along a single
843 scintillator bar resulting in very few hits. The width of the barrel and downstream
844 ECal corresponds to ~ 11 electron radiation lengths to ensure $\sim 50\%$ of the energy of
845 the π^0 is contained. As the P0D has its own calorimetry which reconstructs showers,
846 the P0D ECal determines the energy which escapes the P0D.

847 Each ECal is constructed of multiple layers of scintillating bars sandwiched between
848 lead sheets. The scintillating bars are threaded with optical fiber and read out by
849 MPPCs. Each sequential layer of the scintillator is orientated perpendicular to the
850 previous which allows a two-dimensional readout, which when temporal, information
851 is included results in three-dimension event displays. The target mass of the P0D ECal,
852 barrel ECal, and downstream ECal are 1.50, 4.80 and 6.62 tonnes respectively.

⁸⁵³ **1.5.2.5 Side Muon Range Detector**

⁸⁵⁴ As illustrated in Figure 1.16, the ECal, FGDs, P0D, and TPCs are enclosed within the
⁸⁵⁵ UA1 magnet. Originally designed for the NOMAD [118] experiment and reconditioned
⁸⁵⁶ for use in the T2K experiment [119], the UA1 magnet provides a uniform horizontal
⁸⁵⁷ magnetic field of $0.2 \pm 2 \times 10^{-4}$ T.

⁸⁵⁸ Built into the UA1 magnet, the side muon range detector (SMRD) [120] monitors
⁸⁵⁹ high-energy muons which leave the tracking region and permeate through the ECal.
⁸⁶⁰ It additionally acts as a cosmic muon veto and trigger.

⁸⁶¹ **1.5.3 The Interactive Neutrino GRID**

⁸⁶² The Interactive Neutrino GRID (INGRID) detector is situated within the same “pit” as
⁸⁶³ the other near detectors. It is aligned with the beam in the “on-axis” position and mea-
⁸⁶⁴ sures the beam direction, spread, and intensity. The detector was originally designed
⁸⁶⁵ with 16 identical modules [109] (two modules have since been decommissioned) and a
⁸⁶⁶ “proton” module. The design of the detector is cross-shaped with length and height
⁸⁶⁷ 10m × 10m as illustrated in Figure 1.21.

⁸⁶⁸ Each module is composed of iron sheets interlaced with eleven tracking scintillator
⁸⁶⁹ planes for a total target mass of 7.1 tonnes per module. The scintillator design is an X-Y
⁸⁷⁰ pattern of 24 bars in both orientations, where each bar contains wave-length shifting
⁸⁷¹ fibers which are connected to multi-pixel photon counters (MPPCs). The MPPCs
⁸⁷² convert detected photons into electrical signals via photodiodes. This is then read
⁸⁷³ out by Trip-T front-end electronics [121] and passed to the readout merging modules
⁸⁷⁴ along with timing information from the clock module. Each module is encapsulated
⁸⁷⁵ inside veto planes to aid the rejection of charged particles entering the module.

876 The proton module is different from the other modules in that it consists of entirely
 877 scintillator planes with no iron target. The scintillator bars are also smaller than those
 878 used in the other modules to increase the granularity of the detector and improve
 879 tracking capabilities. The module sits in the center of the beamline and is designed to
 880 give precise measurements of quasi-elastic charged current interactions to evaluate
 881 the performance of the Monte Carlo simulation of the beamline.

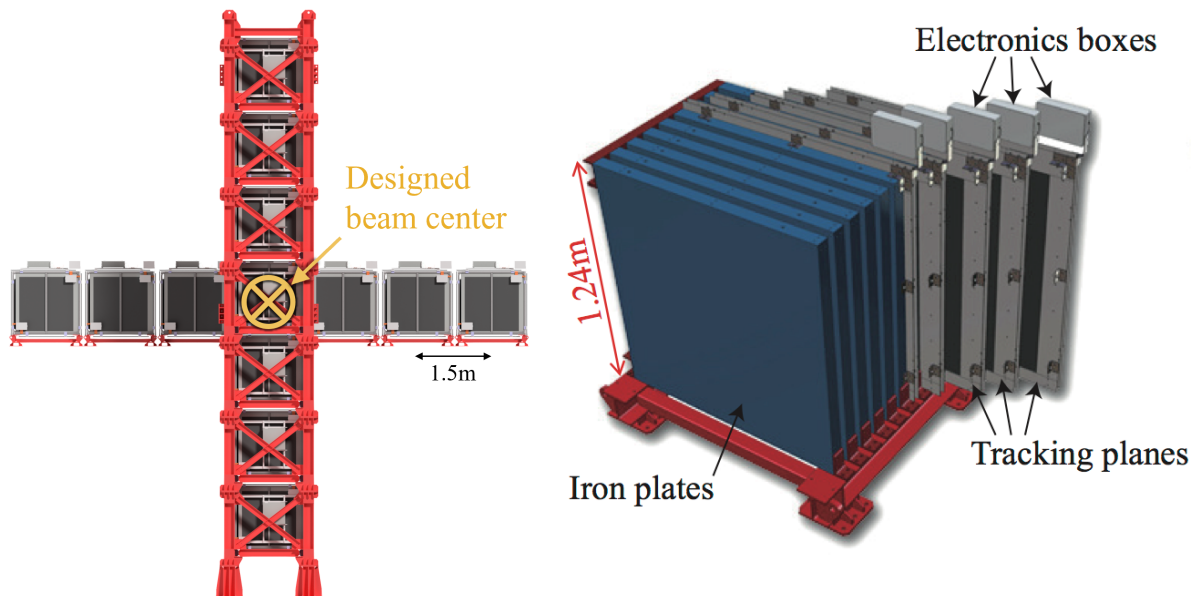


Figure 1.21: Left panel: The Interactive Neutrino GRID on-axis Detector. 14 modules are arranged in a cross-shape configuration, with the center modules being directly aligned with the on-axis beam. Right panel: The layout of a single module of the INGRID detector. Both figures are recreated from [109].

882 The INGRID detector can measure the beam direction to an uncertainty of 0.4mrad
 883 and the beam center within a resolution of 10cm [109]. The beam direction in both the
 884 vertical and horizontal directions is discussed in [122] and it is found to be in good
 885 agreement with the MUMON monitor described in subsection 1.5.1.

886 **Chapter 2**

887 **Bayesian Statistics and Markov Chain**
888 **Monte Carlo Techniques**

889 The analysis throughout this thesis is based upon a Bayesian oscillation analysis. To
890 extract the oscillation parameters, a Markov Chain Monte Carlo (MCMC) method is
891 used. This chapter explains the theory of how parameter estimates can be determined
892 using this technique and condenses the material found in the literature [123–126].

893 The oscillation parameter determination presented within this thesis is built upon a
894 simultaneous fit to the near detector, far detector beam, and atmospheric neutrino data.
895 In total, there are four oscillation parameters of interest ($\sin^2(\theta_{23})$, $\sin^2(\theta_{13})$, Δm_{23}^2 ,
896 and δ_{CP}), two oscillation parameters to which this study will not be sensitive ($\sin^2(\theta_{12})$
897 , Δm_{12}^2) and many nuisance parameters that control the systematic uncertainty models
898 invoked within this study. The systematic uncertainties can be grouped into categories
899 depending on how they are defined; 574 bin-normalisations due to the near detector
900 response, 45 bin-normalisations to describe the far detector response to neutrino beam
901 events, 27 parameters to describe the detector response to atmospheric neutrino events,
902 100 to model the bin-normalisation due to beam flux uncertainties, 18 which model the
903 atmospheric flux uncertainties, and 87 to describe the correlated cross-section model.
904 An alternative parameterisation, where the far detector response is correlated between
905 the beam and atmospheric samples, replaces the bin-normalisation parameters with
906 224 shift and smear systematics. Section [DB: Link to Systematics Chapter](#) describes
907 the systematic model in more depth.

908 The MCMC technique generates a multi-dimensional probability distribution across
 909 all of the model parameters used in the fit. To determine the parameter estimate of a
 910 single parameter, this multi-dimensional object is integrated over all other parameters.
 911 This process is called Marginalisation and is further described in subsection 2.3.1.
 912 Monte Carlo techniques approximate the probability distribution of each parameter
 913 within the limit of generating infinite samples. As ever, generating a large number of
 914 samples is time and resource-dependent. Therefore, an MCMC technique is utilised
 915 within this analysis to reduce the required number of steps to sufficiently sample the
 916 parameter space. This technique is described in further detail in subsection 2.2.1.

917 **2.1 Bayesian Statistics**

918 According to Bayesian Inference, observables and parameters of a statistical model are
 919 treated on an equal footing. To estimate model parameters $\vec{\theta}$ from some data D , one
 920 needs to define the joint probability distribution $P(D|\vec{\theta})$ which can be described as the
 921 prior distribution for model parameters $P(\vec{\theta})$ and the likelihood of the data given the
 922 model parameters $P(D|\vec{\theta})$,

$$P(D, \vec{\theta}) = P(D|\vec{\theta})P(\vec{\theta}). \quad (2.1)$$

923 The prior distribution, $P(\vec{\theta})$, describes all previous knowledge about the parameters
 924 within the model. For example, if the risk of developing health problems is known
 925 to increase with age, the prior distribution would describe the increase. For the
 926 purpose of this analysis, the prior distribution is typically the best-fit values taken
 927 from external data measurements with a Gaussian uncertainty. The prior distribution

928 can also contain correlations between model parameters. In an analysis using Monte
 929 Carlo techniques, the likelihood of measuring some data assuming some set of model
 930 parameters is calculated by comparing the Monte Carlo prediction generated at that
 931 particular set of model parameters to the data.

932 It is parameter estimation that is important for this analysis and as such, we apply
 933 Bayes' theorem [127]. To calculate the probability for each parameter to have a certain
 934 value given the observed data $P(\vec{\theta}|D)$, known as the posterior distribution (often
 935 termed the posterior). This can be expressed as

$$P(\vec{\theta}|D) = \frac{P(D|\vec{\theta})P(\vec{\theta})}{\int P(D|\vec{\theta})P(\vec{\theta})d\vec{\theta}}. \quad (2.2)$$

936 The denominator in Equation 2.2 is the integral of the joint probability distribution
 937 over all values of all parameters used within the fit. For brevity, we say that the
 938 posterior distribution is

$$P(\vec{\theta}|D)\alpha P(D|\vec{\theta})P(\vec{\theta}). \quad (2.3)$$

939 In subsection 2.3.1, we see that for the cases used within this analysis, it is reason-
 940 able to know the posterior to some normalisation constant.

941 2.2 Monte Carlo Simulation

942 Monte Carlo techniques are used to numerically solve a complex problem that does
 943 not necessarily have an analytical solution. These techniques rely on building a large

944 ensemble of samples from an unknown distribution and then using the ensemble to
945 approximate the properties of the distribution.

946 An example that uses Monte Carlo techniques is to calculate the area underneath
947 a curve. For example, take the problem of calculating the area under a straight line
948 with gradient $M = 0.4$ and intercept $C = 1.0$. Analytically, one can calculate the area
949 under the line is equal to 30 units for $0 \leq x \leq 10$. Using Monte Carlo techniques,
950 one can calculate the area under this line by throwing many random values for the x
951 and y components of each sample and then calculating whether that point falls below
952 the line. The area can then be calculated by the ratio of points below the line to the
953 total number of samples thrown multiplied by the total area in which samples were
954 scattered. The study is shown in Figure 2.1 highlights this technique and finds the area
955 under the curve to be 29.9 compared to an analytical solution of 30.0. The deviation
956 of the numerical to analytical solution can be attributed to the number of samples
957 used in the study. The accuracy of the approximation in which the properties of the
958 Monte Carlo samples replicate those of the desired distribution is dependent on the
959 number of samples used. Replicating this study with a differing number of Monte
960 Carlo samples used in each study (As shown in Figure 2.2) highlights how the Monte
961 Carlo techniques are only accurate within the limit of a high number of samples.

962 Whilst the above example has an analytical solution, these techniques are just as
963 applicable to complex solutions. Clearly, any numerical solution is only as useful as its
964 efficiency. As discussed, the accuracy of the Monte Carlo technique is dependent upon
965 the number of samples generated to approximate the properties of the distribution.
966 Furthermore, if the positions at which the samples are evaluated are not 'cleverly'
967 picked, the efficiency of the Monte Carlo technique significantly drops. Given the
968 example in Figure 2.1, if the region in which the samples are scattered significantly
969 extends passed the region of interest, many calculations will be calculated but do

not add to the ability of the Monte Carlo technique to achieve the correct result. For instance, any sample evaluated at a $y \geq 5$ could be removed without affecting the final result. This does bring in an aspect of the ‘chicken and egg’ problem in that to achieve efficient sampling, one needs to know the distribution beforehand.

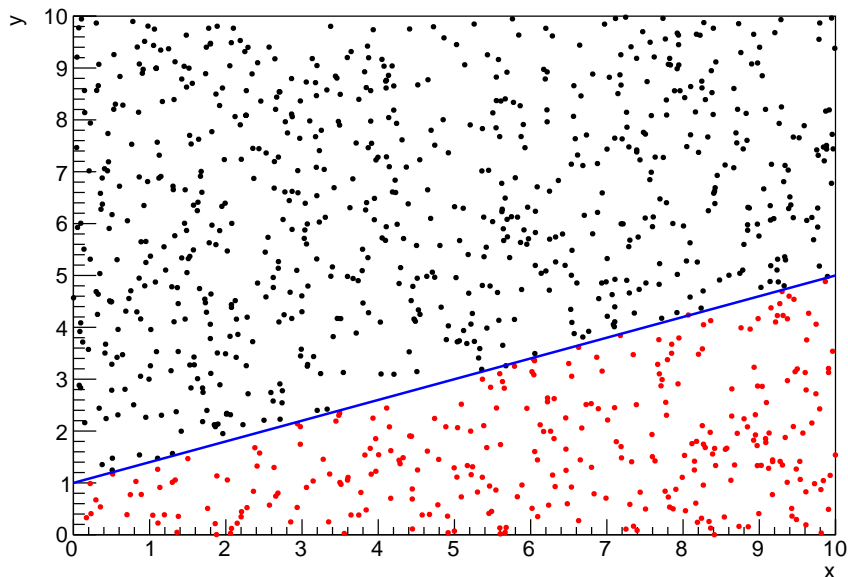


Figure 2.1: Example of using Monte Carlo techniques to find the area under the blue line. The gradient and intercept of the line are 0.4 and 1.0 respectively. The area found to be under the curve using one thousand samples is 29.9 units.

2.2.1 Markov Chain Monte Carlo

This analysis utilises a multi-dimensional probability distribution, with some dimensions being significantly more constrained than others. This could be from prior knowledge of parameter distributions from external data or un-physical regions in which parameters can not exist. Consequently, the Monte Carlo techniques used need to be as efficient as possible. For this analysis, the Markov Chain Monte Carlo (MCMC) technique is chosen. An MCMC technique is a Monte Carlo technique that uses a Markov chain to select which points at which to sample the parameter distribution.

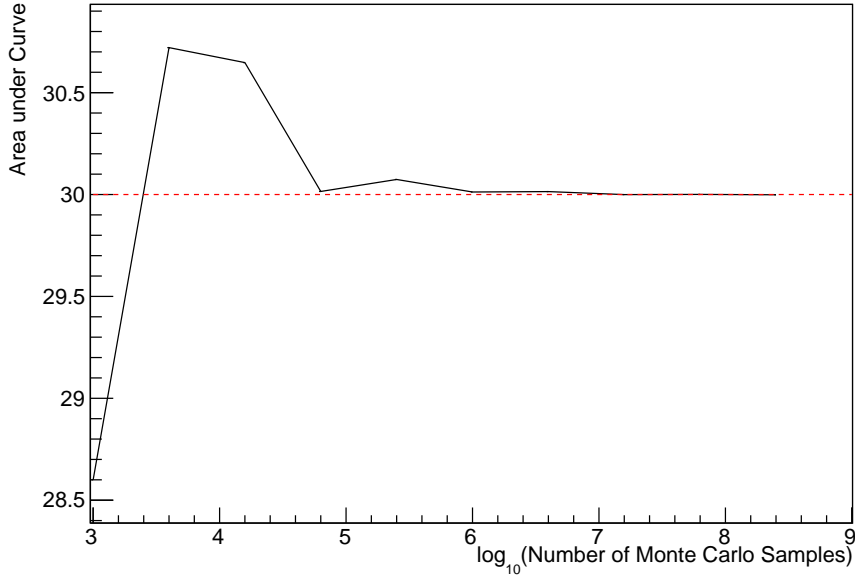


Figure 2.2: The area under a line of gradient 0.4 and intercept 1.0 for the range $0 \leq x \leq 10$ as calculated using Monte Carlo techniques as a function of the number of samples used in each repetition. The analytical solution to the area is 30 units as given by the red line.

982 This technique performs a semi-random stochastic walk through the allowable pa-
 983 rameter space. This builds a posterior distribution which has the property that the
 984 density of sampled points is proportional to the probability density of that parame-
 985 ter. This does mean that the samples produced by this technique are not statistically
 986 independent but they will cover the space of the distribution.

987 A Markov chain functions by selecting the position of step \vec{x}_{i+1} based on the
 988 position of \vec{x}_i . The space in which the Markov chain selects samples is dependent
 989 upon the total number of parameters utilised within the fit, where a discrete point in
 990 this space is described by the N-dimensional space \vec{x} . In a perfectly operating Markov
 991 chain, the position of the next step depends solely on the previous step and not on the
 992 further history of the chain (\vec{x}_0, \vec{x}_1 , etc.). However, in solving the multi-dimensionality
 993 of the fit used within this analysis, each step becomes correlated with several of
 994 the steps preceding itself. This behaviour is further explained in subsection 2.2.3.
 995 Providing the MCMC chain is well optimised, it will begin to converge towards a

996 unique stationary distribution. The period between the chain's initial starting point
997 and the convergence to the unique stationary distribution is colloquially known as the
998 burn-in period. This is discussed further in subsection 2.2.3. Once the chain reaches
999 the stationary distribution, all points sampled after that point will look like samples
1000 from that distribution.

1001 Further details of the theories underpinning MCMC techniques are discussed
1002 in [124] but can be summarised by the requirement that the chain satisfies the three
1003 'regularity conditions':

- 1004 • Irreducibility: From every position in the parameter space \vec{x} , there must exist a
1005 non-zero probability for every other position in the parameter space to be reached.
- 1006 • Recurrence: Once the chain arrives at the stationary distribution, every step fol-
1007 lowing from that position must be samples from the same stationary distribution.
- 1008 • Aperiodicity: The chain must not repeat the same sequence of steps at any point
1009 throughout the sampling period.

1010 The output of the chain after burn-in (ie. the sampled points after the chain
1011 has reached the stationary distribution) can be used to approximate the posterior
1012 distribution and model parameters $\vec{\theta}$. To achieve the requirement that the unique
1013 stationary distribution found by the chain be the posterior distribution, one can use
1014 the Metropolis-Hastings algorithm. This guides the stochastic process depending on
1015 the likelihood of the current proposed step compared to that of the previous step.
1016 Implementation and other details of this technique are discussed in subsection 2.2.2.

¹⁰¹⁷ 2.2.2 Metropolis-Hastings Algorithm

¹⁰¹⁸ As a requirement for MCMCs, the Markov chain implemented in this technique must
¹⁰¹⁹ have a unique stationary distribution that is equivalent to the posterior distribution.
¹⁰²⁰ To ensure this requirement and that the regularity conditions are met, this analysis
¹⁰²¹ utilises the Metropolis-Hastings (MH) algorithm [128,129]. For the i^{th} step in the chain,
¹⁰²² the MH algorithm determines the position in the parameter space to which the chain
¹⁰²³ moves to based on the current step, \vec{x}_i , and the proposed step, \vec{y}_{i+1} . The proposed step
¹⁰²⁴ is randomly selected from some proposal function $f(\vec{x}_{i+1}|\vec{x}_i)$, which depends solely
¹⁰²⁵ on the current step (ie. not the further history of the chain). The next step in the chain
¹⁰²⁶ \vec{x}_{i+1} can be either the current step or the proposed step determined by whether the
¹⁰²⁷ proposed step is accepted or rejected. To decide if the proposed step is selected, the
¹⁰²⁸ acceptance probability, $\alpha(\vec{x}_i, \vec{y}_i)$, is calculated as

$$\alpha(\vec{x}_i, \vec{y}_{i+1}) = \min\left(1, \frac{P(\vec{y}_{i+1}|D)f(\vec{x}_i|\vec{y}_{i+1})}{P(\vec{x}_i|D)f(\vec{y}_{i+1}|\vec{x}_i)}\right). \quad (2.4)$$

¹⁰²⁹ Where $P(\vec{y}_{i+1}|D)$ is the posterior distribution as introduced in section 2.1. To
¹⁰³⁰ simplify this calculation, the proposal function is required to be symmetric such that
¹⁰³¹ $f(\vec{x}_i|\vec{y}_{i+1}) = f(\vec{y}_{i+1}|\vec{x}_i)$. In practice, a multi-variate Gaussian distribution is used to
¹⁰³² throw parameter proposals from. This reduces Equation 2.4 to

$$\alpha(\vec{x}_i, \vec{y}_{i+1}) = \min\left(1, \frac{P(\vec{y}_{i+1}|D)}{P(\vec{x}_i|D)}\right). \quad (2.5)$$

1033 After calculating this quantity, a random number, β , is generated uniformly be-
1034 tween 0 and 1. If $\beta \leq \alpha(\vec{x}_i, \vec{y}_{i+1})$, the proposed step is accepted. Otherwise, the chain
1035 sets the next step equal to the current step and this procedure is repeated. This can be
1036 interpreted as if the posterior probability of the proposed step is greater than that of
1037 the current step, ($P(\vec{y}_{i+1}|D) \geq P(\vec{x}_i|D)$), the proposed step will always be accepted.
1038 If the opposite is true, ($P(\vec{y}_{i+1}|D) \leq P(\vec{x}_i|D)$), the proposed step will be accepted
1039 with probability $P(\vec{x}_i|D)/P(\vec{y}_{i+1}|D)$. This ensures that the Markov chain does not get
1040 trapped in any local minima in the potentially non-Gaussian posterior distribution.
1041 The outcome of this technique is that the density of steps taken in a discrete region is
1042 directly proportional to the probability density in that region.

1043 2.2.3 MCMC Optimisation

1044 As discussed in subsection 2.2.2, the proposal function invoked within the MH algo-
1045 rithm can take any form and the chain will still converge to the stationary distribution.
1046 As discussed in [DB: Link to Analysis Strategy Section](#), this analysis performs the
1047 Monte Carlo reweighting on an event-by-event basis. This requires significant com-
1048 putational resources to perform a parameter fit. Therefore, the number of steps taken
1049 before the unique stationary distribution is found should be minimised as only steps
1050 after convergence add information to the fit. Furthermore, the chain should entirely
1051 cover the allowable parameter space to ensure that all values have been considered.
1052 Tuning the distance that the proposal function jumps between steps on a parameter-
1053 by-parameter basis can both minimise the length of the burn-in period and ensure that
1054 the correlation between step \vec{x}_i and \vec{x}_j is sufficiently small.

1055 The effect of changing the width of the proposal function is highlighted in Figure 2.3.
1056 Three scenarios, each with the same underlying stationary distribution (A Gaussian of
1057 width 1.0 and mean 0.), are presented. The only difference between the three scenarios

is the width of the proposal function, colloquially known as the ‘step size σ ’. Each scenario starts at an initial parameter value of 10.0 which would be considered an extreme variation. For the case where $\sigma = 0.1$, it is clear to see that the chain takes a long time to reach the expected region of the parameter. This indicates that this chain would have a large burn-in period and does not converge to the stationary distribution until step ~ 500 . Furthermore, whilst the chain does move towards the expected region, each step is significantly correlated with the previous. Considering the case where $\sigma = 5.0$, the chain approaches the expected parameter region almost instantly meaning that the burn-in period is not significant. However, there are clearly large regions of steps where the chain does not move. This is likely due to the chain proposing steps in the tails of the distribution which have a low probability of being accepted. Consequently, this chain would take a significant number of steps to fully span the allowable parameter region. For the final scenario, where $\sigma = 0.5$, you can see a relatively small burn-in period of approximately 100 steps. Once the chain reaches the stationary distribution, it moves throughout the expected region of parameter values many times, sufficiently sampling the full parameter region. This example is a single parameter varying across a continuous distribution and does not fully reflect the difficulties in the many-hundred multi-variate parameter distribution used within this analysis. However, it does give a conceptual idea of the importance of selecting the proposal function and associated step size.

As discussed, step size tuning directly correlates to the average step acceptance rate. If the step size is too small, many steps will be accepted but the chain moves slowly. If the opposite is true, many steps will be rejected as the chain proposes steps in the tails of the distribution. Discussion in [130] suggests that the ‘ideal’ acceptance rate of a high dimension MCMC chain should be approximately $\sim 25\%$. An “ideal” step size [130] of

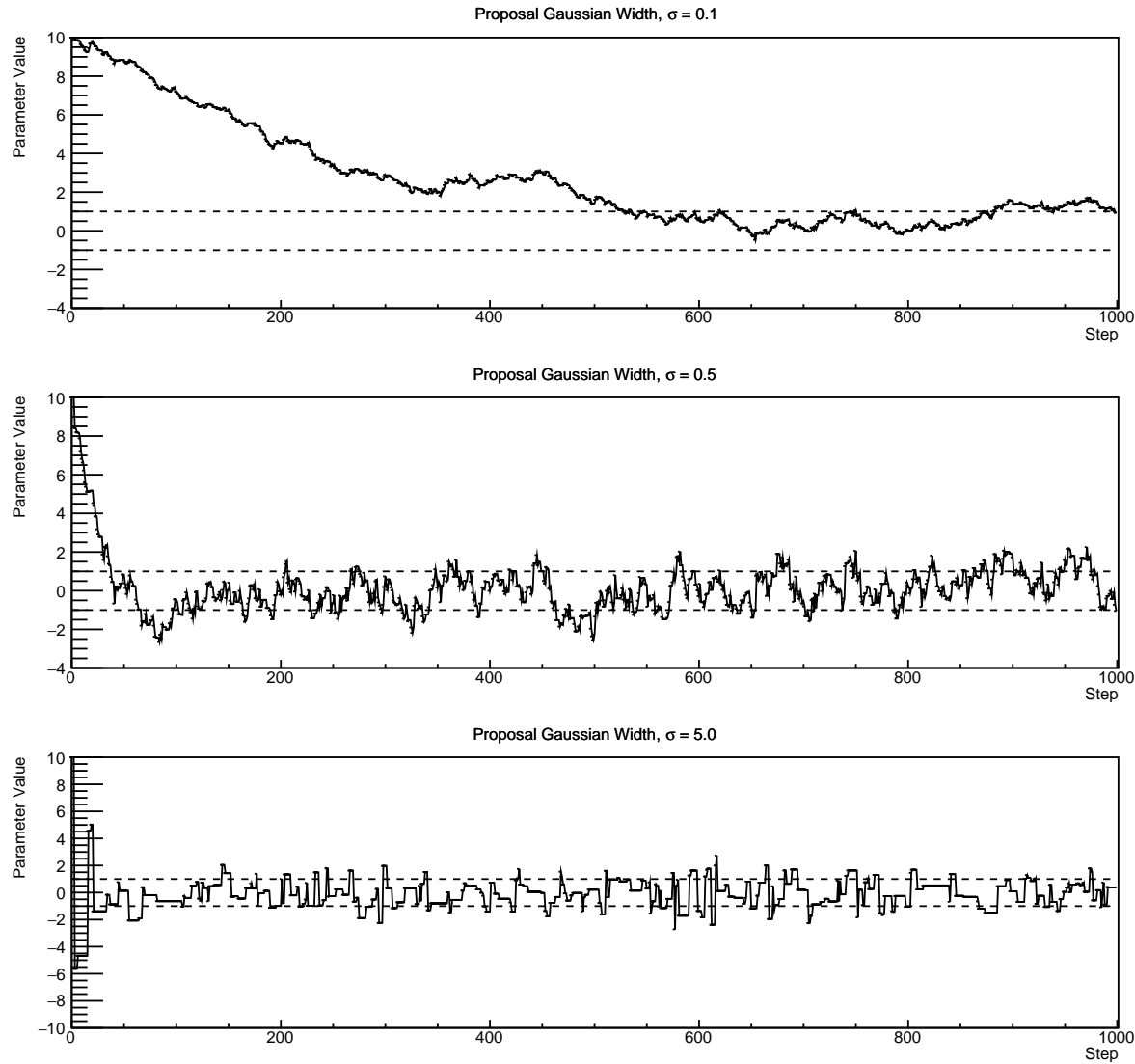


Figure 2.3: Three MCMC chains, each with a stationary distribution equal to a Gaussian centered at 0 and width 1 (As indicated by the black dotted lines). All of the chains use a Gaussian proposal function but have different widths (or ‘step size σ ’). The top panel has $\sigma = 0.1$, middle panel has $\sigma = 0.5$ and the bottom panel has $\sigma = 5.0$.

$$\sigma = \frac{2.4}{N_p}, \quad (2.6)$$

1084 where N_p is the number of parameters included in the MCMC fit. However, the
 1085 complex correlations between systematics mean that some parameters have to be hand

1086 tuned and many efforts have been taken to select a set of parameter-by-parameter step
1087 sizes to approximately reach the ideal acceptance rate.

1088 Figure 2.3 highlights the likelihood as calculated by the fit in [DB: Link to AsimovA](#)
1089 [Sensitivity Section](#) as a function of the number of steps in each chain. In practice,
1090 many independent MCMC chains are run simultaneously to parallelise the task of
1091 performing the fit. This figure overlays the distribution found in each chain. As seen,
1092 the likelihood decreases from its initial value and converges towards a stationary
1093 distribution after $\sim 1 \times 10^5$ steps. Each fit (whether it be different asimov fits or data
1094 fit) will have a different set of preferred parameter values which results in a different
1095 stationary distribution. For each fit presented in this thesis, a burn-in period of 1×10^5
1096 steps was found to be sufficient.

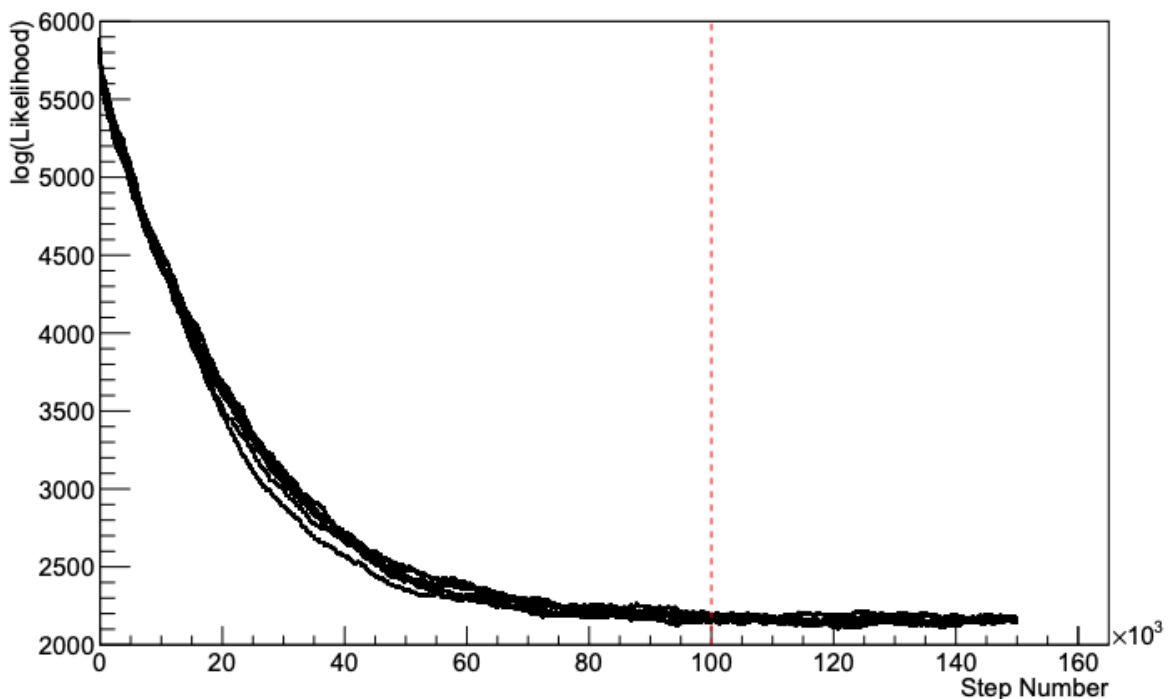


Figure 2.4: The log-likelihood from the fit detailed in [DB: Link to AsimovA](#) [Sensitivity Section](#) as a function of the number of steps accumulated in each fit. Many independent MCMC chains were run in parallel and overlaid on this plot. The red line indicates the 1×10^5 step burn-in period after which the log-likelihood becomes stable.

1097 2.3 Understanding the MCMC Results

1098 Whilst section 2.1 and section 2.2 describe how to interpret Bayesian statistics and
1099 explains the MCMC techniques used within this analysis, there is no mention of
1100 how to interpret the output of the chain. The posterior distribution output from the
1101 chain is a high dimension object, with as many dimensions as there are parameters
1102 included in the fit. However, this multi-dimensional object is difficult to conceptualize
1103 so parameter estimations are often presented in one or two-dimensional projections
1104 of this probability distribution. To do this, we invoke the marginalisation technique
1105 highlighted in subsection 2.3.1.

1106 2.3.1 Marginalisation

1107 The output of the MCMC chain is a highly dimensional probability distribution
1108 which is very difficult to interpret. From the standpoint of an oscillation analysis
1109 experiment, the one or two-dimensional ‘projections’ of the oscillation parameters of
1110 interest are most relevant. Despite this, the best fit values and uncertainties on the
1111 oscillation parameters of interest should correctly encapsulate the correlations to the
1112 other systematic uncertainties (colloquially called ‘nuisance’ parameters). For this joint
1113 beam and atmospheric analysis, the oscillation parameters of interest are $\sin^2(\theta_{23})$,
1114 $\sin^2(\theta_{13})$, Δm_{23}^2 , and δ_{CP} . All other parameters (Including the oscillation parameter
1115 this fit is insensitive to) are deemed nuisance parameters. To generate these projections,
1116 we rely upon integrating the posterior distribution over all nuisance parameters. This
1117 is called marginalisation. A simple example of this technique is to imagine the scenario
1118 where two coins are flipped. To determine the probability that the first coin returned
1119 a ‘head’, the exact result of the second coin flip is disregarded and simply integrated

1120 over. For the parameters of interest, $\vec{\theta}_i$, we can calculate the marginalised posterior by
1121 integrating over the nuisance parameters, $\vec{\theta}_n$. In this case, Equation 2.2 becomes

$$P(\vec{\theta}_i|D) = \frac{\int P(D|\vec{\theta}_i, \vec{\theta}_n)P(\vec{\theta}_i, \vec{\theta}_n)d\vec{\theta}_n}{\int P(D|\vec{\theta})P(\vec{\theta})d\vec{\theta}} \quad (2.7)$$

1122 Where $P(\vec{\theta}_i, \vec{\theta}_n)$ encodes the prior knowledge about the uncertainty and correlations
1123 between the parameters of interest and the nuisance parameters. In practice, this
1124 is simply taking the one or two-dimensional projection of the multi-dimensional
1125 probability distribution.

1126 Whilst in principle an easy solution to a complex problem, correlations between the
1127 interesting and nuisance parameters can bias the marginalised results. A similar effect
1128 is found when the parameters being marginalised over have non-Gaussian probability
1129 distributions. For example, Figure 2.5 highlights the marginalisation bias in the
1130 probability distribution found for a parameter when requiring a correlated parameter
1131 to have a positive parameter value. Due to the complex nature of this oscillation
1132 parameter fit presented in this thesis, there are certainly correlations occurring between
1133 the oscillation parameters of interest and the other nuisance parameters included in
1134 the fit.

1135 2.3.2 Parameter Estimation and Credible Intervals

1136 The purpose of this analysis is to determine the best fit values for the oscillation
1137 parameters that the beam and atmospheric samples are sensitive to; $\sin^2(\theta_{23})$, $\sin^2(\theta_{13})$
1138, Δm_{23}^2 , and δ_{CP} . Typically, the results presented take the form of one or two-dimension
1139 marginalised probability distributions for the appearance ($\sin^2(\theta_{13})$ and δ_{CP}) and

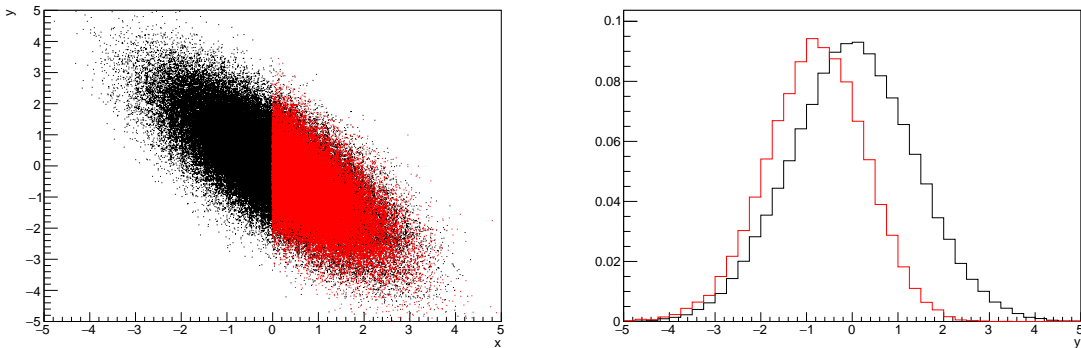


Figure 2.5: Left: The two dimensional probability distribution for two correlated parameters x and y . The red distribution shows the two dimensional probability distribution when $0 \leq x \leq 5$. Right: The marginalised probability distribution for the y parameter found when requiring the x to be bound between $-5 \leq x \leq 5$ and $0 \leq x \leq 5$ for the black and red distribution, respectively.

1140 disappearance ($\sin^2(\theta_{23})$ and Δm_{23}^2) parameters. The posterior probability density
 1141 taken from the output MCMC chain is binned in these parameters. The parameter
 1142 best-fit point is then taken to be the value that has the highest posterior probability.
 1143 This is performed in both one and two-dimensional projections.

1144 However, the single best-fit point in a given parameter is not of much use on its
 1145 own. We would also like to determine the uncertainty, or credible interval, on that
 1146 best-fit point. The definition of the 1σ credible interval is that we have 68% belief that
 1147 the parameter is within those bounds. For a more generalised definition, the credible
 1148 interval is the region of the posterior distribution that contains a specific fraction of
 1149 the total probability, such that

$$\int P(\theta|D)d\theta = \alpha \quad (2.8)$$

1150 Where θ is the parameter on which we calculate the credible interval. This technique
 1151 then calculates the $\alpha \times 100\%$ credible interval.

In practice, this analysis uses the highest posterior density (HPD) credible intervals which are calculated through the following method. First, the probability distribution is area-normalised such that it has an integrated area equal to 1.0. The bins of probability are then summed from the highest to lowest until the sum exceeds the 1σ level (0.68 in this example). This process is repeated for a range of credible intervals, notably the 1σ , 2σ and 3σ along with other levels where the critical values for each level can be found in [131]. This process can be repeated for the two-dimensional probability distributions by creating two-dimensional contours of credible intervals rather than a one-dimensional result.

2.3.3 Application of Bayes' Theorem

Due to the matter resonance, this analysis has some sensitivity to the mass hierarchy of neutrino states (whether Δm_{23}^2 is positive or negative) and the octant of $\sin^2(\theta_{23})$. The Bayesian approach utilised within this analysis gives an intuitive method of model comparison by determining which hypothesis is most favourable. Taking the ratio of Equation 2.3 for the two hypotheses of normal hierarchy, NH , and inverted hierarchy, IH , gives

$$\frac{P(\vec{\theta}_{NH}|D)}{P(\vec{\theta}_{IH}|D)} = \frac{P(D|\vec{\theta}_{NH})}{P(D|\vec{\theta}_{IH})} \times \frac{P(\vec{\theta}_{NH})}{P(\vec{\theta}_{IH})}. \quad (2.9)$$

The middle term defines the Bayes factor which is a data-driven interpretation of how strong the data prefers one hierarchy to the other. For this analysis, equal priors on both mass hierarchy hypotheses are chosen ($P(\vec{\theta}_{NH}) = P(\vec{\theta}_{IH}) = 0.5$). In practice, the MCMC chain proposes a value of $|\Delta m_{23}^2|$ and then applies a 50% probability that the value is sign flipped. Consequently, the Bayes factor can be calculated from

₁₁₇₃ the ratio of the probability density in either hypothesis. This equates to counting the
₁₁₇₄ number of steps taken in the normal and inverted hierarchies and taking the ratio. The
₁₁₇₅ same approach can be taken to compare the upper octant (UO) compared to the lower
₁₁₇₆ octant (LO) hypothesis of $\sin^2(\theta_{23})$.

₁₁₇₇ Whilst the value of the Bayes factor should always be shown, the Jeffreys scale [132]
₁₁₇₈ (highlighted in Table 2.1) gives an indication of the strength of preference for one model
₁₁₇₉ compared to the other. Other interpretations of the strength of preference of a model
₁₁₈₀ exist, e.g. the Kass and Raferty Scale [133].

| $\log_{10}(B_{AB})$ | B_{AB} | Strength of Preference |
|---------------------|--------------|--|
| < 0.0 | < 1 | No preference for hypothesis A (Supports hypothesis B) |
| 0.0 – 0.5 | 1.0 – 3.16 | Preference for hypothesis A is weak |
| 0.5 – 1.0 | 3.16 – 10.0 | Preference for hypothesis A is substantial |
| 1.0 – 1.5 | 10.0 – 31.6 | Preference for hypothesis A is strong |
| 1.5 – 2.0 | 31.6 – 100.0 | Preference for hypothesis A is very strong |
| > 2.0 | > 100.0 | Decisive preference for hypothesis A |

Table 2.1: Jeffreys scale for strength of preference for two models A and B as a function of the calculated Bayes factor ($B_{AB} = B(A/B)$) between the two models [132]. The original scale is given in terms of $\log_{10}(B(A/B))$ but converted to linear scale for easy comparison throughout this thesis.

₁₁₈₁ 2.3.4 Comparison of MCMC Output to Expectation

₁₁₈₂ Whilst not important for the extraction of oscillation parameters, understanding how
₁₁₈₃ the data constrains the model parameters is important to the understanding of this
₁₁₈₄ analysis. A simple method of doing this is to perform a comparison in the fitting
₁₁₈₅ parameters (For instance, the reconstructed neutrino energy and lepton direction for
₁₁₈₆ T2K far detector beam samples) of the spectra generated by the MCMC chain to ‘data’.
₁₁₈₇ This ‘data’ could be true data or some variation of Monte Carlo prediction. This allows
₁₁₈₈ easy comparison of the MCMC probability distribution to the data. To perform this, N

1189 steps from the post burn-in MCMC chain are randomly selected (Where for all plots
1190 of this style in this thesis, $N = 3000$). From these, the Monte Carlo prediction at each
1191 step is generated by reweighting the model parameters to the values specified at that
1192 step. Due to the probability density being directly correlated with the density of steps
1193 in a certain region, parameter values close to the best fit value are most likely to be
1194 selected.

1195 In practice, for each bin of the fitting parameters has a probability distribution
1196 of event rates, with one entry per sampled MCMC step. This distribution is binned
1197 where the bin with the highest probability is selected as the mean and an error on
1198 the width of this probability distribution is calculated using the approach highlighted
1199 in subsection 2.3.2. Consequently, the best fit distribution in the fit parameter is not
1200 necessarily that which would be attained by reweighting the Monte Carlo prediction
1201 to the most probable parameter values.

1202 A similar study can be performed to illustrate the freedom of the model parameter
1203 space prior to the fit. This can be done by throwing parameter values from the prior
1204 uncertainty of each parameter. This becomes troublesome for parameters with no
1205 prior uncertainty as the range is technically infinite. Where applicable solutions to
1206 remove these have been addressed.

₁₂₀₇ **Chapter 3**

₁₂₀₈ **Simulation, Reconstruction and Event Se-**
₁₂₀₉ **lections**

₁₂₁₀ **3.1 Simulation**

₁₂₁₁ In order to generate a Monte Carlo prediction of the expected event rate at the far
₁₂₁₂ detector for both sets of samples, all the processes in the beamline, atmospheric flux,
₁₂₁₃ neutrino interaction, and detector need to be modeled. The beamline simulation
₁₂₁₄ consists of three distinct parts; initial hadron interaction modeling, target station
₁₂₁₅ geometry and particle tracking and hadronic re-interactions. These are modeled by
₁₂₁₆ FLUKA [134], JNUBEAM [135, 136], and GCALOR [137], respectively. FLUKA is
₁₂₁₇ not very adaptable but matches external cross-section measurements in the region of
₁₂₁₈ interest better than GCALOR ($O(10)$ GeV). Thus a small simulation is built to model
₁₂₁₉ the interactions in the target and the output is then passed to JNUBEAM and GCALOR
₁₂₂₀ for propagation. The hadronic interactions are tuned to data from the NA61/SHINE
₁₂₂₁ [138–140] and HARP [141] experiments. The tuning is done by reweighting the FLUKA
₁₂₂₂ and GCALOR predictions to match the external data multiplicity and cross-section
₁₂₂₃ measurements, based on final state particle kinematics [142]. The predicted flux for
₁₂₂₄ neutrino and antineutrino beam modes is illustrated in Figure 1.14.

₁₂₂₅ The atmospheric neutrino flux predictions are simulated by the HKKM model
₁₂₂₆ [42, 44], where the primary cosmic ray flux is tuned to AMS [143] and BESS [144]

external data assuming the US-standard atmosphere '76 [145] density profile and includes geomagnetic field effects. Secondary interactions of pions and muons are handled by DPMJET-III [146] for energies above 32GeV and JAM [44, 147] for energies below that value. These hadronic interactions are tuned to external data [148, 149] using the same methodology as the tuning of the beamline simulation. The energy and cosine zenith predictions of $\nu_e, \bar{\nu}_e, \nu_\mu, \bar{\nu}_\mu$ flux are given in Figure 1.3 and Figure 1.5, respectively. The flux is approximately symmetrical and peaked around $\cos(\theta_Z) = 0.0$. This is because horizontally-going pions and kaons can travel further than their vertically-going counterparts resulting in a larger probability of decay to neutrinos. The symmetry is broken in low-energy neutrinos due to geomagnetic effects, which modify the track of the primary cosmic rays.

The neutrino interactions in all three detectors are simulated with NEUT [150, 151]. This simulates quasi-elastic (QE), meson exchange (MEC), single meson production (PROD), coherent pion production (COH), and deep inelastic scattering (DIS) interactions. These interaction categories can be further broken down by whether they were propagated via a W^\pm boson in Charged Current (CC) interactions or via a Z^0 boson in Neutral Current (NC) interactions. CC interactions have a charged lepton in the final state, which can be flavour-tagged in reconstruction to determine the flavour of the neutrino. In contrast, NC interactions have a neutrino in the final state so no flavour information can be determined from the observables in the detector. This is the reason why NC events are assumed to not oscillate within the analysis. Both CC and NC interactions are modeled for all the above interaction categories, other than MEC interactions which are only modeled for CC events. The SK detector is only sensitive to charged particles, so all charged current interactions are simulated whilst only neutral current processes that produce charged mesons (NCDIS, NCCOH, and NCPROD) are modeled. NC MEC interactions can only produce charged particles through secondary re-interactions which is a low cross-section process.

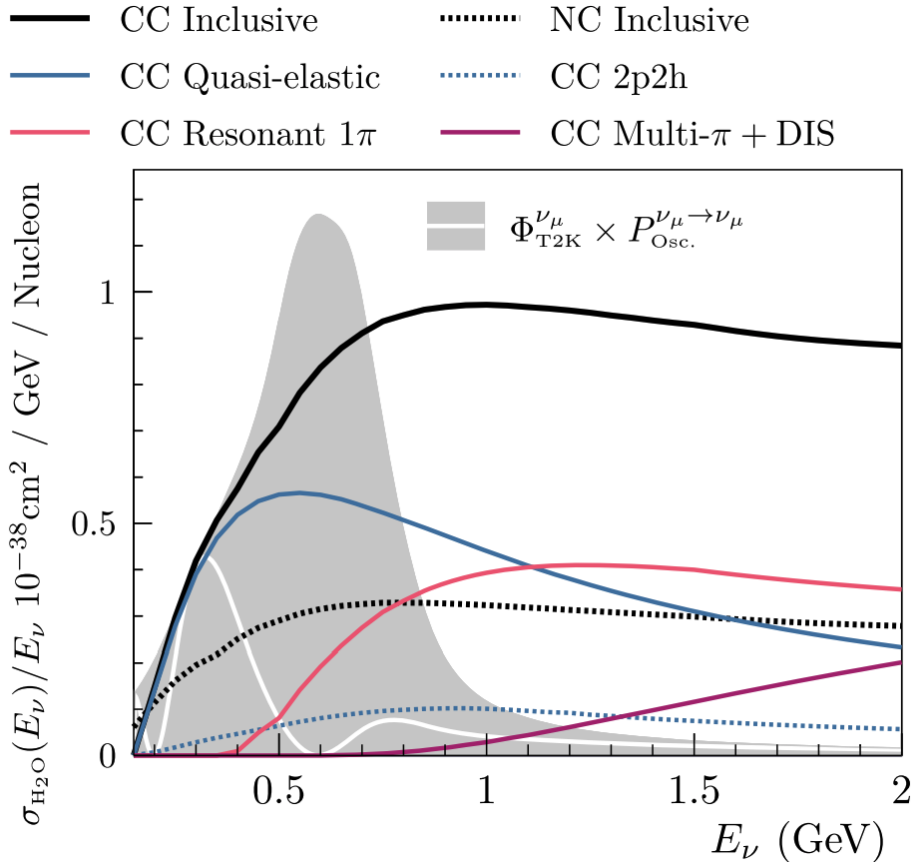


Figure 3.1: The NEUT prediction of the ν_μ -H₂O cross-section overlaid on the T2K ν_μ flux. The charged current (black, solid) and neutral current (black, dashed) inclusive, charged current quasi-elastic (blue, solid), charged current 2p2h (blue, dashed), charged current single pion production (pink), and charged current multi- π and DIS (Purple) cross-sections are illustrated. Taken from [150].

As illustrated in Figure 3.1, QE interactions dominate the low-energy cross-section of neutrino interactions. The NEUT implementation adopts the Llewellyn Smith [152] model for neutrino-nucleus interactions, where the nuclear ground state of any bound nucleons (neutrino-oxygen interactions) is approximated by a spectral-function [153] model that simulates the effects of Fermi momentum and Pauli blocking. The cross-section of QE interactions are controlled by vector and axial-vector form factors parameterised by the BBBA05 [154] model and a dipole form factor with $M_A^{QE} = 1.21 \text{ GeV}$ fit to external data [155], respectively. QE interactions only account for single-nucleon interactions whereas multi-nucleon interactions (or MEC) can contribute significantly to the overall cross-section. NEUT implements the Valencia [156] model

1264 to simulate MEC events, where two nucleons and two holes in the nuclear target are
1265 produced (Often called 2p2h interactions due to this effect).

1266 For neutrinos of energy $O(1)\text{GeV}$, PROD interactions become dominant. These
1267 predominantly produce charged and neutral pions although γ , kaon, and η production
1268 is also considered. To simulate these interactions, the Berger-Sehgal [157] model is
1269 implemented within NEUT. It simulates the excitation of a nucleon from a neutrino
1270 interaction, production of an intermediate baryon, and the consequential decay to a
1271 single meson or γ . Pions can also be produced through COH interactions, which occur
1272 when the incoming neutrino interacts with the entire oxygen nuclei target leaving a
1273 single pion outside of the nucleus. NEUT utilises the Berger-Sehgal [158] model to
1274 simulate these interactions.

1275 DIS and multi- π producing interactions become the most dominant for energies
1276 $> O(5)\text{GeV}$. PYTHIA [159] is used to simulate any interaction with invariant mass,
1277 $W > 2\text{GeV}/c^2$, which produces at least one meson. For any interaction which produces
1278 at least two mesons but has $W < 2\text{GeV}/c^2$, the Bronner model is invoked [160].
1279 Both of these models use Parton distribution functions based on the Bodek-Yang
1280 model [161–163].

1281 Any pion which is produced within the nucleus can re-interact through final state
1282 interactions before it exits, as illustrated by the scattering, absorption, production, and
1283 exchange interactions in Figure 3.2. These re-interactions alter the observable particles
1284 within the detector. For instance, if the charged pion from a CC PROD interaction
1285 is absorbed, the observables would mimic a CC QE interaction. To simulate these
1286 effects, NEUT uses a semi-classical intranuclear cascade model [150]. This cascade
1287 functions by stepping the pion through the nucleus in fixed-length steps equivalent
1288 to $dx = R_N/100$, where R_N is the radius of the nucleus. At each step, the Monte
1289 Carlo allows the pion to interact through scattering, charged exchange, absorption, or

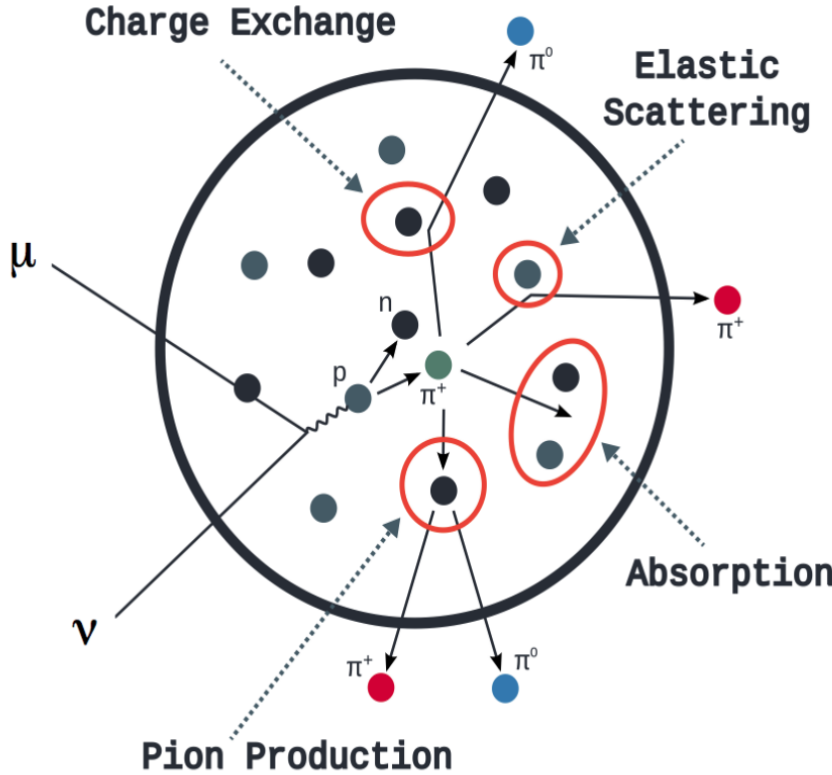


Figure 3.2: Illustration of the various processes which a pion can undergo before exiting the nucleus. Taken from [164].

1290 production with an interaction-dependent probability calculated from a fit to external
1291 data [165]. This cascade continues until the pion is absorbed or exits the nucleus.

1292 Once the outgoing particle kinematics have been determined from NEUT, they
1293 are passed into the detector simulation. The near detectors ND280 and INGRID are
1294 simulated using a GEANT4 package [109, 166] to simulate the detector geometry and
1295 particle tracking. The response of the detectors is simulated using the elecSim pack-
1296 age. The far detector simulation is based upon the original Kamiokande experiment
1297 software which uses the GEANT3-based SKDETSIM [109, 167] package. This controls
1298 the interactions of particles in the water as well as Cherenkov light production. The
1299 water quality and PMT calibration measurements detailed in subsection 1.4.2 are also
1300 used within this simulation to make accurate predictions of the detector response.

₁₃₀₁ **3.2 Event Reconstruction at SK**

₁₃₀₂ Any above Cherenkov threshold event which occurs in SK will be recorded by the
₁₃₀₃ PMT array, where each PMT records the time and accumulated charge is measured.
₁₃₀₄ This is shown in the event displays illustrated in Figure 3.3. To be useful for physics
₁₃₀₅ analyses, this series of PMT hit information needs to be reconstructed to determine the
₁₃₀₆ particle’s identity and kinematics. This is because the charge and timing distribution
₁₃₀₇ of photons generated by a particular particle in an event is dependent upon its initial
₁₃₀₈ vertex position, time, direction, and momentum of the particle.

₁₃₀₉ For the purposes of this analysis, the `fitQun` reconstruction algorithm is utilised.
₁₃₁₀ Its core function is to compare a prediction of the accumulated charge and timing
₁₃₁₁ distribution from each PMT, generated for a particular particle hypothesis, to that
₁₃₁₂ observed in the neutrino event. It determines the best particle hypothesis by min-
₁₃₁₃ imising a likelihood function which includes information from PMTs which were hit
₁₃₁₄ and those that were not hit. This improves upon the `APFit` reconstruction algorithm
₁₃₁₅ which has been used for many previous SK analyses. `APFit` only includes information
₁₃₁₆ from PMTs within the 43 deg Cherenkov cone and then sequentially fits the kinematic
₁₃₁₇ parameters and particle configuration. Conversely, `fitQun` performs a simultaneous
₁₃₁₈ fit, improving both the accuracy of the fit parameters and the rejection of neutral
₁₃₁₉ current π^0 events [168, 169]. The `fitQun` algorithm is based on the key concepts
₁₃₂₀ on the MiniBooNE reconstruction algorithm [170] and is described in [171] which is
₁₃₂₁ summarised below.

₁₃₂₂ An event in SK can consist of multiple “sub-events”. For example, a muon neutrino
₁₃₂₃ interaction will generate a muon which will subsequently decay into an electron.
₁₃₂₄ Both the muon and electron can generate Cherenkov photons but both subevents
₁₃₂₅ need to be reconstructed separately. Therefore, to avoid assigning photons generated

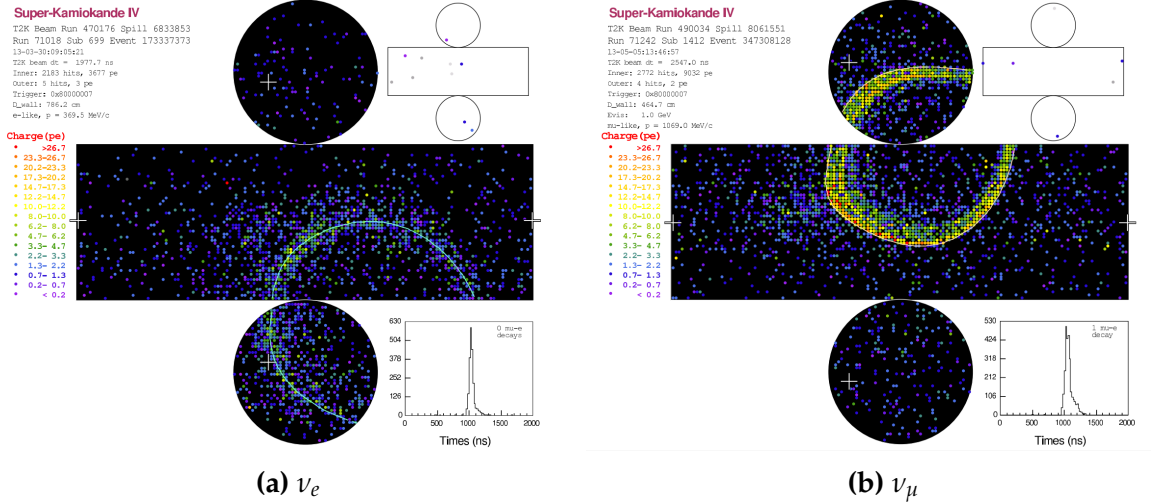


Figure 3.3: Event displays from Super Kamiokande illustrating the “crisp” ring from a muon and the typically “fuzzy” electron ring. Each pixel represents a PMT and the color scheme denotes the accumulated charge deposited on that PMT. Figures taken from [172].

1326 by the decay-electron to the muon, each event is divided into time clusters, termed
 1327 “subevents”, where subevent is defined to contain at most one hit for each PMT. To
 1328 find the subevents, a vertex goodness metric is calculated for some vertex position \vec{x}
 1329 and time t ,

$$G(\vec{x}, t) = \sum_i^{\text{hit PMTs}} \exp \left(-\frac{1}{2} \left(\frac{T_{Res}^i(\vec{x}, t)}{\sigma} \right)^2 \right) \quad (3.1)$$

1330 where

$$T_{Res}^i(\vec{x}, t) = t_i - t - |R_{PMT}^i - \vec{x}| / c_n \quad (3.2)$$

1331 is the residual hit time, R_{PMT}^i is the position of the i^{th} PMT, c_n is the speed of light in
 1332 water and $\sigma = 4\text{ns}$ which is comparable to the time resolution of the PMT. When the fit

1333 values of time and vertex are close to the true values, $T_{Res}^i(\vec{x}, t)$ tends to zero resulting
 1334 in subevents appearing as spikes in the goodness metric. The fit vertex and time are
 1335 grid-scanned, and the values which maximise the goodness metric are selected as the
 1336 “pre-fit vertex”. Whilst this predicts a vertex for use in the clustering algorithm, the
 1337 final vertex is fit using the higher-precision maximum likelihood method described
 1338 below.

1339 Once the pre-fit vertex has been determined, the goodness metric is scanned as a
 1340 function of t to determine the number of delayed peaks. A peak-finding algorithm
 1341 is then used on the goodness metric, requiring the goodness metric to exceed some
 1342 threshold and drop below a reduced threshold before any delayed additional peaks
 1343 are considered. The thresholds are set such that the rate of false peak finding is
 1344 minimised while still attaining good data to Monte Carlo agreement. To improve
 1345 performance, the pre-fit vertex for each delayed subevent is re-calculated after PMT
 1346 hits from the primary subevent are masked. This improves the decay-electron tagging
 1347 performance. Once all subevents have been determined, the time window around
 1348 each subevent is then defined by the earliest and latest time which satisfies $-180 <$
 1349 $T_{Res}^i < 800\text{ns}$. The subevents and associated time windows are then used as seeds for
 1350 further reconstruction.

1351 For a given subevent, `fiTQun` constructs a likelihood based on the accumulated
 1352 charge q_i and time information t_i from the i^{th} PMT,

$$L(\Gamma, \vec{\theta}) = \prod_j^{\text{unhit}} P_j(\text{unhit}|\Gamma, \vec{\theta}) \prod_i^{\text{hit}} \{1 - P_i(\text{unhit}|\Gamma, \vec{\theta})\} f_q(q_i|\Gamma, \vec{\theta}) f_t(t_i|\Gamma, \vec{\theta}), \quad (3.3)$$

1353 where $\vec{\theta}$ defines the track parameters; vertex position, direction vector and mo-
 1354 menta, and Γ represents the particle hypothesis. $P_i(\text{unhit}|\Gamma, \vec{\theta})$ defines the probability

₁₃₅₅ of the i^{th} tube to not register a hit given the track parameters and particle hypothesis.
₁₃₅₆ The charge likelihood, $f_q(q_i|\Gamma, \vec{\theta})$, and time likelihood, $f_t(t_i|\Gamma, \vec{\theta})$, represent the probability density function of observing charge q_i and time t_i on the i^{th} PMT given track parameters $\vec{\theta}$ and particle hypothesis Γ .

₁₃₅₉ As the generation and propagation of the optical photons are independent of the
₁₃₆₀ PMT and electronics response, it is natural to split the calculation into two. Firstly,
₁₃₆₁ calculating the expected number of photoelectrons (or predicted charge), μ_i , at the
₁₃₆₂ i^{th} PMT, and then calculating the likelihood based on this value. This substitution
₁₃₆₃ allows the charge likelihood density $f_q(q_i|\mu_i)$ and unhit probability $P_i(\text{unhit}|\mu_i)$ to be
₁₃₆₄ expressed via quantities that are only dependent on the response of the PMT.

₁₃₆₅ The predicted charge is calculated based on contributions from both the direct
₁₃₆₆ light and the scattered light. The direct light contribution is determined based on the
₁₃₆₇ integration of the Cherenkov photon profile along the track. PMT angular acceptance
₁₃₆₈ and water quality and calibration measurements discussed in subsection 1.4.2 are
₁₃₆₉ included to accurately model the detector's response. The scattered light is calculated
₁₃₇₀ in a similar way although it includes a scattering function that depends on the vertex
₁₃₇₁ of the particle and the position of the PMT. The charge likelihood is calculated by
₁₃₇₂ comparing the prediction to the observed charge in the PMT, where the prediction
₁₃₇₃ assumes photoelectron generation obeys a Poisson distribution.

₁₃₇₄ The time likelihood is approximated to depend on the vertex \vec{x} , direction \vec{d} , and
₁₃₇₅ time t of the track parameters as well as the particle hypothesis. The expected time
₁₃₇₆ for PMT hits is calculated by assuming unscattered photons being emitted from the
₁₃₇₇ midpoint of the track, S_{mid} ,

$$t_i^{exp} = t + S_{mid}/c + |R_{PMT}^i - \vec{x} - S_{mid}\vec{d}|/c_n, \quad (3.4)$$

where c is the speed of light in a vacuum. The time likelihood is then expressed in terms of the residual difference between the PMT hit time and the expected hit time, $t_i^{Res} = t_i - t_i^{exp}$. As the first photon hit defines the PMT hit time, the time likelihood density profile is narrower for higher momenta particles which introduces a dependence on the predicted charge. The particle hypothesis and momentum also affect the Cherenkov photon distribution which modifies the shape of the time likelihood density since in reality not all photons are emitted at the midpoint of the track. As with the charge likelihood, the contributions from both the direct and scattered light to the time likelihood density are calculated separately, which are both calculated from particle gun studies.

The track parameters, $\vec{\theta}$, which maximise $L(\Gamma|\vec{\theta})$ are defined the best fit parameters. In practice MINUIT [173] is used to minimise the value of $-\ln L(\Gamma, \vec{\theta})$. The particle hypothesis is determined by the comparison of $L(\Gamma, \vec{\theta})$ across all viable hypotheses, Γ . The fit considers an electron-like, muon-like, and charged pion-like hypothesis. The particle's identity is determined by taking the ratio of the likelihood of each of the hypotheses. For instance, electrons and muons are distinguished by considering the value of $\ln(L_e/L_\mu)$ as illustrated in Figure 3.4.

Alongside the three hypotheses which have a single final state particle generating optical photons, denoted “single-ring” particle hypotheses, the `fitQun` algorithm also considers a π^0 hypothesis. To do this, it performs a fit looking for two standard electron-hypothesis tracks which point to the same vertex position and time. This assumes the electron tracks are generated from photon-conversion so the electron tracks actually appear offset from the proposed π^0 vertex. For these fits, the conversion length, direction, and momenta of each photon are also considered as track parameters which are then fit in the same methodology as the standard single-ring hypotheses.

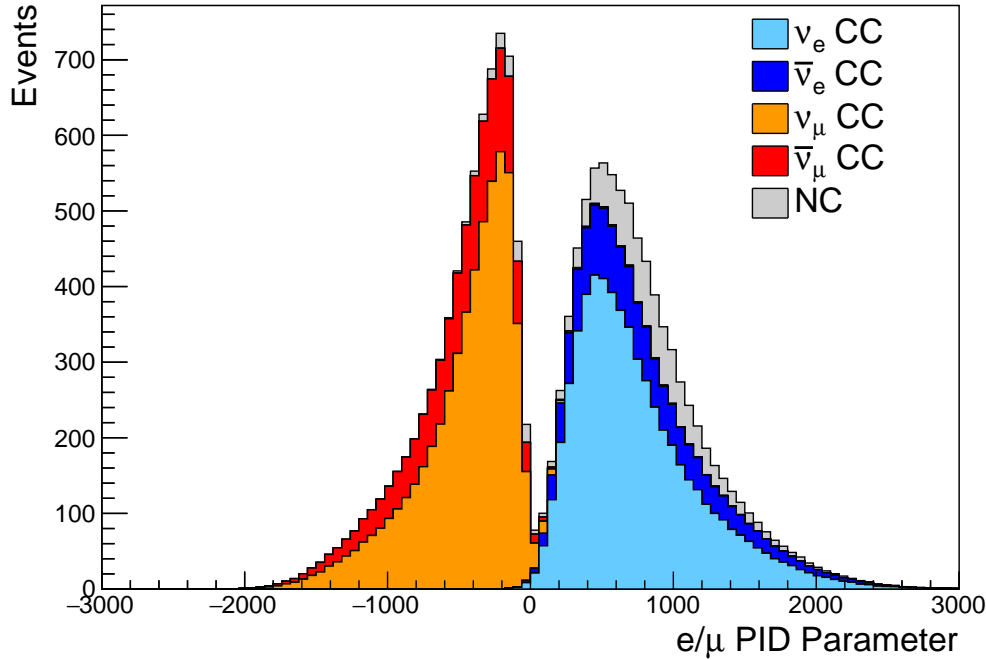


Figure 3.4: The electron/muon PID separation parameter for all sub-GeV single-ring events in SK-IV. The charged current (CC) component is broken down in four flavours of neutrino ($\nu_\mu, \bar{\nu}_\mu, \nu_e$ and $\bar{n}u_e$). Events with positive values of the parameter are determined to be electron-like.

The previous discussion pertains to a single final state particle that generates optical photons. However, the higher energy atmospheric neutrino events can generate final states with multiple particles which generate Cherenkov photons. These “multi-ring” hypotheses are also considered in the `fitQun` algorithm, but only for the first subevent in each ring to reduce computational cost. When calculating the charge likelihood density, the predicted charge associated with each ring is calculated separately and then merged to calculate the total accumulated charge on each PMT. Similarly, the time likelihood for the multi-ring hypothesis is calculated assuming each ring is independent. However, each track is then time-ordered based on the time of flight from the center of the track to the PMT, and the direct light from any ring incident on the PMT arrives before any scattered light. To reduce computational resources required for a fit, the multi-ring fits only consider electron-like and charged pion-like rings as the pion fit can be used as a proxy for a muon fit due to their similar mass.

1416 Typically, multi-ring fits have the largest likelihood because of the additional
1417 degrees of freedom introduced. Multi-ring fits proceed by proposing another ring
1418 to the previous fit and then fitting the parameters in the method described above.
1419 The additional ring is only added if the ratio of likelihoods between the n and $n + 1$
1420 passes the criteria. The criteria values for single-ring and multi-ring separation have
1421 been determined to be 9.35(11.83) based on Monte-Carlo studies, for hypotheses with
1422 electron-like(muon-like) the first ring.

1423 As an example of how the reconstruction depends on the detector conditions, the
1424 author of this thesis assessed the quality of event reconstruction for SK-V data. The
1425 detector systematics invoked within the T2K-only oscillation analysis are determined
1426 using data to Monte Carlo comparisons using the SK-IV data [174]. Due to tank-open
1427 maintenance occurring between SK-IV and SK-V, the dark rate of each PMT was
1428 observed to increase due to light exposure for a significant time during the repairs.
1429 This can be seen in Figure 3.5. Run-10 of the T2K experiment was conducted in the SK-
1430 V period, so the consistency of SK-IV and SK-V data needs to be studied to determine
1431 whether the SK-IV defined systematics can be applied to the run-10 data. This study
1432 was performed using the stopping muon data set for both the SK-IV and SK-V periods.
1433 This data is used due to the high rate of interactions, $O(200)$ events per hour, as well
1434 as having similar energies to muons from CCQE ν_μ interactions. The rate of cosmic
1435 muons does depend on the solar activity cycle [175]. This has been neglected in this
1436 comparison study as it is the shape of the distributions which is important for the
1437 purposes of being compared to the detector systematics. 2398.42 and 626.719 hours of
1438 SK-IV and SK-V are used which equates to 686743 and 192504 events respectively.

1439 The predicted charge used in the `fitQun` charge likelihood calculation for each
1440 PMT includes the photoelectron emission contribution from the dark rate of the PMT.
1441 Therefore, the increase in the dark rate needs to be accounted for. In practice, the

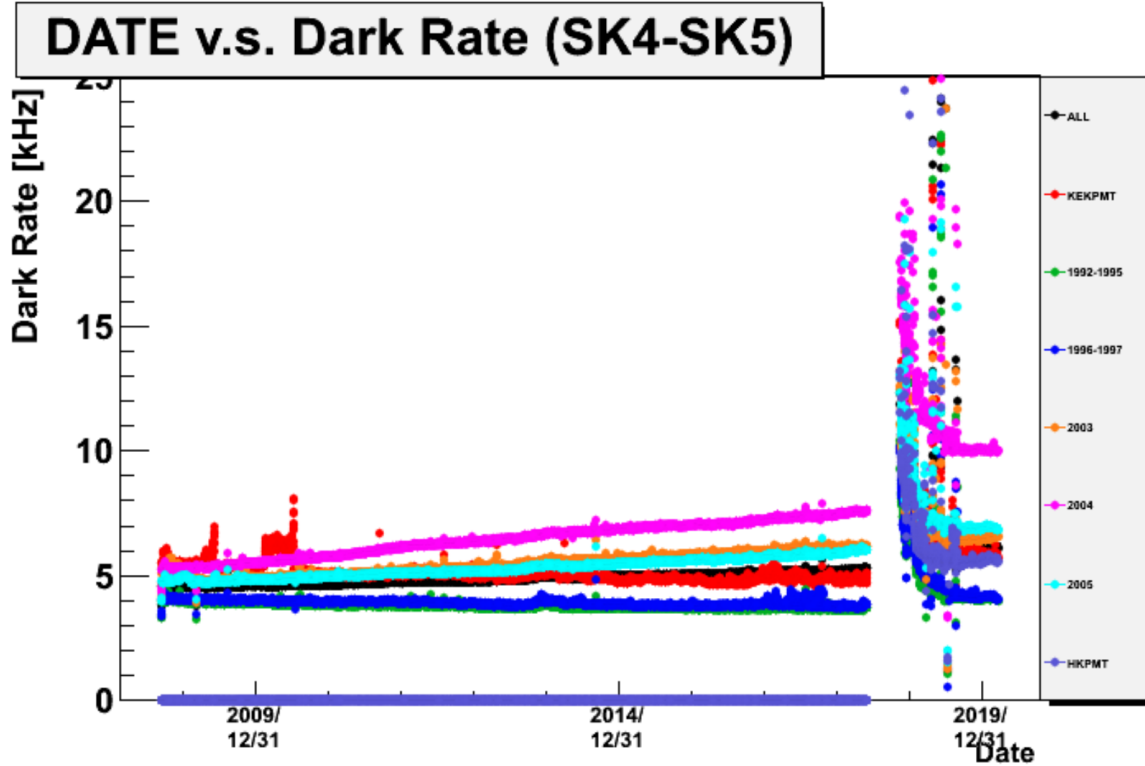


Figure 3.5: The variation of the measured dark rate as a function of date, broken down by PMT type. The SK-IV and SK-V periods span September 2008 to May 2018 and January 2019 to July 2020 respectively. The break in measurement between 2018 corresponds to the period of tank repair and refurbishment. Figure adapted from [174].

reconstruction algorithm takes the average dark rate for all PMTs for each SK period as an input and predicts the associated charge from this contribution. The dark rate was calculated by averaging the dark rate per run for each period separately, using the calibration measurements detailed in subsection 1.4.2. The average dark rate from SK-IV and SK-V were found to be 4.57kHz and 6.30kHz , respectively. The associated charge with the muon and decay electron subevents are illustrated in Figure 3.6. As expected, the increase in dark rate is not observed in the muon subevent which is of typically higher energy. However, it has a clear effect on the decay electron subevent which is lower energy.

The energy scale systematic for the SK-IV period was determined to be 2.1% [176]. It is defined to be equal to the difference between data and Monte Carlo prediction

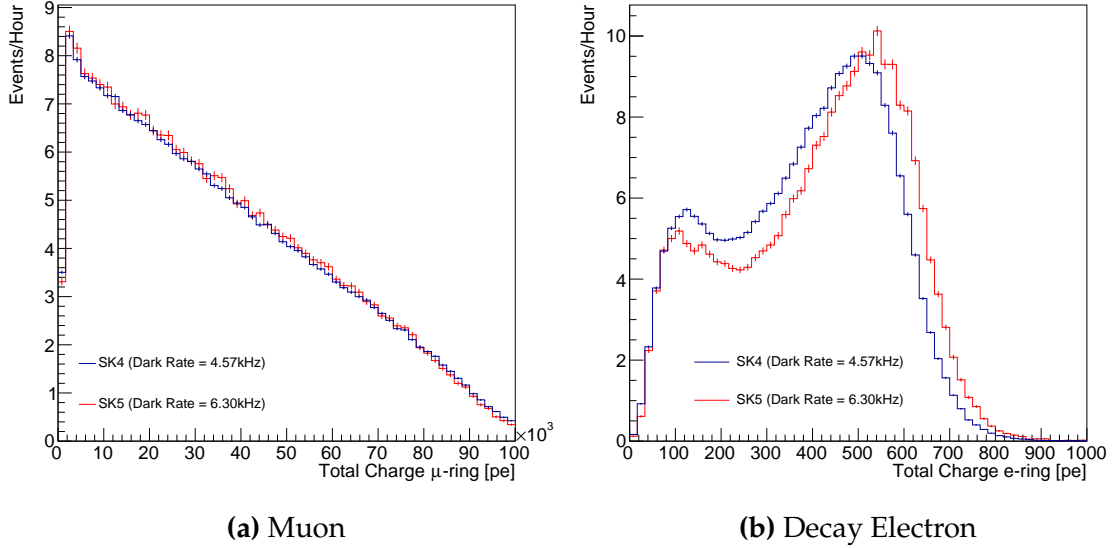


Figure 3.6: Comparison of the measured raw charge deposited per event from the stopping muon data samples between SK-IV (Blue) and SK-V (Red), split by the primary muon subevent and the associated decay electron subevent.

in the stopping muon data sample. To determine the consistency of the SK-IV and SK-V with respect to the energy scale systematic, the muon momentum distribution is compared between the two SK periods. The distribution of Cherenkov photons is dependent upon the momentum of the particle. This is then integrated along the track length of the particle to determine the PMT hit probability for each PMT. Consequently, the reconstructed momentum divided by track length is compared between SK-IV and SK-V as illustrated in Figure 3.7.

The consistency between these distributions has been computed in two ways. Firstly, a Gaussian is fit to each distribution separately. The mean of which is found to be $(2.272 \pm 0.003)\text{MeV/cm}$ and $(2.267 \pm 0.006)\text{MeV/cm}$ for SK-IV and SK-V respectively. The ratio of these is equal to 1.002 ± 0.003 . The mean of the Gaussian's is consistent with the expected stopping power of a minimum ionising muon for a target material (water) with $Z/A \sim 0.5$ [177]. The second consistency check is performed by introducing a nuisance parameter, α , which modifies the SK-V distribution. The value of α which minimises the χ^2 between the SK-IV and SK-V is determined by

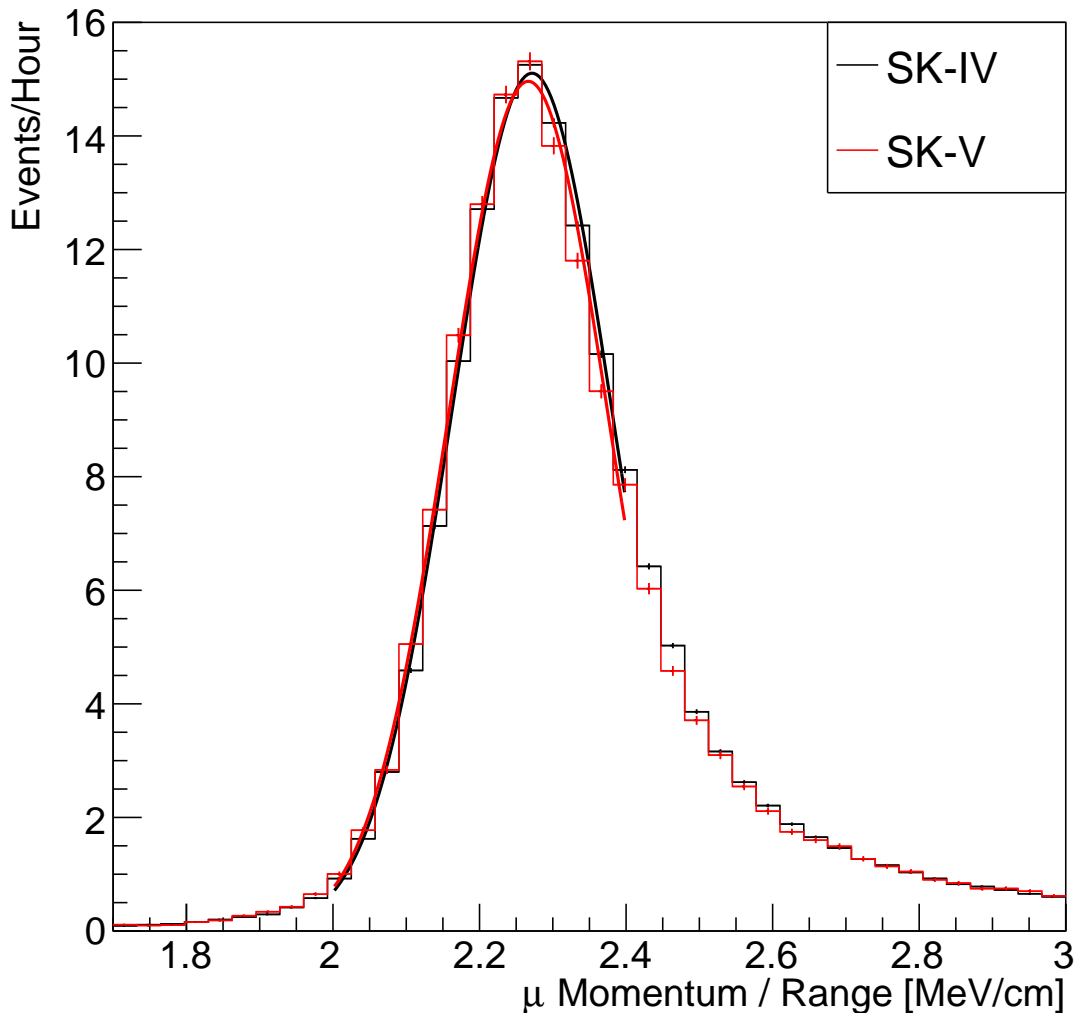


Figure 3.7: The distribution of the reconstructed momentum from the muon ring divided by the distance between the reconstructed muon and decay electron vertices as found in the stopping muon data sets of SK-IV (Black) and SK-IV (Red). Only events with one tagged decay electron and considered. A Gaussian fit is considered in the range [2.0, 2.4] MeV/cm and illustrated as the solid curve.

scanning across a range of values. This is repeated by applying α as a multiplicative factor and an additive shift. The χ^2 distributions for different values of α is illustrated in Figure 3.8. The values which minimise the χ^2 are found to be 0.0052 and 1.0024 for the additive and multiplicative implementations respectively. No evidence of shifts larger than the 2.1% uncertainty on the energy scale systematic has been found in the reconstructed momentum distribution of SK-IV and SK-V.

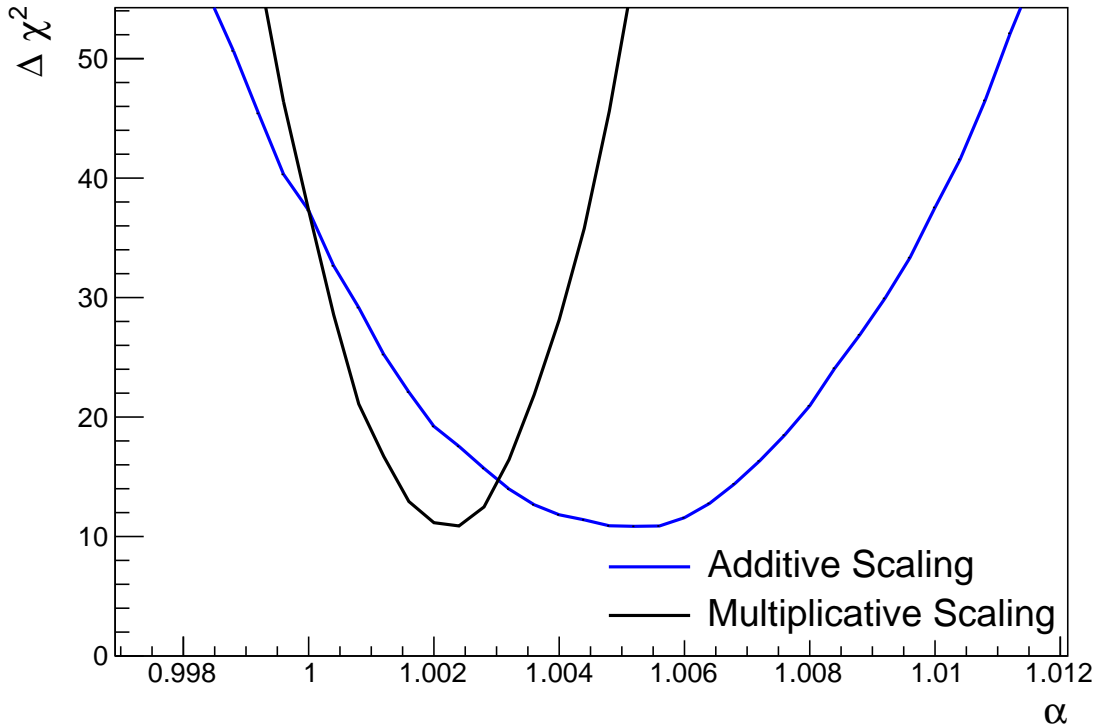


Figure 3.8: The χ^2 difference between the SK-IV and SK-V reconstructed muon momentum divided by range when the SK-V is modified by the scaling parameter α . Both additive (Blue) and multiplicative (Black) scaling factors have been considered. In practice, the additive scaling factor actually uses the value of $(\alpha - 1.0)$.

¹⁴⁷⁴ 3.3 Event Selection at SK

¹⁴⁷⁵ Atmospheric neutrino events observed in the SK detector are categorised into three
¹⁴⁷⁶ different types of samples; fully contained (FC), partially contained (PC) and up-
¹⁴⁷⁷ going muon (Up- μ), using signatures in the inner and outer detector (ID and OD,
¹⁴⁷⁸ respectively). To identify FC neutrino events, it is required that the neutrino interacts
¹⁴⁷⁹ inside the fiducial volume of the ID such that no significant OD activity is observed.
¹⁴⁸⁰ For this analysis, an event is defined to be in the fiducial volume providing the
¹⁴⁸¹ event vertex is at least 0.5m away from the ID walls. PC events have the same ID
¹⁴⁸² requirements but can have a larger signal present inside the OD. Typically these events
¹⁴⁸³ are higher energy muon interactions that penetrate the ID walls. The Up- μ sample

¹⁴⁸⁴ contains events where muons are created in the OD water or rock below the tank
¹⁴⁸⁵ and then propagate upwards through the detector. The reason downward-going
¹⁴⁸⁶ muons generated from neutrino interactions above the tank are neglected is due to
¹⁴⁸⁷ the difficulty in separating their signature from the cosmic muon shower background.
¹⁴⁸⁸ The sample categories are visually depicted in Figure 3.9.

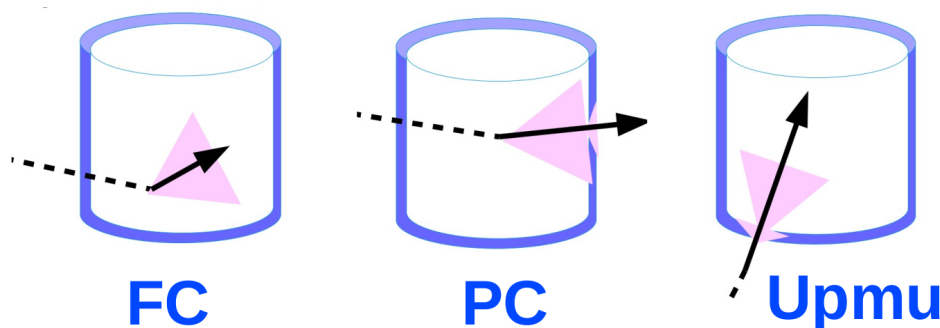


Figure 3.9: A depiction of the topology patterns for fully-contained (FC), partially-contained (PC) and up-going muon ($\text{Up-}\mu$) samples included in this analysis.

¹⁴⁸⁹ Based on the event characteristics as defined by the `fitQun` event reconstruction
¹⁴⁹⁰ software, the FC events are further divided up by

- ¹⁴⁹¹ • **Visible Energy:** equal to the sum of the reconstructed kinetic energy above the
¹⁴⁹² Cerenkov threshold for all rings present in the event. The purpose is to separate
¹⁴⁹³ events into sub-GeV and multi-GeV categories.
- ¹⁴⁹⁴ • **Number of observed Cerenkov rings.** The purpose is to separate single-ring and
¹⁴⁹⁵ multi-ring events, where single-ring events predominantly consist of quasi-elastic
¹⁴⁹⁶ interactions and multi-ring events are resonant pion production or deep inelastic
¹⁴⁹⁷ scattering events.
- ¹⁴⁹⁸ • **Particle identification parameter of the most energetic ring:** A value deter-
¹⁴⁹⁹ mined from the maximum likelihood value based on `fitQun`'s electron, muon, or
¹⁵⁰⁰ pion hypothesis. The purpose is to separate electron-like and muon-like events.

- **Number of sub-events:** Based on optimised time cuts, this quantity determines the number of observed decay electrons associated with an event. The main purpose is to separate quasi-elastic events (which have one decay electron emitted from the muon decay) and resonant pion production events (which have two decay electrons emitted from the muon and pion).

The PC and Up- μ categories are broken down into “through-going” and “stopping” samples depending on whether the muon left the detector. This is because the stopping events deposited the entire energy of the interaction into the detector, resulting in better reconstruction. Through-going Up- μ samples are further broken down by whether any hadronic showering was observed in the event which would be mostly likely due to DIS interactions. The expected neutrino energy for the different categories is given in Figure 3.10. FC sub-GeV and multi-GeV events peak around 0.7GeV and 3GeV respectively, with slightly different peak energies for $\nu_x \rightarrow \nu_e$ and $\nu_x \rightarrow \nu_\mu$. PC and Up- μ are almost entirely comprised of $\nu_x \rightarrow \nu_\mu$ events and peak around 7GeV and 100GeV respectively.

In data-taking operation, the SK detector observes many background events alongside the beam and atmospheric neutrino signal events of physics interest. Cosmic ray muons and flasher events, which is the spontaneous discharge of a given PMTm contribute the largest amount of background events in the energy range relevant to oscillation analyses. Lower energy analyses like DSNB searches are also subject to radioactive backgrounds [178]. Therefore the data recorded is reduced with the aim of removing these background events. The reduction process is detailed in [46, 83] and briefly summarised below.

The first two steps in the FC reconstruction remove most cosmic ray muons by requiring a significant amount of ID activity compared to that measured in the OD. This is done by counting the total number of photoelectrons recorded in the ID as

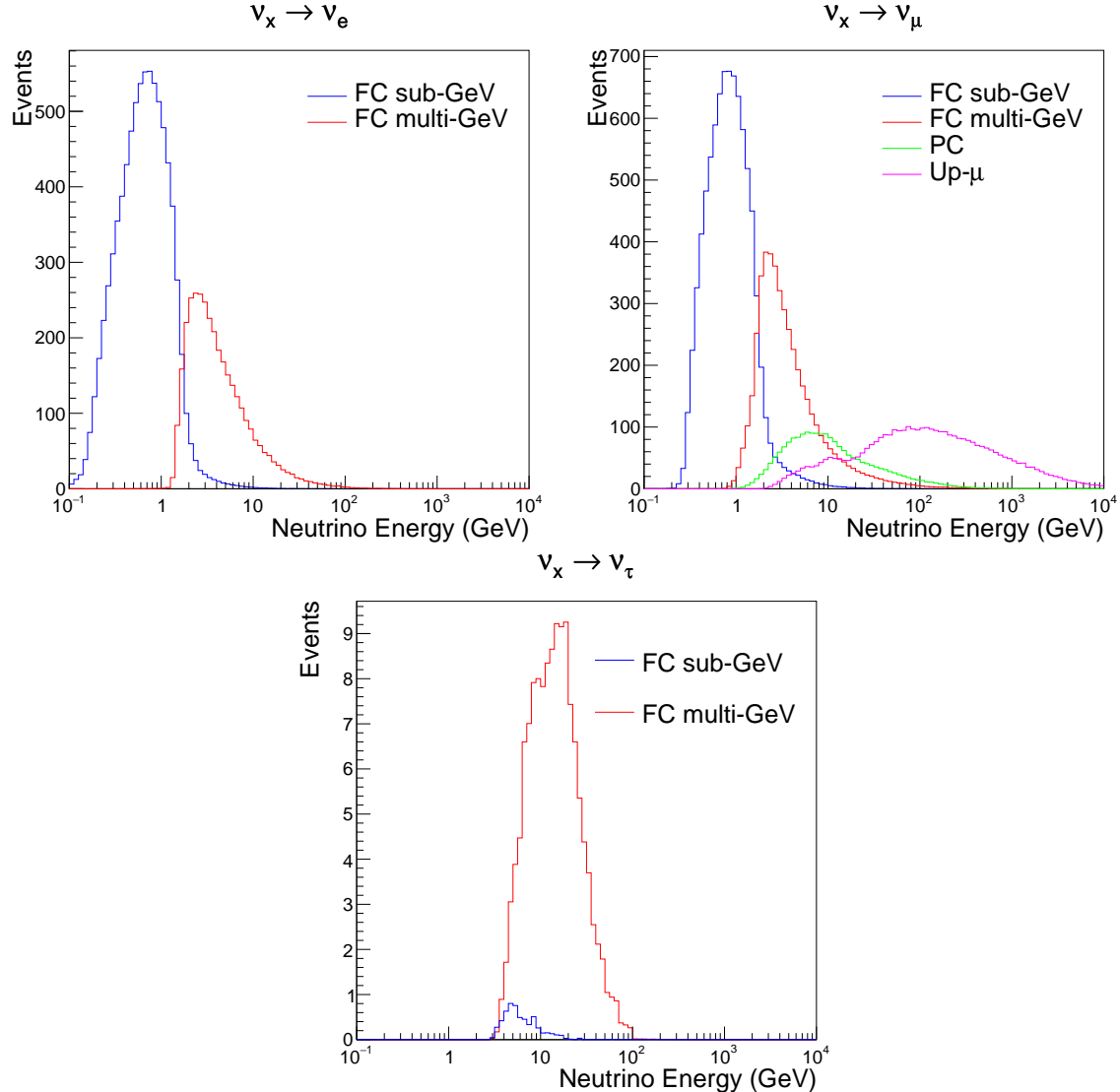


Figure 3.10: The predicted neutrino flux of the fully contained (FC) sub-GeV and multi-GeV, partially contained (PC) and upward-going muon (Up- μ) events. The prediction is broken down by the $\nu_x \rightarrow \nu_e$ prediction (top left), $\nu_x \rightarrow \nu_\mu$ prediction (top right) and $\nu_x \rightarrow \nu_\tau$ prediction (bottom). All systematic dials are set to their nominal values and the Asimov A oscillation parameters are assumed.

well as the number of hits in the OD. A third reduction step is then applied to select cosmic-ray muons that pass the initial reduction. These are typically high momentum muons or events which leave only a small number of hits in the OD. A purpose-built cosmic muon fitter is used to determine the entrance (or exit) position of the muon from the OD and a cut is applied to OD activity contained within 8m of this position. Flasher events are removed in the fourth reduction step which is based on the close

proximity of PMT hits surrounding the PMT producing the flash. Events that pass the reduction stage to this point are reconstructed using the more accurate APFit algorithm and the fifth step of the reduction uses the information from this more accurate fitter to repeat the third and fourth reduction steps using tighter cuts. This particularly targets invisible muons which are below the Cherenkov threshold resulting in no OD activity but whose decay electrons generate light inside the ID. The final cuts require the event vertex to be within the fiducial volume (0.5m from the wall although the nominal distance is 2.0m), visible energy $E_{vis} > 30\text{MeV}$ and fewer than 16 hits within the higher energy OD cluster. The culmination of the fully contained reduction results in 8.09 events/day in the nominal fiducial volume [179]. The uncertainty in the reconstruction is calculated by comparing Monte Carlo prediction to data. The largest discrepancy is found to be 1.3% in the fourth reduction step.

The PC and Up- μ events are also processed through their own reduction processes detailed in [46]. Both of these samples are reconstructed with the APFit algorithm rather than `fiTQun`. This is because the efficiency of reconstructing events that leave the detector has not been sufficiently studied for reliable systematic uncertainties. 0.66 and 1.44 events/day are found after the final step of reduction for the PC and Up- μ samples respectively.

₁₅₅₁ **Chapter 4**

₁₅₅₂ **Oscillation Probability Calculation**

₁₅₅₃ The calculation of the oscillation probability is crucial to the reliability of the sensitivity
₁₅₅₄ measurements of the analysis presented within this thesis. Firstly, it is important to
₁₅₅₅ understand how and where the sensitivity to the oscillation parameters comes from
₁₅₅₆ for both atmospheric and beam samples. An overview of how these sets of samples
₁₅₅₇ observe changes in δ_{CP} , Δm_{23}^2 , and $\sin^2(\theta_{23})$ as well as how the atmospheric samples
₁₅₅₈ have an increased sensitivity to mass hierarchy determination is given in section 4.1.
₁₅₅₉ It also explains the additional complexities involved when including atmospheric
₁₅₆₀ neutrinos as compared to a beam-only analysis.

₁₅₆₁ Without additional techniques, atmospheric sub-GeV upward-going neutrinos can
₁₅₆₂ artificially inflate the sensitivity to δ_{CP} due to the quickly varying oscillation probabil-
₁₅₆₃ ity in this region. Therefore, a “sub-sampling” approach has been developed to reduce
₁₅₆₄ these biases ensuring accurate and reliable sensitivity measurements. This technique
₁₅₆₅ ensures that small-scale unresolvable features of the oscillation probability have been
₁₅₆₆ averaged over whilst the large-scale resolvable features in the oscillation probability
₁₅₆₇ have been kept. The documentation of this technique is found in section 4.2 alongside
₁₅₆₈ the validation of the choices which have been made. The CUDAProb3 implementation
₁₅₆₉ choice made within the fitting framework, as detailed in section 4.3, ensures that the
₁₅₇₀ analysis can be done in a timely manner.

₁₅₇₁ Whilst the beam neutrinos are assumed to propagate through a constant density
₁₅₇₂ slab of material, the density variations through the Earth result in more complex
₁₅₇₃ oscillation patterns Furthermore, the uncertainty in the electron density can modify

1574 the oscillation probability for the denser core layers of the Earth. section 4.4 details
1575 the model of the Earth used within this analysis. This includes the official SK-only
1576 methodology as well as relatively straightforward improvements that can be made to
1577 more closely approximate the PREM model. Another quirk of atmospheric neutrinos
1578 oscillation studies is that the height of production in the atmosphere is not known
1579 on an event-by-event analysis. An analytical averaging technique that approximates
1580 the uncertainty of the oscillation probability has been followed, with the author of
1581 this thesis being responsible for the implementation and validation. This technique is
1582 illustrated in section 4.5 alongside the variation in oscillation probability which would
1583 be an expected effect in the down-going and horizontal-going neutrinos.

1584 4.1 Overview

1585 The analysis presented within this thesis focuses on the determination of oscillation
1586 parameters from atmospheric and beam neutrinos. Whilst subject to the same oscil-
1587 lation probability, the way in which the two sets of samples have sensitivity to the
1588 different oscillation parameters differs quite significantly.

1589 Atmospheric neutrinos have a varying baseline, or “path length”, such that the
1590 distance each neutrino travels before interacting is dependent upon the zenith angle.
1591 Therefore the oscillation probability can be represented as a two-dimensional “oscillo-
1592 gram” as shown in Figure 4.1. For this calculation, four layers of fixed density were
1593 used to model the Earth with values taken from an approximation of the PREM model.
1594 These can be seen in the distinct discontinuities in the oscillogram as a function of the
1595 zenith angle.

1596 Another complexity of atmospheric neutrino oscillation probability calculation is
1597 the uncertainty in the height at which a neutrino was produced, termed the “produc-

tion height". Primary cosmic rays, which contribute most of the neutrino flux, can interact anywhere between the Earth's surface and ~ 50 km above that. The baseline, L , for a neutrino generated with zenith angle, θ , and production height, h , can be calculated as

$$L = \sqrt{(R_E + h)^2 - R_E^2 (1 - \cos^2(\theta))} - R_E \cos(\theta), \quad (4.1)$$

where $R_E = 6,371$ km is the Earth's radius.

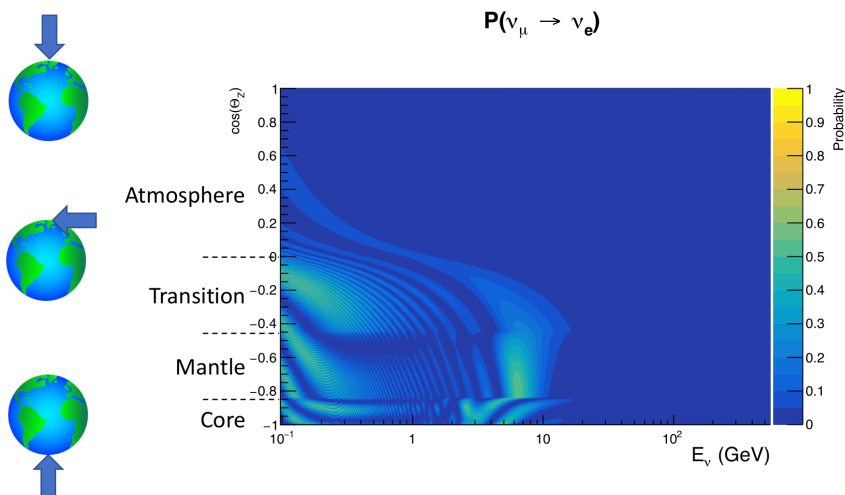


Figure 4.1: An "Oscillogram" that depicts the $P(\nu_\mu \rightarrow \nu_e)$ oscillation probability as a function of neutrino energy and cosine of the zenith angle. The zenith angle is defined such that $\cos(\theta_Z) = 1.0$ represents neutrinos that travel from directly above the detector. The four-layer constant density PREM model approximation is used and Asimov A oscillation parameters are assumed.

Atmospheric neutrinos do have some sensitivity to δ_{CP} through a normalisation term. Figure 4.2 illustrates the difference in oscillation probability between CP-conserving and CP-violating δ_{CP} values. The result is a complicated oscillation pattern in the appearance probability for sub-GeV upgoing neutrinos. The detector does not have sufficient resolution to resolve these individual patterns so the sensi-

tivity to δ_{CP} for atmospheric neutrinos comes via the overall normalisation of the
 sub-GeV upgoing events. The presence of matter means that the effect δ_{CP} has on
 the oscillation probability is not equal between neutrinos and antineutrinos which
 would be expected when propagating through a vacuum. This is further extenuated
 by the fact that SK can not distinguish neutrinos and antineutrinos well and that the
 cross-section neutrino interaction is larger than that for antineutrinos. Finally, sample
 selections (discussed in [DB: Link to selection chapter](#)) targeting different neutrino
 interaction modes (charge current quasi-elastic and single pion production) result in
 an imbalance in the percentage of neutrinos to anti-neutrinos in these samples due
 to pion capture. Negatively charged pions from antineutrino interactions are more
 likely to be captured by a nucleus compared to a positively charged pion emitted from
 a neutrino interaction. This all culminates in atmospheric neutrinos having a very
 complex sensitivity to δ_{CP} .

Atmospheric neutrinos are subject to matter effects as they travel through the dense
 matter in the Earth. The vacuum and matter oscillation probabilities for $P(\nu_e \rightarrow \nu_e)$
 and $P(\bar{\nu}_e \rightarrow \bar{\nu}_e)$ are presented in Figure 4.3. The oscillation probability for both neutrinos
 and antineutrinos are affected in the presence of matter but the resonance (Effects
 around $E_\nu \sim 5\text{GeV}$) only occurs for neutrinos in normal mass hierarchy and antineu-
 trinos for inverse mass ordering. The exact position and amplitude of the resonance
 depend on $\sin^2(\theta_{23})$ meaning that the atmospheric neutrinos have sensitivity to the
 octant of θ_{23} .

As the T2K beam flux is centered at the first oscillation maximum, the sensitivity
 to δ_{CP} is predominantly observed as a change in the event-rate of e-like samples in
 $\nu/\bar{\nu}$ modes. Figure 4.4 illustrates the $P(\nu_\mu \rightarrow \nu_e)$ oscillation probability for a range
 of δ_{CP} values. A circular modulation of the oscillation peak (in both magnitude and
 position) is observed when varying throughout the allowable values of δ_{CP} . The CP-

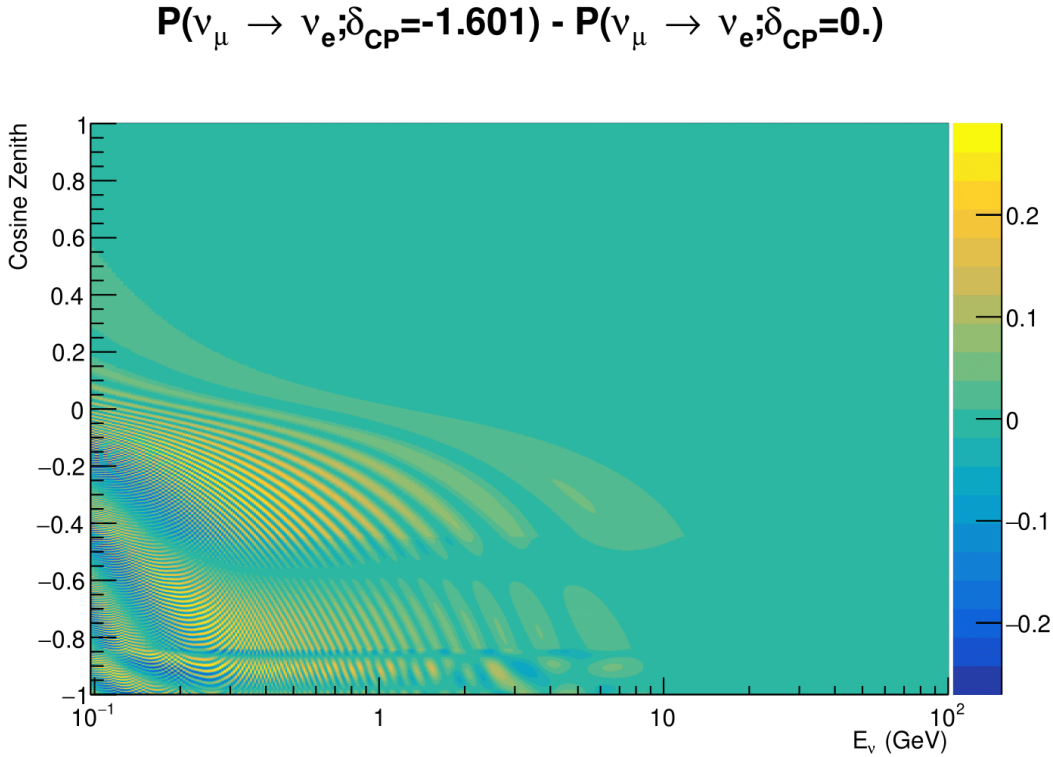


Figure 4.2: The effect of δ_{CP} for atmospheric neutrinos given in terms of the neutrino energy and zenith angle. The oscillogram compares the $P(\nu_\mu \rightarrow \nu_e)$ oscillation probability for a CP conserving ($\delta_{CP} = 0.0$) and CP violating ($\delta_{CP} = -1.601$) value of δ_{CP} . The other oscillation parameters assume the “Asimov A” oscillation parameter set given in Table 4.1.

1634 conserving values of $\delta_{CP} = 0, \pi$ have a lower(higher) oscillation maximum than the
 1635 CP-violating values of $\delta_{CP} = -\pi/2 (\delta_{CP} = \pi/2)$ leading to a $\sin(\delta_{CP})$ type sensitivity.
 1636 A sub-dominant shift in the energy of the oscillation peak is also present to aid in
 1637 separating the two CP-conserving values of δ_{CP} .

1638 T2K’s sensitivity to the atmospheric oscillation parameters is more of a shape-
 1639 based variation of the muon-like samples, as illustrated in Figure 4.4. The value of
 1640 Δm_{32}^2 laterally shifts the position of the oscillation dip (around $E_\nu \sim 0.6$ GeV) in the
 1641 $P(\nu_\mu \rightarrow \nu_\mu)$ oscillation probability. A variation of $\sin^2(\theta_{23})$ is predominantly observed
 1642 as a vertical shift of the oscillation dip with second-order horizontal shifts being due
 1643 to matter effects. The beam neutrinos have limited sensitivity to matter effects due

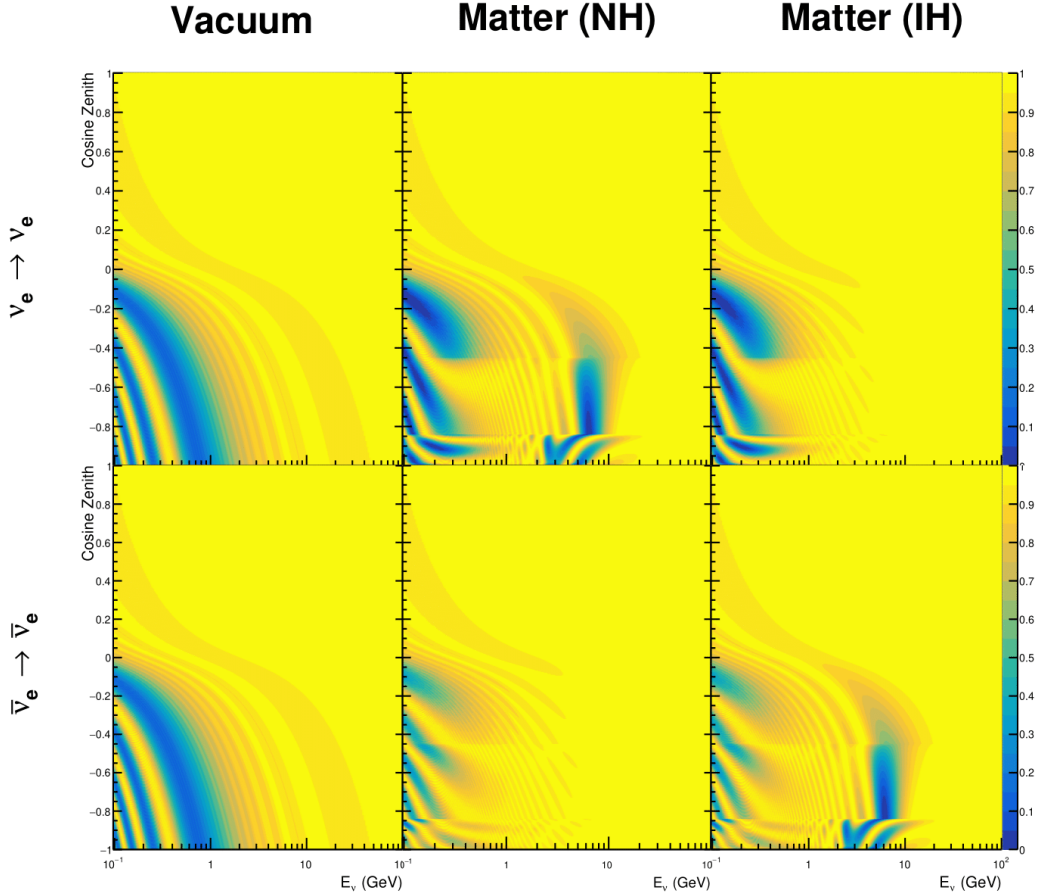


Figure 4.3: An illustration of the matter-induced effects on the oscillation probability, given as a function of neutrino energy and zenith angle. The top row of panels gives the $P(\nu_e \rightarrow \nu_e)$ oscillation probability and the bottom row illustrates the $P(\bar{\nu}_e \rightarrow \bar{\nu}_e)$ oscillation probability. The left column highlights the oscillation probability in a vacuum, whereas the middle and right column represents the oscillation probabilities when the four layer fixed density PREM model is assumed. All oscillation probabilities assume the “Asimov A” set given in Table 4.1, but importantly, the right column sets an inverted mass hierarchy. The “matter resonance” effects at $E_\nu \sim 5\text{GeV}$ can be seen in the $P(\nu_e \rightarrow \nu_e)$ for normal mass hierarchy and $P(\bar{\nu}_e \rightarrow \bar{\nu}_e)$ for inverted hierarchy.

to the shorter baseline as well as the Earth’s mantle is relatively low-density material
 (as compared to the Earth’s core). For some values of δ_{CP} , the degeneracy in the number of e-like events allows the mass hierarchy to be resolved. This leads to a δ_{CP} -dependent mass hierarchy sensitivity which can be seen in Figure 4.5.

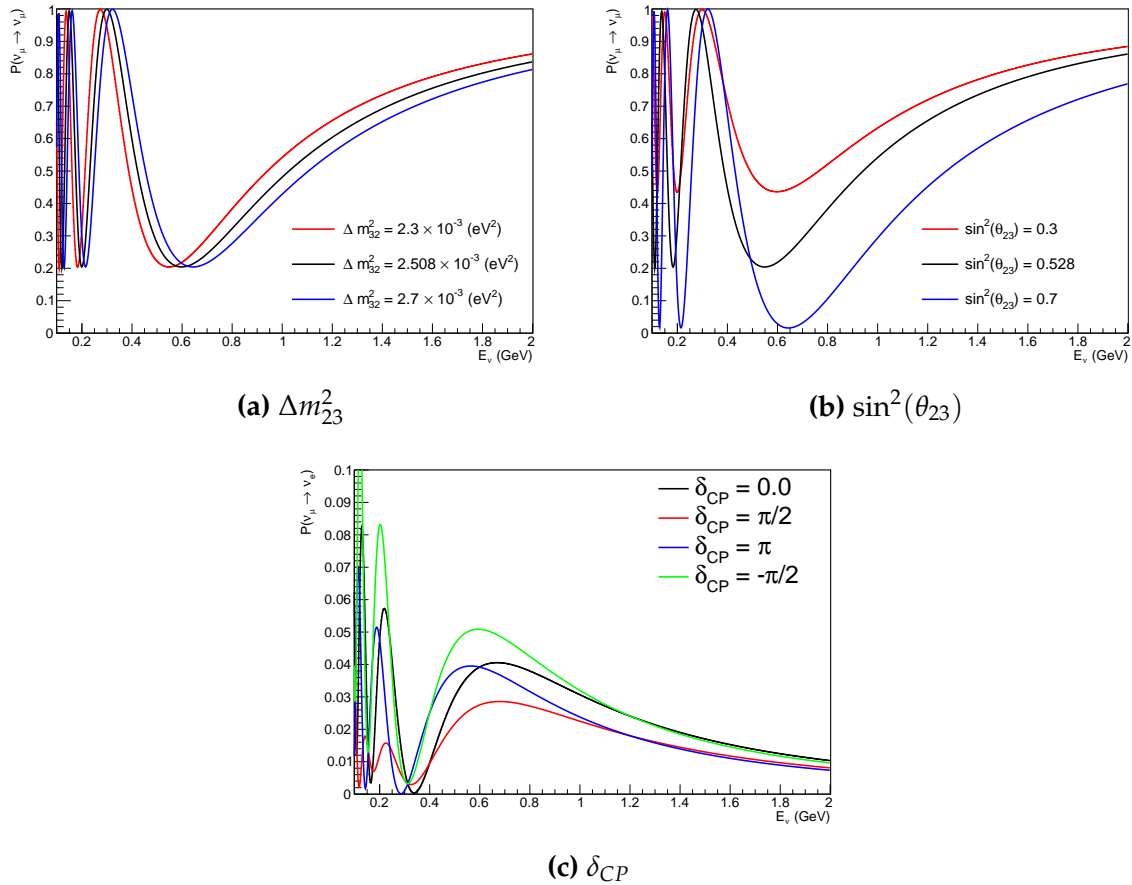


Figure 4.4: The oscillation probability for beam neutrino events given as a function of neutrino energy. All oscillation parameters assume the “Asimov A” set given in Table 4.1 unless otherwise stated. Each panel represents a change in one of the oscillation parameters whilst keeping the remaining parameters fixed.

Whilst all oscillation channels should be included for completeness, the computational resources required to run a fit are limited and any reasonable approximations which reduce the number of oscillation probability calculations that need to be made should be applied. The $\nu_e \rightarrow \nu_{e,\mu,\tau}$ (and antineutrino equivalent) oscillations can be ignored for beam neutrinos as the $\nu_e/\bar{\nu}_e$ fluxes being approximately two orders of magnitude smaller than the corresponding $\nu_\mu/\bar{\nu}_\mu$ flux. Furthermore, as the peak neutrino energy of the beam is well below the threshold for τ production ($E_\nu \sim 3\text{GeV}$ [180]) only a small proportion of the neutrinos produced in the beam have the required energy. For the few neutrinos that have sufficient energy, the oscillation probability is very small due to the short baseline. Whilst these approximations can be made for the

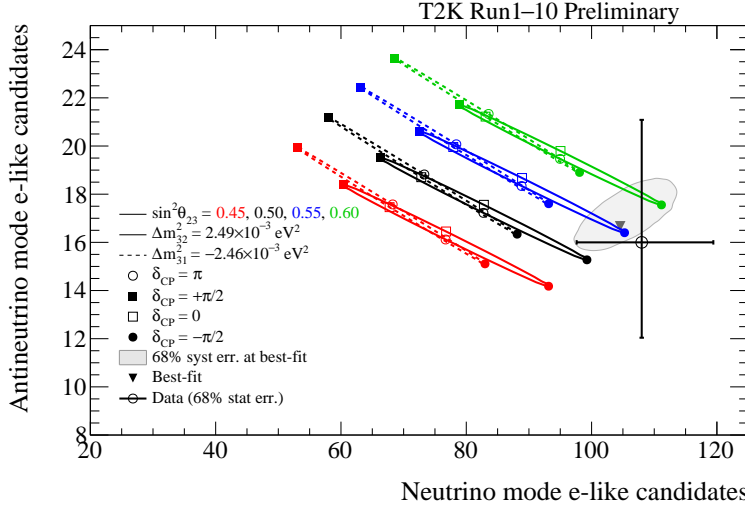


Figure 4.5: The number of electron-like events in the FHC and RHC operating mode of the beam, as a function of the oscillation probabilities. Both normal hierarchy (Solid) and inverse hierarchy (Dashed) values of Δm_{23}^2 are given.

beam neutrinos, the atmospheric flux of ν_e is of the same order of magnitude as the ν_μ flux and the energy distribution of atmospheric neutrinos extends well above the tau production threshold.

Throughout this thesis, several spectra predictions, Asimov fits, and contour comparisons are presented which require oscillation parameters to be assumed. Table 4.1 defines two sets of oscillation parameters, with “Asimov A” set being close to the preferred values from a previous T2K-only fit [181] and “Asimov B” being CP-conserving and further from maximal θ_{23} mixing.

| Parameter | Asimov A | Asimov B |
|-----------------------|-------------------------------------|----------|
| Δm_{12}^2 | $7.53 \times 10^{-5} \text{ eV}^2$ | |
| Δm_{32}^2 | $2.509 \times 10^{-3} \text{ eV}^2$ | |
| $\sin^2(\theta_{12})$ | 0.304 | |
| $\sin^2(\theta_{13})$ | 0.0219 | |
| $\sin^2(\theta_{23})$ | 0.528 | 0.45 |
| δ_{CP} | -1.601 | 0.0 |

Table 4.1: Reference values of the neutrino oscillation parameters for two different oscillation parameter sets.

1666 4.2 Treatment of Fast Oscillations

1667 As shown in Figure 4.6, atmospheric neutrino oscillations have a significantly more
1668 complex structure for upgoing neutrinos with energy below 1GeV. This is because the
1669 L/E dependence of the oscillation probability in this region induces rapid variations
1670 for small changes in L or E . As discussed in section 4.1, this is also the region in which
1671 atmospheric neutrinos have sensitivity to δ_{CP} . In practice, the direction between
1672 the detector and a neutrino's production vertex is inferred from the direction of any
1673 secondary particles created in the detector target. For low-energy neutrinos, this
1674 inference can be rather poor and introduces a distinct difference to beam neutrinos
1675 where the direction to production vertex is very well known.

1676 As a consequence of the poor detector resolution, an average oscillation probability
1677 is observed in this region. This creates a computational problem as a significantly
1678 large amount of MC statistics would be required to accurately predict the number
1679 of events in each bin if MC averaging was the only technique used. This section
1680 describes the ‘sub-sampling’ approach developed for this analysis and compares it to
1681 the methodology used within the SK-only analysis.

1682 The official SK-only analysis uses the osc3++ oscillation parameter fitter [182]. To
1683 perform the fast oscillation averaging, it uses a ‘nearest-neighbour’ technique. For a
1684 given neutrino MC event, the nearest neighbours in reconstructed lepton momentum
1685 and zenith angle are found and a distribution of neutrino energies is built. This
1686 distribution is then used to compute an average oscillation probability for the given
1687 neutrino MC event.

1688 For the i^{th} event, the oscillation weight is calculated as

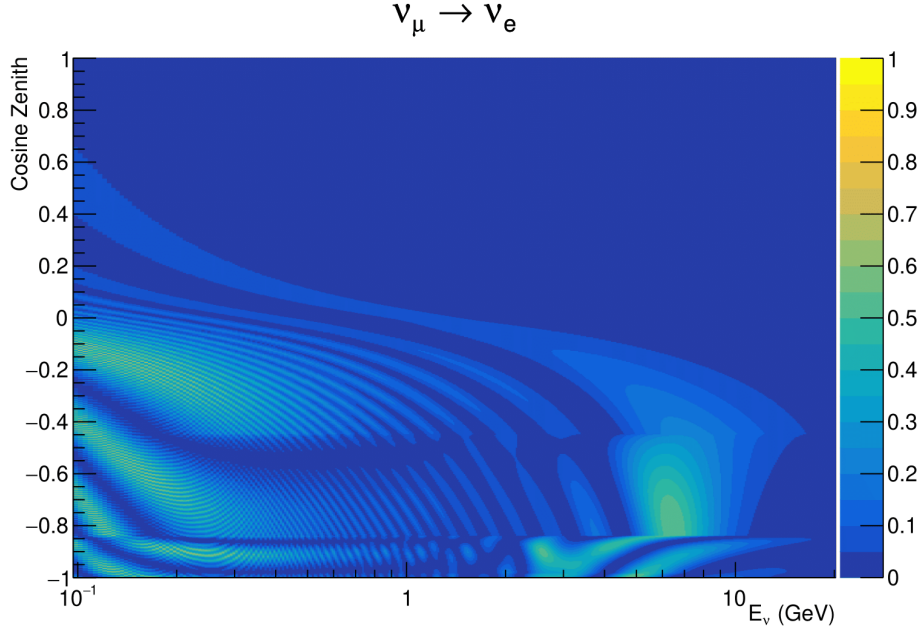


Figure 4.6: The oscillation probability $P(\nu_\mu \rightarrow \nu_e)$, given as a function of neutrino energy and zenith angle, which highlights an example of the “fast” oscillations in the sub-GeV upgoing region.

$$W_i = \frac{1}{5}P(E_i, \bar{L}_i) + \frac{1}{5} \sum_{\beta=-1, -0.5, 0.5, 1} P(E_i + \beta\sigma_i, L_\beta), \quad (4.2)$$

where $P(E, L)$ is the oscillation probability calculation for neutrino energy E and path length L , σ_i is the RMS of the energy distribution for the given event, and the two path lengths, \bar{L}_i and L_β are discussed below. In practice, twenty of the nearest neighbours are used to generate the neutrino energy distribution. All of the oscillation probability calculations are performed with a fixed zenith angle (and therefore have same matter density profile).

The uncertainty in the production height is controlled by using an “average” production height. \bar{L}_i represents the average path length computed using twenty production heights taken from the Honda flux model’s prediction [44] for a fixed zenith angle, where the production heights are sampled in steps of 5% of their cumulative

1699 distribution function. L_β values are similarly calculated but instead use different
1700 combinations of four production heights (sampled in the same way),

$$\begin{aligned} L_{-1.0} &= \frac{1}{4}L(45, 50, 55, 60), \\ L_{-0.5} &= \frac{1}{4}L(35, 40, 65, 70), \\ L_{+0.5} &= \frac{1}{4}L(25, 30, 75, 68), \\ L_{+1.0} &= \frac{1}{4}L(15, 20, 85, 89). \end{aligned} \tag{4.3}$$

1701 This averaging works well because of the correlation between the true neutrino
1702 zenith angle and the inferred direction from secondary particles in the detector. For
1703 low-energy neutrinos, where the resolution of the true neutrino direction is poor, σ_i
1704 will be large, resulting in significant averaging effects. Contrary to this, the inferred
1705 direction of high-energy neutrinos will be much closer to the true value, meaning that
1706 σ_i will be smaller.

1707 In practice, this technique is performed before the fit in order to deal with the
1708 computational cost. Oscillation probabilities are pre-calculated on a 4D grid. This
1709 is possible as the Osc3++ framework uses binned oscillation parameters rather than
1710 continuous so the oscillation parameters used in the fit are known prior to run-time.
1711 The framework used in the analysis presented within this thesis uses continuous
1712 oscillation parameters. Due to the MCMC technique invoked within the fitter (see
1713 chapter 2), there is no way to know which oscillation parameter values will be selected
1714 in each step at run-time. Therefore, the oscillation parameter calculation would have
1715 to be performed at run-time which is very expensive for event-by-event reweighting.
1716 Having to compute five oscillation probabilities per event would require far too many

¹⁷¹⁷ computational resources to be viable so the SK technique can not be used within this
¹⁷¹⁸ analysis. However, the concept of the averaging technique can be taken from it.

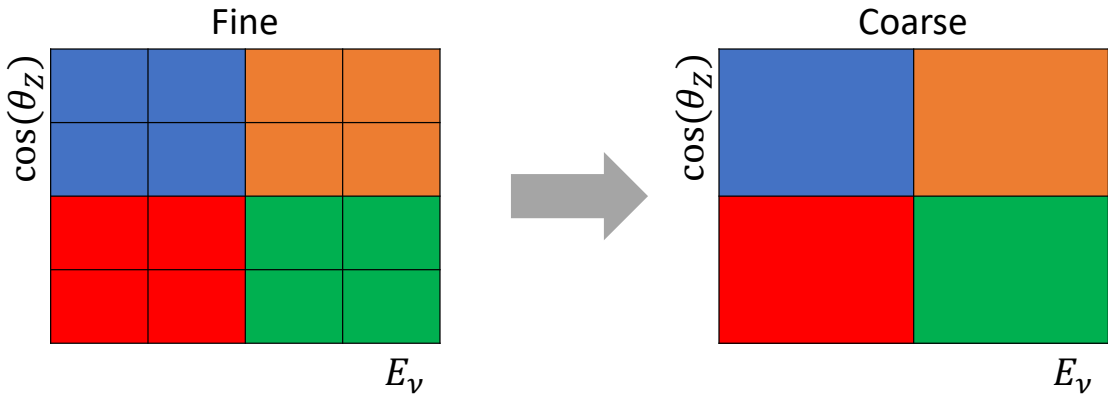


Figure 4.7: Illustration of the averaging procedure for $N = 2$. The oscillation probabilities calculated on the finer left binning are averaged to obtain the oscillation probabilities in the coarser right binning. These averaged oscillation probabilities with the coarser binning are then applied to each event during the fit.

¹⁷¹⁹ This analysis uses a binned oscillogram in which oscillation probabilities for a given
¹⁷²⁰ event are selected based on that event's attributes. To perform a similar averaging as
¹⁷²¹ the SK analysis, a sub-sampling approach has been devised. The technique can be
¹⁷²² explained by considering a "fine" and "coarse" oscillogram. The fine oscillograms
¹⁷²³ are used to define the array of cosine zeniths and energies for the neutrino oscillation
¹⁷²⁴ engine. The coarse oscillograms cover the same phase-space as the fine oscillograms
¹⁷²⁵ but have fewer bins in that range. Then, for a given coarse oscillogram bin, the value
¹⁷²⁶ of that bin will be taken as the average of all the oscillation probabilities of all the fine
¹⁷²⁷ oscillogram bins which fall into that coarse oscillogram bin.

¹⁷²⁸ The binning which is used to calculate the oscillation probabilities, known as the
¹⁷²⁹ 'fine' binning, has $N \times N$ subdivisions per coarse bin. The value assigned to a coarse
¹⁷³⁰ bin is the linear average (flat prior in E_ν and $\cos(\theta_Z)$) of all the oscillation probabilities
¹⁷³¹ calculated at the center of each fine bin contained within that coarse bin. Figure 4.7
¹⁷³² illustrates the $N = 2$ example where the assigned value to a coarse bin is the linear

1733 average of the four fine bins which fall in that coarse bin. Whilst the coarse bin edges
1734 are not linear on either axis, the sub-division of the fine bins is linear over the range
1735 of a coarse bin. The alignment of the fine and coarse binning edges is checked at
1736 run-time.

1737 The coarse binning is defined with 67×52 bins in true neutrino energy \times cosine
1738 zenith. In general, the binning is logarithmically spaced in neutrino energy but has
1739 some hand-picked bin edges. Firstly, the bin density around the matter resonance is
1740 smoothly increased around the matter resonance region. This is to avoid smearing
1741 this region which can be well sampled by the Monte Carlo. Secondly, bin edges
1742 are selected to hit $0.4, 0.6, 1, 10, 30, 50, 100\text{GeV}$. This is to ensure that the Coloumb
1743 correction systematic and the atmospheric flux systematics definitions in neutrino
1744 energy can be hit. The cosine zenith binning is approximately linearly spaced across
1745 the allowable range but the values of layer transitions are hit precisely; -0.8376
1746 (core-mantle) and -0.4464 (mantle/transition zone). Bins are spread further apart for
1747 downgoing events as this is a region unaffected by the fast oscillation wavelengths
1748 and reduces the total number of calculations required to perform the reweight (Not
1749 the number required to perform the oscillation calculation).

1750 The choice of N is justified based on two studies. Firstly, the variation of event
1751 rates of each sample is studied as a function of the number of subdivisions. For
1752 a given set of oscillation parameters thrown from the PDG prior constraints, the
1753 oscillation probabilities are calculated using a given value of N . Each sample is re-
1754 weighted and the event rate is stored. The value of N is scanned from 1, which
1755 corresponds to no averaging, to 24, which corresponds to the largest computationally
1756 viable subdivision binning. The event rate of each sample at large N is expected to
1757 converge to a stationary value due to the fine binning fully sampling the small-scale

1758 structure. Figure 4.8 illustrates this behaviour for the SubGeV_elike_0dcy sample for
 1759 30 different throws of the oscillation parameters.

SubGeV-elike-0dcy

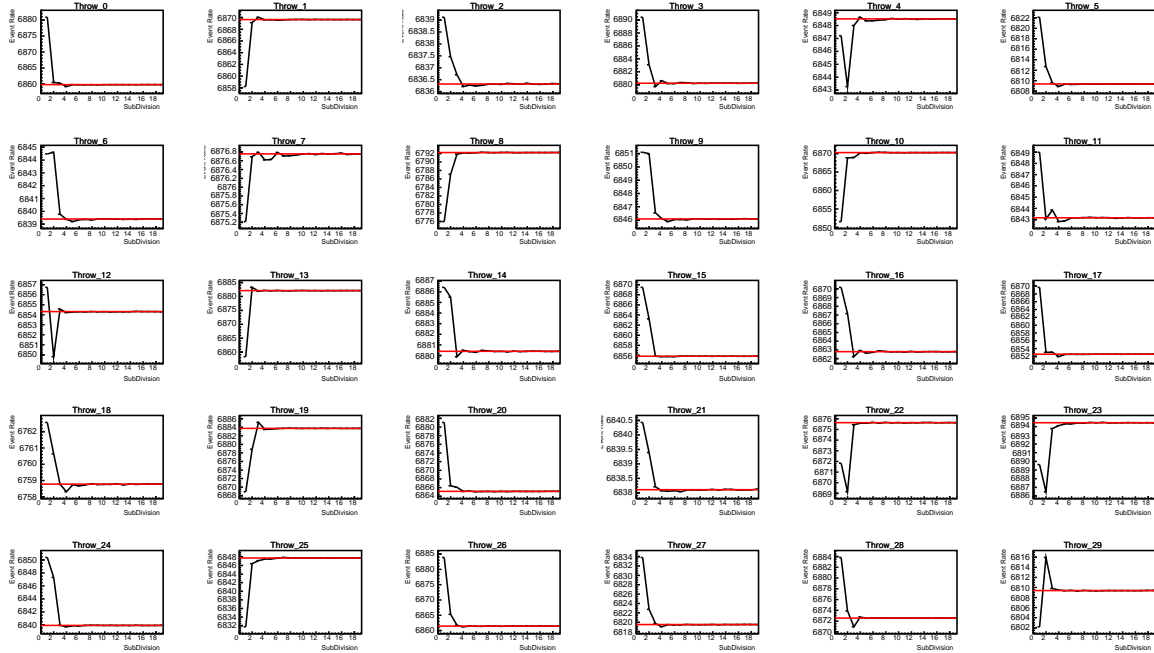


Figure 4.8: Event rate of the SubGeV_elike_0dcy sample as a function of the number of subdivisions per coarse bin. Each subplot represents the event rate of the sample at a different oscillation parameter set (thrown from the PDG priors). The red line in each subplot represents the mean of the event rate over the different values of sub-divisions for that particular oscillation parameter throw.

1760 Denoting the event rate for one sample for a given throw t at each N by $\lambda_t^{(N)}$, the
 1761 average over all considered N values ($\bar{\lambda}_t = \frac{1}{24} \sum_{N=1}^{24} \lambda_t^{(N)}$) is computed. The variance
 1762 in the event rate at each N is then calculated from

$$\text{Var}[\lambda^{(N)}] = \frac{1}{N_{\text{throws}}} \sum_{t=1}^{N_{\text{throws}}} \left(\lambda_t^{(N)} - \bar{\lambda}_t \right)^2 - \left[\frac{1}{N_{\text{throws}}} \sum_{t=1}^{N_{\text{throws}}} \left(\lambda_t^{(N)} - \bar{\lambda}_t \right) \right]^2. \quad (4.4)$$

The aim of the study is to find the lowest value of N such that this variance is below 0.001. This is the typical threshold used by T2K fitters to validate systematic implementation so is just as applicable to the oscillation probability calculation. The results of this study for each atmospheric sample used within this thesis are illustrated in Figure 4.9 for 2000 throws of the oscillation parameters. As can be seen, the variance is below the threshold at $N = 10$, and is driven primarily by the SubGeV_mulike_1dcy and SubGeV_elike_0dcy selections.

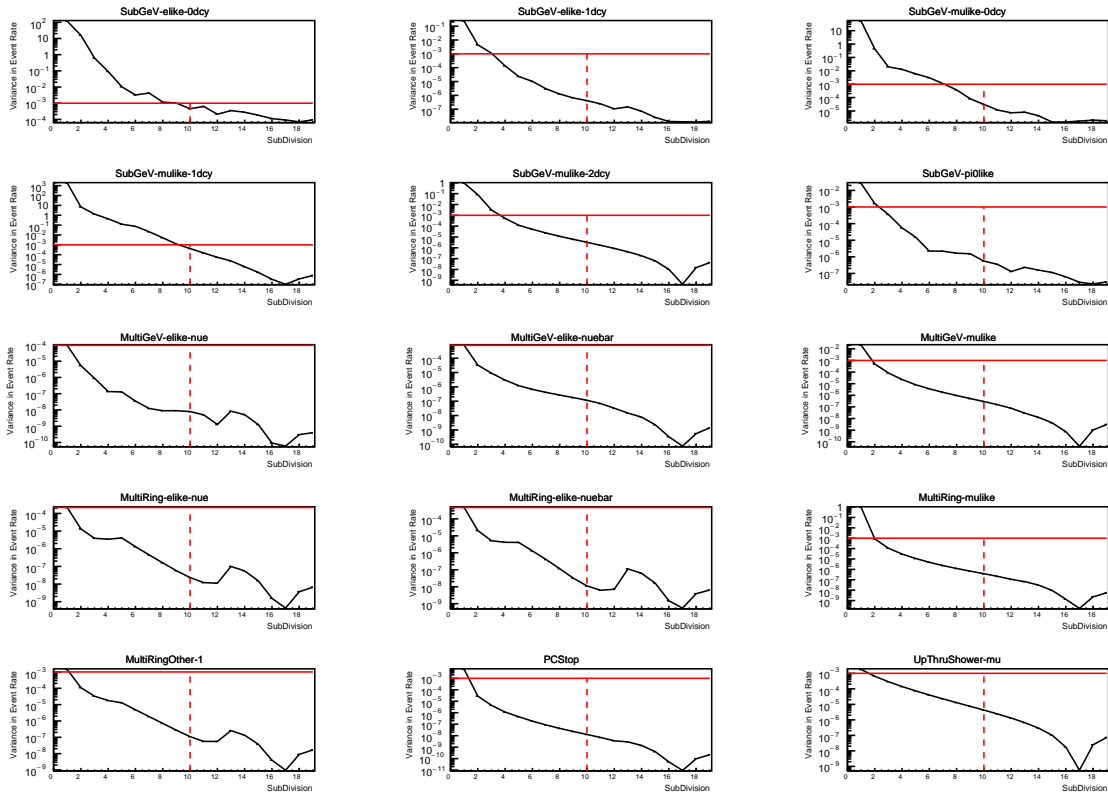


Figure 4.9: Variance of event rate for each atmospheric sample as a function of the number of sub-divisions per coarse bin. The solid red line indicates the 0.1% threshold and the dashed red line is a graphical indication of the variance at a sub-division $N = 10$.

The second study to determine the value of N is as follows. The likelihood for each sample is computed against an Asimov data set created with oscillation parameters from “Asimov A” in Table 4.1. Following Equation 4.4, the variance of the log-likelihood over all considered N is computed. The results are shown in Figure 4.10.

1774 This tests the impact of the averaging on each sample's binning by reconstructed
 1775 momentum and/or zenith angle and also provides a scale for the calculation errors
 1776 compared to their statistical uncertainties.

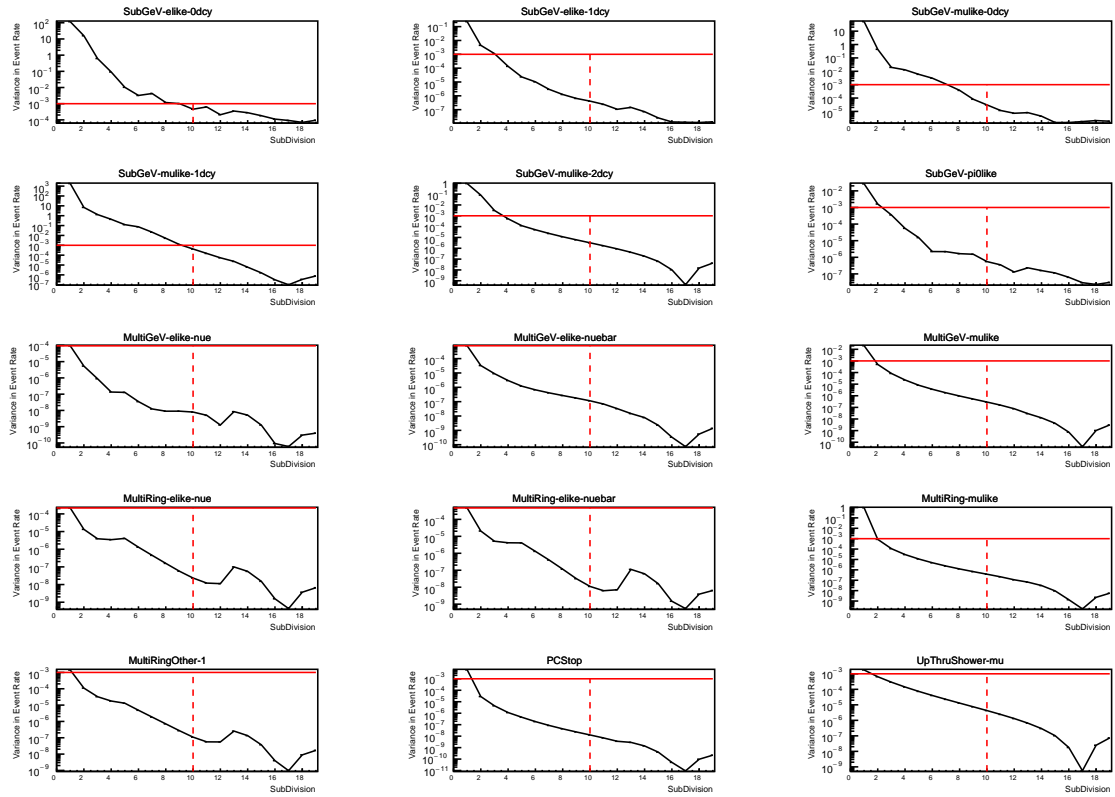


Figure 4.10: Variance of sample likelihood, when compared to 'Asimov data' set at Asimov A, for each atmospheric sample as a function of the number of sub-divisions per coarse bin. The solid red line indicates the 0.1% threshold and the dashed red line is a graphical indication of the variance at a sub-division $N = 10$.

1777 A choice of N sub-divisions per coarse bin has a variance in both event rate and
 1778 log-likelihood residuals less than the required threshold of 0.001. The event rate test is
 1779 the more stringent test. For the variance of log-likelihood residuals, the largest value is
 1780 of order 10^{-7} , corresponding to an error on the log-likelihood of about 3×10^{-4} , small
 1781 enough to be negligible for the oscillation analysis.

1782 In practice Figure 4.11 illustrates the effect of the smearing using $N = 10$. The fast
1783 oscillations in the sub-GeV upgoing region have been replaced with a normalisation
1784 effect whilst the large matter resonance structure remains.

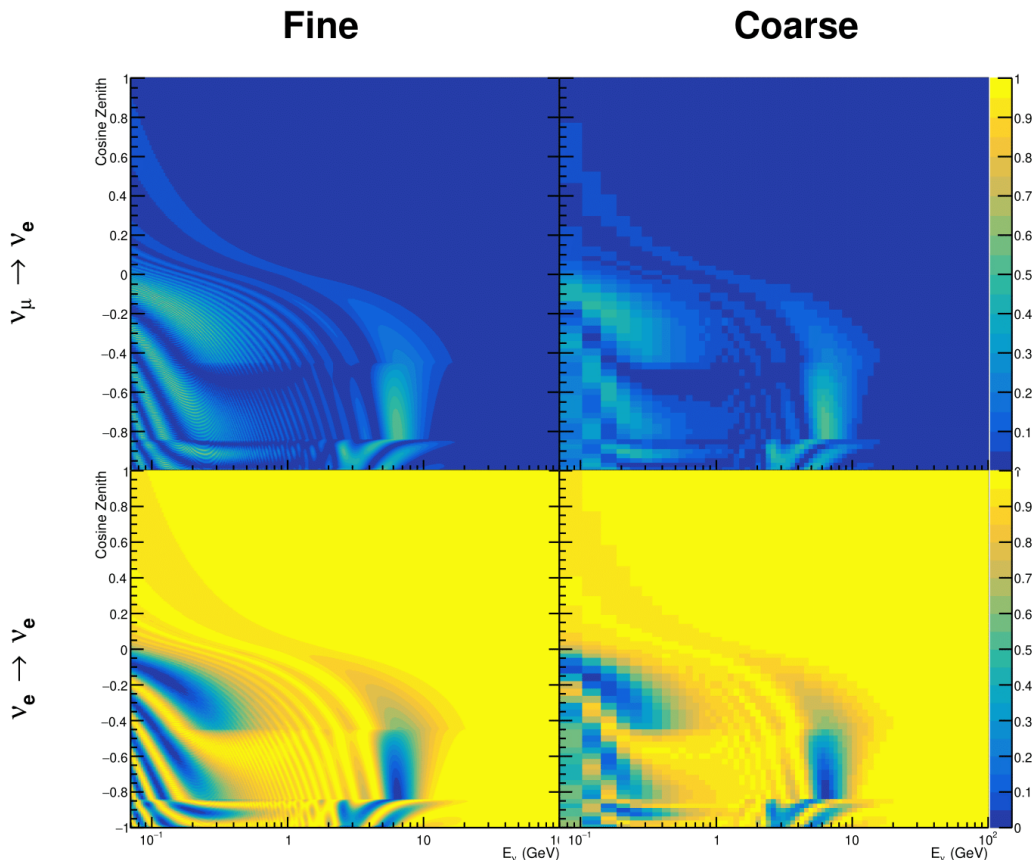


Figure 4.11: The oscillation probability, $P(\nu_\mu \rightarrow \nu_e)$ (top row) and $P(\nu_e \rightarrow \nu_e)$ (bottom row), given as a function of neutrino energy and zenith angle. The left column gives the “fine” binning used to calculate the oscillation probabilities and the right column illustrates the “coarse” binning used to reweight the MC events. The fine binning choice is given with $N = 10$, which was determined to be below threshold from Figure 4.9 and Figure 4.10.

1785 4.3 Calculation Engine

1786 As previously discussed in section 4.2, the calculation of oscillation probabilities is per-
1787 formed at run-time due to utilising continuous oscillation parameters. Consequently,
1788 the time per calculation is crucial for fit performance. The fitting framework used for
1789 this analysis was developed with ProbGPU [183]. This is a GPU-only implementation
1790 of the prob3 engine [184]. It is primarily designed for neutrino propagation in a beam
1791 experiment (single layer of constant density) with the atmospheric propagation code
1792 not being used prior to the analysis in this thesis.

1793 Another engine, CUDAProb3 [185], has been implemented within the fitting frame-
1794 work used within this analysis. It has been specifically optimised for atmospheric
1795 neutrino oscillation calculation so unfortunately does not contain the code to replace
1796 the beam oscillation calculation. Based on the benefits shown by the implementation
1797 in this chapter, efforts are being placed into including linear propagation for beam
1798 neutrino propagation into the engine [186]. The engine utilises object-orientated tech-
1799 niques as compared to the functional implementation of ProbGPU. This allows the
1800 energy and cosine zenith arrays to be kept on GPU memory, rather than having to
1801 load these arrays onto GPU memory for each calculation. General memory interfacing
1802 is one of the slowest tasks which GPUs can do, so being able to eliminate this signifi-
1803 cantly reduces the time required for calculation. This can be seen in Figure 4.12, where
1804 the GPU implementation of CUDAProb3 is approximately three times faster than the
1805 ProbGPU engine.

1806 Another significant advantage of CUDAProb3 is that it contains a CPU multithreaded
1807 implementation which is not possible with the ProbGPU or prob3 engines. This elimi-
1808 nates the requirement for GPU resources when submitting jobs to batch systems. As
1809 illustrated in Figure 4.12, the calculation speed depends on the number of available

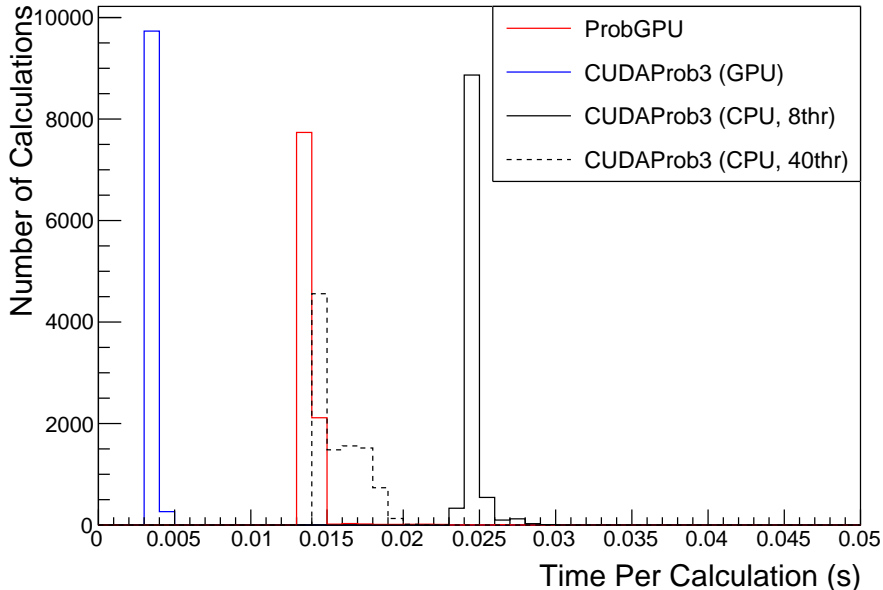


Figure 4.12: The calculation time taken to both calculate the oscillation probabilities and fill the “coarse” oscillograms, following the technique given in section 4.2, for the CUDAProb3 and ProbGPU (Red) calculation engines. CUDAProb3 has both a GPU (Blue) and CPU (Black) implementation, where the CPU implementation is multithreaded. Therefore, 8-threads (solid) and 40-threads (dashed) configurations have been used. Prob3, which is a CPU single-thread implementation has a mean step time of 1.142s.

1810 threads. Using 8 threads (which is typical of the batch systems being used) is ap-
 1811 proximately twice as slow as the ProbGPU engine implementation, but would allow
 1812 the fitting framework to be run on many more resources. This fact is utilised for any
 1813 SK-only fits but GPU resources are required for any fits which include beam samples
 1814 due to the ProbGPU requirement.

1815 4.4 Matter Density Profile

1816 For an experiment observing atmospheric neutrinos propagating through the Earth,
 1817 such as the studies presented in this thesis, a model of the Earth’s density and layering
 1818 is required. The model used within this analysis is the Preliminary Reference Earth
 1819 Model (PREM) [187]. This model provides piecewise cubic polynomials as a function

of radius which results in the density profile illustrated in Figure 4.13. As will be discussed in section 4.5, the propagator used within the calculation engine requires constant density layers. To follow the official SK-only analysis [182], the average density of each layer has been taken from the PREM model. Table 4.2 documents the density and radii of the layers used within this approximation.

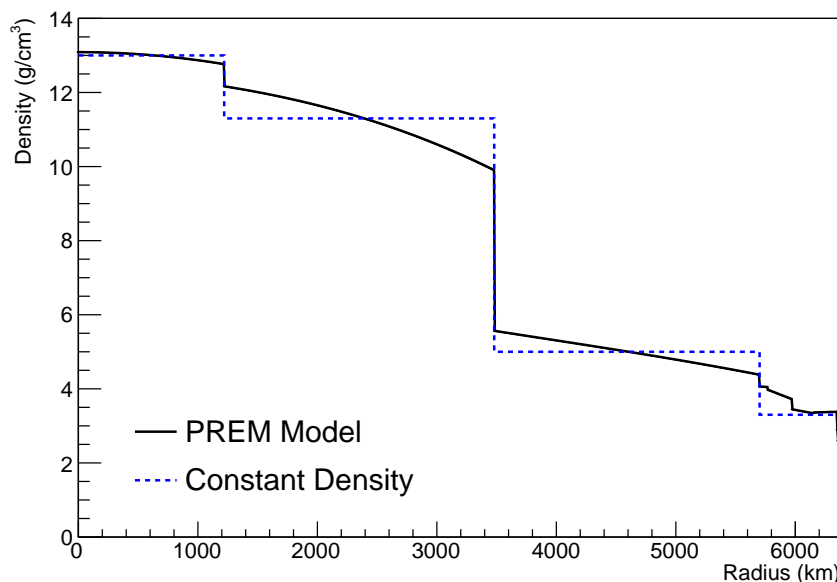


Figure 4.13: The density of the Earth given as a function of the radius, as given by the PREM model (Black) and the constant density four-layer approximation (Blue), as used in the official SK-only analysis.

| Layer | Outer Radius [km] | Density [g/cm ³] | Chemical composition (Z/A) |
|-----------------|-------------------|------------------------------|----------------------------|
| Inner Core | 1220 | 13 | 0.468 ± 0.029 |
| Outer Core | 3480 | 11.3 | 0.468 ± 0.029 |
| Lower Mantle | 5701 | 5.0 | 0.496 |
| Transition Zone | 6371 | 3.3 | 0.496 |

Table 4.2: Description of the four layers of the Earth invoked within the average constant density approximation of the PREM model [187].

The density measurements provided in the PREM model are provided in terms of mass density, whereas neutrino oscillations are sensitive to the electron number density. This value can be computed as the product of the chemical composition, or

the Z/A value, and the mass density of each layer. Currently, the only way to calculate this value for layers close to the Earth's core is through neutrino oscillations. The chemical composition of the upper layers of the Earth's Mantle and the Transition zone is well known due to it being predominantly pyrolite which has a chemical composition value of 0.496 [188]. The components of the Earth's core region are less well known. Consequently, the chemical composition dial for the core layers is set to a value of 0.468 [189]. This value is assigned a Gaussian error with a standard deviation equivalent to the difference in chemical composition in core and mantle layers. Figure 4.14 illustrates the effect of moving from the $Z/A = 0.5$ method which is used in the official SK-only analysis [182] to more precise values recorded by other neutrino experiments.

The beam oscillation probability in this thesis uses a baseline of 295km, density 2.6g/cm^3 [190], and chemical composition 0.5 as is done by the official T2K-only analysis.

Whilst the propagator requires a fixed density layer model of the Earth, the density only has to be fixed for a specific neutrino energy $\times \cos(\theta_Z)$ bin in a given layer (I.e. set of values at which to calculate the oscillation probability). As the density is a function of radius, which is a function of the direction in which a neutrino propagates, a better approximation of the PREM model can be made if a $\cos(\theta_Z)$ -specific density is calculated.

To achieve this, the average density, $\langle \rho \rangle_i$, in the i^{th} layer, is calculated as the density, ρ , integrated over the track a given $\cos(\theta_Z)$,

$$\langle \rho \rangle_i = \frac{1}{t_{i+1} - t_i} \int_{t_i}^{t_{i+1}} \rho(t) dt \quad (4.5)$$

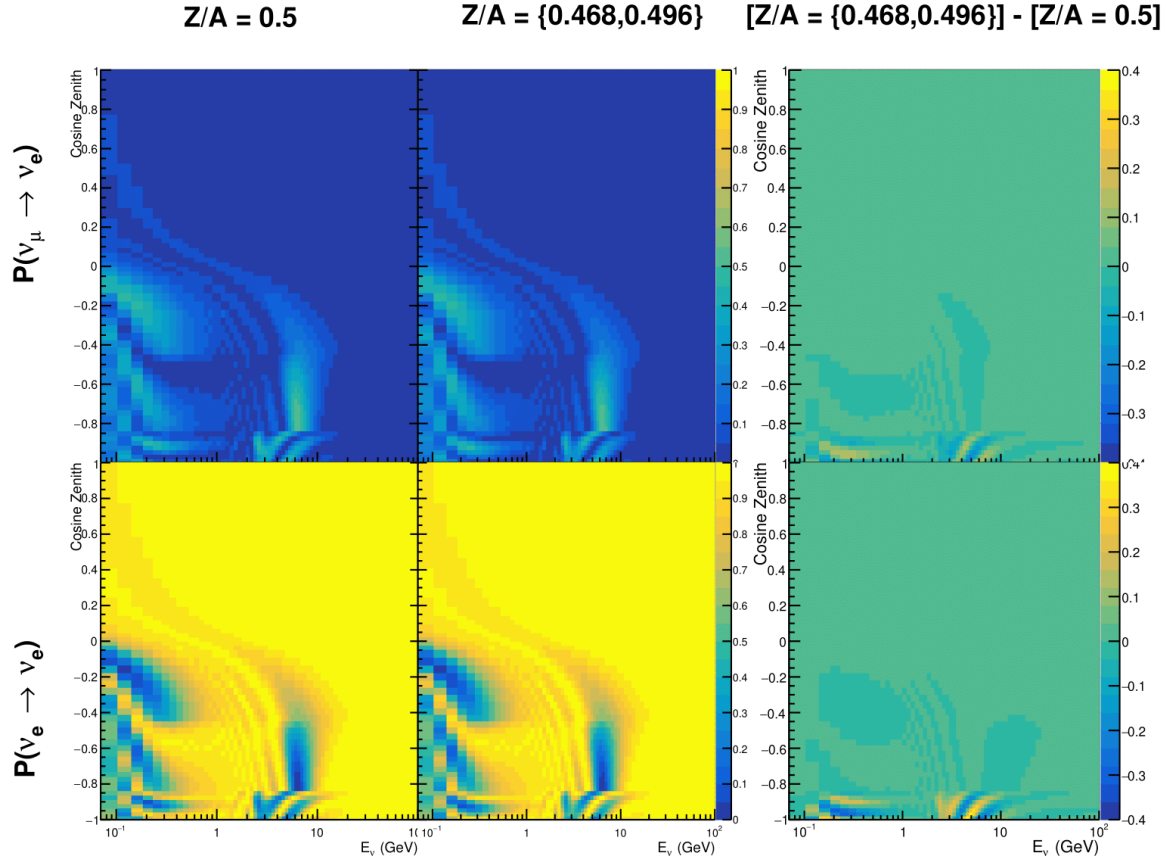


Figure 4.14: The oscillation probability, $P(\nu_\mu \rightarrow \nu_e)$ (top row) and $P(\nu_e \rightarrow \nu_\mu)$ (bottom row), given as a function of neutrino energy and zenith angle. The left column gives probabilities where the constant $Z/A = 0.5$ approximation which is used in the official SK-only analysis. The middle column gives the probabilities where the more accurate $Z/A = [0.468, 0.498]$ values as given in Table 4.2. The right column illustrates the difference in oscillation probability between the two different techniques.

1850 where t_i are the intersection points between each layer and t is the path length of
 1851 the trajectory across the layer which is dependent upon $\cos(\theta_Z)$.

1852 The oscillation probability calculation speed is approximately linear in the number
 1853 of layers invoked within the Earth model. Therefore a four-layer model is still utilized
 1854 with the only difference to the above example being that the four-layer model used for
 1855 each value of $\cos(\theta_Z)$ is different. Following the method outlined in [191], a four-layer
 1856 piecewise quadratic polynomial is fit to the PREM model for the four layers defined in

1857 Table 4.2. This fit was not performed by the author of the thesis and is documented
1858 in [192]. The coefficients of the quadratic fit to each layer are given in Table 4.3 with
1859 the final distribution illustrated in Figure 4.15. The quadratic approximation is clearly
1860 much closer to the PREM model as compared to the constant density approximation.

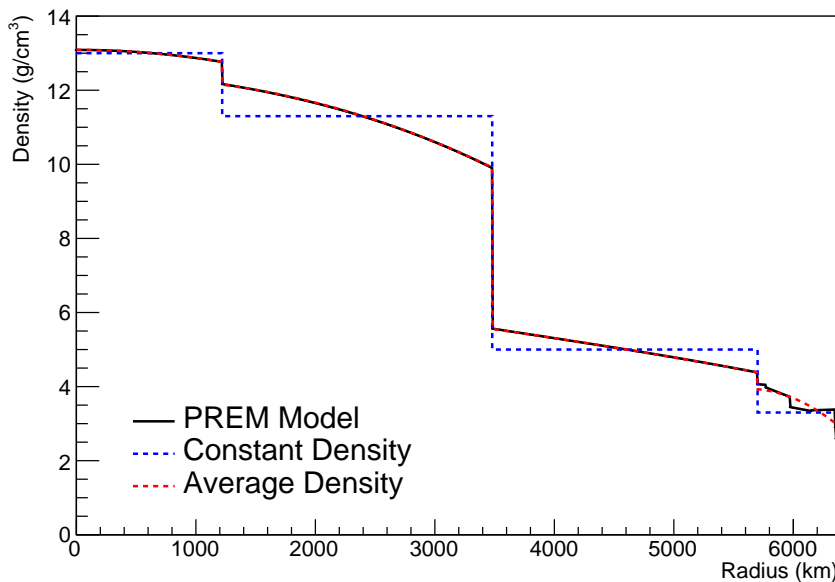


Figure 4.15: The density of the Earth given as a function of the radius, as given by the PREM model (Black), the constant density four-layer approximation (Blue), as used in the official SK-only analysis, and the quadratic approximation of the PREM model (Red).

| Layer | Outer Radius [km] | Density [g/cm ³] |
|-----------------|-------------------|-------------------------------|
| Inner Core | 1220 | $13.09 - 8.84x^2$ |
| Outer Core | 3480 | $12.31 + 1.09x - 10.02x^2$ |
| Lower Mantle | 5701 | $6.78 - 1.56x - 1.25x^2$ |
| Transition Zone | 6371 | $-50.42 + 123.33x - 69.95x^2$ |

Table 4.3: The quadratic polynomial fits to the PREM model for four assumed layers of the PREM model. The fit to calculate the coefficients is given in [192], where $x = R/R_{Earth}$.

1861 The effect of using the average density per $\cos(\theta_Z)$ model is highlighted in Fig-
1862 ure 4.16. The slight discontinuity in the oscillation probability around $\cos(\theta_Z) \sim -0.45$
1863 in the fixed density model, which is due to the transition to mantle layer boundary, has

₁₈₆₄ been reduced. This is expected as the difference in the density across this boundary is
₁₈₆₅ significantly smaller in the average density model as compared to the constant density
₁₈₆₆ model. Whilst the difference in density across the other layer transitions is reduced,
₁₈₆₇ there is still a significant difference. This means the discontinuities in the oscillation
₁₈₆₈ probabilities remain but are significantly reduced. However, as the average density
₁₈₆₉ approximation matches the PREM model well in this region, these discontinuities are
₁₈₇₀ due to the Earth model rather than an artifact of the oscillation calculation.

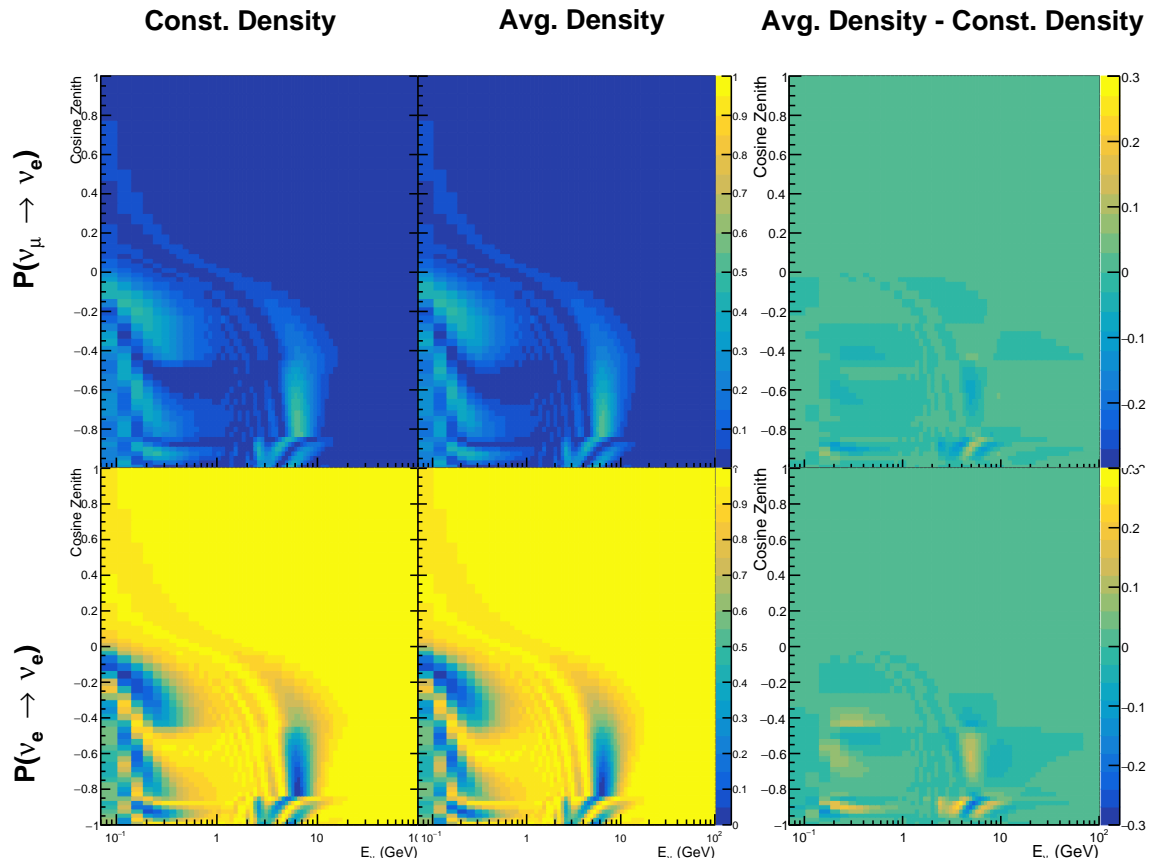


Figure 4.16: The oscillation probability, $P(\nu_\mu \rightarrow \nu_e)$ (top row) and $P(\nu_e \rightarrow \nu_\mu)$ (bottom row), given as a function of neutrino energy and zenith angle. The left column gives probabilities where the four-layer constant density approximation is used. The middle column gives the probabilities where the density is integrated over the trajectory, using the quadratic PREM approximation, for each $\cos(\theta_Z)$ is used. The right column illustrates the difference in oscillation probability between the two different techniques.

¹⁸⁷¹ 4.5 Production Height Averaging

¹⁸⁷² As discussed in section 4.1, the height at which the cosmic ray flux interacts in the
¹⁸⁷³ atmosphere is not known on an event-by-event basis. The production height can
¹⁸⁷⁴ vary from the Earth's surface to 50km above that. The SK-only analysis methodol-
¹⁸⁷⁵ ogy (described in section 4.2) for including the uncertainty on the production height
¹⁸⁷⁶ is to include variations from the Honda model when pre-calculating the oscillation
¹⁸⁷⁷ probabilities prior to the fit. This technique is not possible for this analysis which
¹⁸⁷⁸ uses continuous oscillation parameters that can not be known prior to the fit. Conse-
¹⁸⁷⁹ quently, an analytical averaging technique was developed in [192]. The author of this
¹⁸⁸⁰ thesis was not responsible for the derivation of the technique but has performed the
¹⁸⁸¹ implementation and validation of the technique for this analysis alone.

¹⁸⁸² The oscillation probability used within this analysis is based on [20]. The neutrino
¹⁸⁸³ wavefunction in the vacuum Hamiltonian evolves in each layer of constant matter
¹⁸⁸⁴ density via

$$i \frac{d\psi_j(t)}{dt} = \frac{m_j^2}{2E_\nu} \psi_j(t) - \sum_k \sqrt{2} G_F N_e U_{ej} U_{ke}^\dagger \psi_k(t), \quad (4.6)$$

¹⁸⁸⁵ where m_j^2 is the square of the j^{th} vacuum eigenstate mass, E_ν is the neutrino energy,
¹⁸⁸⁶ G_F is Fermi's constant, N_e is the electron number density and U is the PMNS matrix.
¹⁸⁸⁷ $N_e \rightarrow -N_e$ and $\delta_{CP} \rightarrow -\delta_{CP}$ for antineutrino propagation.

¹⁸⁸⁸ Using the 20 production heights per MC neutrino event, provided as 5% percentiles
¹⁸⁸⁹ from the Honda flux model, a production height distribution $p_j(h|E_\nu, \cos \theta_Z)$ is built
¹⁸⁹⁰ for each neutrino flavour $j = \nu_e, \bar{\nu}_e, \nu_\mu, \bar{\nu}_\mu$. In practice, a histogram is filled with 20
¹⁸⁹¹ evenly spaced bins in production height h between 0 and 50km. The neutrino energy

1892 and cosine zenith binning is the same as that provided in section 4.2. The average
1893 production height, $\bar{h} = \int dh \frac{1}{4} \sum_j p_j(h|E_\nu, \cos(\theta_Z))$, is calculated. The production height
1894 binning of this histogram is then translated into $\delta t(h) = t(z, \bar{h}) - t(z, h)$, where $t(z, h)$
1895 is the distance travelled along the trajectory.

1896 For the i^{th} traversed layer, the transition amplitude, $D_i(t_{i+1}, t_i)$, is computed. The
1897 time ordered product of these is then used as the overall transition amplitude via

$$A(t_{n+1}, t_0) = D_n(t_{n+1}, t_n) \dots D_1(t_2, t_1) D_0(t_1, t_0), \quad (4.7)$$

1898 where,

$$\begin{aligned} D_n(t_{n+1}, t_n) &= \exp[-iH_n(t_{n+1} - t_n)] \\ &= \sum_{k=1}^3 C_k \exp[ia_k \delta t] \end{aligned} \quad (4.8)$$

1899 is expressed as a diagonalised time-dependent solution to the schrodinger equation.
1900 The 0^{th} layer is the propagation through the atmosphere and is the only term which
1901 depends on the production height. Using the subsitution $t_0 = t(\bar{h}) - \delta t(h)$, it can be
1902 shown that

$$D_0(t_1, t_0) = D_0(t_1, \bar{h}) D_0(\delta t). \quad (4.9)$$

1903 Thus Equation 4.7 becomes

$$\begin{aligned}
A(t_{n+1}, t_0) &= D_n(t_{n+1}, t_n) \dots D_1(t_2, t_1) D_0(t_1, \bar{h}) D(\delta t) \\
&= A(t_{n+1}, \bar{h}) \sum_{k=1}^3 C_k \exp[i a_k \delta t], \\
&= \sum_{k=1}^3 B_k \exp[i a_k \delta t].
\end{aligned} \tag{4.10}$$

¹⁹⁰⁴ The oscillation probability averaged over production height is calculated as

$$\begin{aligned}
\bar{P}(\nu_j \rightarrow \nu_i) &= \int d(\delta t) p_j(\delta t | E_\nu, \cos \theta_Z) P(\nu_j \rightarrow \nu_i) \\
&= \int d(\delta t) p_j(\delta t | E_\nu, \cos \theta_Z) A(t_{n+1}, t_0) A^*(t_{n+1}, t_0) \\
&= \sum_{km} (B_k)_{ij} (B_m)_{ij}^* \int d(\delta t) p_j(\delta t | E_\nu, \cos \theta_Z) \exp[i(a_k - a_m)\delta t]
\end{aligned} \tag{4.11}$$

¹⁹⁰⁵ In practice, implementation in CUDAProb3 [185] is relatively straightforward as
¹⁹⁰⁶ the majority of these terms are already calculated in the standard oscillation calculation.
¹⁹⁰⁷ Figure 4.17 illustrates the results of the production height averaging. As expected,
¹⁹⁰⁸ the main effect is observed in the low-energy downward-going and horizontal-going
¹⁹⁰⁹ events. Upward-going events have to travel the radius of the Earth, $R_E = 6371\text{km}$,
¹⁹¹⁰ where the production height uncertainty is a small fraction of the total path length.

¹⁹¹¹

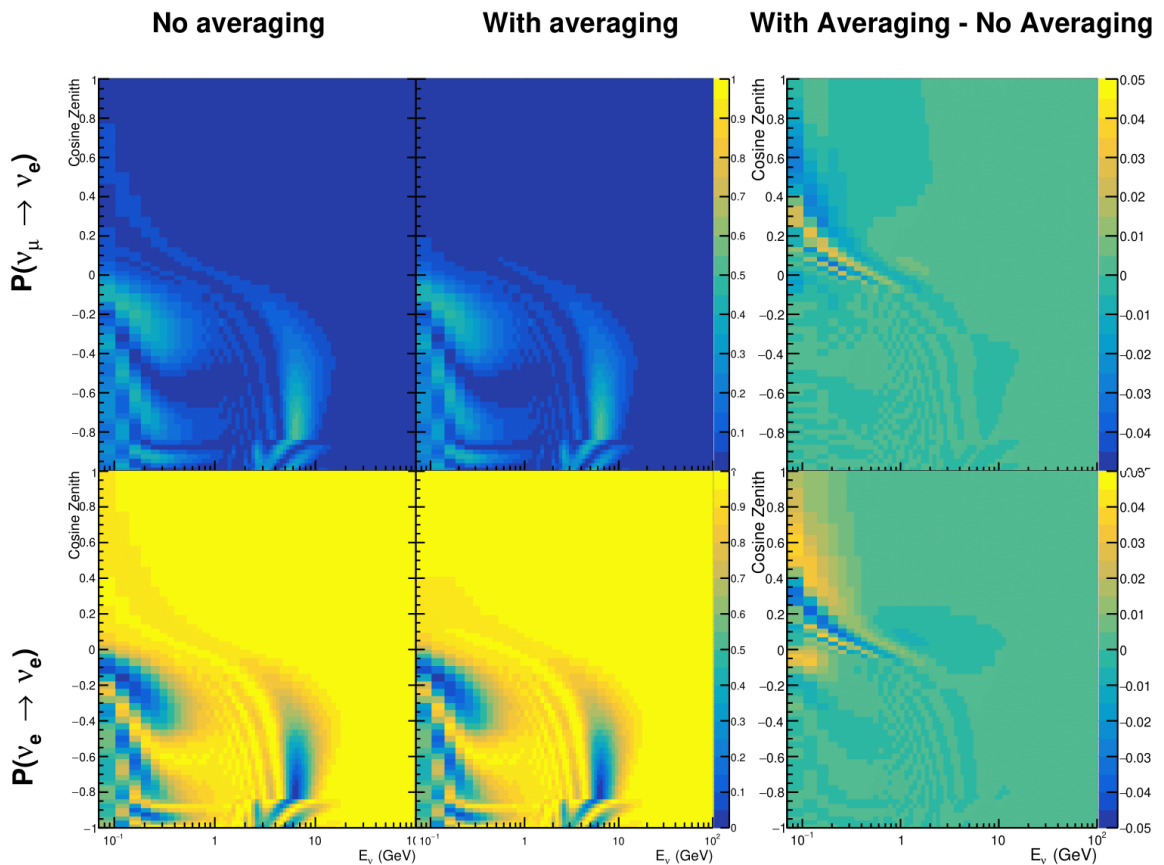


Figure 4.17: The oscillation probability, $P(\nu_\mu \rightarrow \nu_e)$ (top row) and $P(\nu_e \rightarrow \nu_e)$ (bottom row), given as a function of neutrino energy and zenith angle. The left column gives probabilities where a fixed production height of 25km is used. The middle column gives the probabilities where the production height is analytically averaged. The right column illustrates the difference in oscillation probability between the two different techniques.

¹⁹¹² Bibliography

- ¹⁹¹³ [1] J. Chadwick, Verhandl. Dtsc. Phys. Ges. **16**, 383 (1914).
- ¹⁹¹⁴ [2] C. D. Ellis and W. A. Wooster, Proc. R. Soc. Lond. A Math. Phys. Sci. **117**, 109 (1927).
- ¹⁹¹⁶ [3] W. Pauli, Phys. Today **31N9**, 27 (1978).
- ¹⁹¹⁷ [4] E. Fermi, Z. Phys. **88**, 161 (1934).
- ¹⁹¹⁸ [5] F. Reines and C. L. Cowan, Phys. Rev. **92**, 830 (1953).
- ¹⁹¹⁹ [6] C. L. Cowan, F. Reines, F. B. Harrison, H. W. Kruse, and A. D. McGuire, Science **124**, 103 (1956), <http://science.sciencemag.org/content/124/3212/103.full.pdf>.
- ¹⁹²¹ [7] G. Danby *et al.*, Phys. Rev. Lett. **9**, 36 (1962).
- ¹⁹²² [8] K. Kodama *et al.*, Physics Letters B **504**, 218 (2001).
- ¹⁹²³ [9] LSND, A. Aguilar-Arevalo *et al.*, Phys. Rev. **D64**, 112007 (2001), hep-ex/0104049.
- ¹⁹²⁴ [10] MiniBooNE Collaboration, A. A. Aguilar-Arevalo *et al.*, Phys. Rev. Lett. **110**, 161801 (2013).
- ¹⁹²⁶ [11] Planck Collaboration *et al.*, aap **641** (2020).
- ¹⁹²⁷ [12] B. Pontecorvo, Sov. Phys. JETP **26**, 984 (1968), [Zh. Eksp. Teor. Fiz. 53, 1717 (1967)].
- ¹⁹²⁸ [13] B. Pontecorvo, Sov. Phys. JETP **7**, 172 (1958), [Zh. Eksp. Teor. Fiz. 34, 247 (1957)].
- ¹⁹²⁹ [14] M. Kobayashi and T. Maskawa, Progress of Theoretical Physics **49**, 652 (1973).
- ¹⁹³⁰ [15] N. Cabibbo, Phys. Rev. Lett. **10**, 531 (1963).
- ¹⁹³¹ [16] A. M. and, Journal of Physics: Conference Series **587**, 012030 (2015).
- ¹⁹³² [17] A. Y. Smirnov, (2003).
- ¹⁹³³ [18] S. Mikheyev and A. Smirnov, Soviet Journal of Nuclear Physics **42**, 913 (1985).
- ¹⁹³⁴ [19] L. Wolfenstein, Phys. Rev. D **17**, 2369 (1978).
- ¹⁹³⁵ [20] V. D. Barger, K. Whisnant, S. Pakvasa, and R. J. N. Phillips, Phys. Rev. D **22**, 2718 (1980).

- ¹⁹³⁷ [21] The Super-Kamiokande Collaboration, Y. Ashie *et al.*, Phys. Rev. Lett. **93**, 101801 (2004).
- ¹⁹³⁸
- ¹⁹³⁹ [22] SNO Collaboration, Q. R. Ahmad *et al.*, Phys. Rev. Lett. **89**, 011301 (2002).
- ¹⁹⁴⁰ [23] 2015 Nobel prize in Physics as listed by Nobelprize.org, https://www.nobelprize.org/nobel_prizes/physics/laureates/2015/, Accessed: 22-06-2022.
- ¹⁹⁴¹
- ¹⁹⁴²
- ¹⁹⁴³ [24] J. A. Formaggio and G. P. Zeller, Rev. Mod. Phys. **84**, 1307 (2012), 1305.7513.
- ¹⁹⁴⁴ [25] A. Bellerive, Int. J. Mod. Phys. A **19**, 1167 (2004).
- ¹⁹⁴⁵ [26] R. Davis, D. S. Harmer, and K. C. Hoffman, Phys. Rev. Lett. **20**, 1205 (1968).
- ¹⁹⁴⁶ [27] N. Vinyoles *et al.*, Astrophys. J. **835**, 202 (2017).
- ¹⁹⁴⁷ [28] V. Gribov and B. Pontecorvo, Phys. Lett. B **28**, 493 (1969).
- ¹⁹⁴⁸ [29] K. S. Hirata *et al.*, Phys. Rev. Lett. **63**, 16 (1989).
- ¹⁹⁴⁹ [30] W. Hampel *et al.*, Phys. Lett. B **447**, 127 (1999).
- ¹⁹⁵⁰ [31] SAGE Collaboration, J. N. Abdurashitov *et al.*, Phys. Rev. C **60**, 055801 (1999).
- ¹⁹⁵¹ [32] Q. R. Ahmad *et al.*, Phys. Rev. Lett. **89** (2002).
- ¹⁹⁵² [33] Borexino Collaboration, Nature **562**, 505 (2018).
- ¹⁹⁵³ [34] B. Aharmim *et al.*, Astrophys. J. **653**, 1545 (2006).
- ¹⁹⁵⁴ [35] M. Agostini *et al.*, (2020).
- ¹⁹⁵⁵ [36] S. Andringa *et al.*, Adv. High Energy Phys. **2016**, 1 (2016).
- ¹⁹⁵⁶ [37] J. F. Beacom *et al.*, Chin. phys. C **41**, 023002 (2017).
- ¹⁹⁵⁷ [38] F. An *et al.*, J. Phys. G Nucl. Part. Phys. **43**, 030401 (2016).
- ¹⁹⁵⁸ [39] J. Aalbers *et al.*, (2020), 2006.03114.
- ¹⁹⁵⁹ [40] T. K. Gaisser and M. Honda, (2002).
- ¹⁹⁶⁰ [41] G. D. Barr, T. K. Gaisser, P. Lipari, S. Robbins, and T. Stanev, Physical Review D **70** (2004).
- ¹⁹⁶¹
- ¹⁹⁶² [42] M. Honda, T. Kajita, K. Kasahara, S. Midorikawa, and T. Sanuki, Physical Review

- 1963 D **75** (2007).
- 1964 [43] M. Honda, T. Kajita, K. Kasahara, and S. Midorikawa, Phys. Rev. D **70**, 043008 (2004).
- 1965
- 1966 [44] M. Honda, T. Kajita, K. Kasahara, and S. Midorikawa, Phys. Rev. D **83**, 123001 (2011).
- 1967
- 1968 [45] A. Fasso, A. Ferrari, P. R. Sala, and J. Ranft, (2001).
- 1969 [46] Y. Ashie *et al.*, Physical Review D **71** (2005).
- 1970 [47] F. Reines *et al.*, Phys. Rev. Lett. **15**, 429 (1965).
- 1971 [48] D. Casper *et al.*, Phys. Rev. Lett. **66**, 2561 (1991).
- 1972 [49] K. S. Hirata *et al.*, Phys. Lett. B **280**, 146 (1992).
- 1973 [50] Z. Li *et al.*, Physical Review D **98** (2018).
- 1974 [51] Kamiokande Collaboration *et al.*, (2017).
- 1975 [52] T2K Collaboration, Nature **580**, 339 (2020).
- 1976 [53] M. A. Acero *et al.*, Phys. Rev. Lett. **123**, 151803 (2019).
- 1977 [54] M. G. Aartsen *et al.*, Phys. Rev. Lett. **120** (2018).
- 1978 [55] P. Adamson *et al.*, Phys. Rev. Lett. **112** (2014).
- 1979 [56] M. S. Athar *et al.*, Progress in Particle and Nuclear Physics **124**, 103947 (2022).
- 1980 [57] G. Danby *et al.*, Phys. Rev. Lett. **9**, 36 (1962).
- 1981 [58] K. Abe *et al.*, Physical Review D **87** (2013).
- 1982 [59] MINOS Collaboration, D. G. Michael *et al.*, Phys. Rev. Lett. **97**, 191801 (2006).
- 1983 [60] G. Danby *et al.*, Phys. Rev. Lett. **9**, 36 (1962).
- 1984 [61] NOvA Collaboration, M. A. Acero *et al.*, Phys. Rev. Lett. **123**, 151803 (2019).
- 1985 [62] B. Abi, R. Acciarri, M. A. Acero, and G. e. a. Adamov, Eur. Phys. J. C Part. Fields **80** (2020).
- 1986
- 1987 [63] Hyper-Kamiokande Proto-Collaboration *et al.*, Prog. Theor. Exp. Phys. **2015**, 53C02 (2015).
- 1988

- 1989 [64] C. Blanco, D. Hooper, and P. Machado, Physical Review D **101** (2020).
- 1990 [65] MicroBooNE Collaboration *et al.*, Search for an Excess of Electron Neutrino
1991 Interactions in MicroBooNE Using Multiple Final State Topologies, 2021.
- 1992 [66] KARMEN Collaboration, B. Armbruster *et al.*, Phys. Rev. D **65**, 112001 (2002).
- 1993 [67] S.-B. Kim, T. Lasserre, and Y. Wang, Adv. High Energy Phys. **2013**, 1 (2013).
- 1994 [68] M. Sajjad Athar *et al.*, Prog. Part. Nucl. Phys. **124**, 103947 (2022), 2111.07586.
- 1995 [69] K. Abe *et al.*, Nucl. Instrum. Methods Phys. Res. A **1027**, 166248 (2022).
- 1996 [70] F. P. An *et al.*, Phys. Rev. Lett. **108**, 171803 (2012).
- 1997 [71] RENO Collaboration, J. K. Ahn *et al.*, Phys. Rev. Lett. **108**, 191802 (2012).
- 1998 [72] Double Chooz Collaboration, Y. Abe *et al.*, Phys. Rev. Lett. **108**, 131801 (2012).
- 1999 [73] J. Collaboration *et al.*, TAO Conceptual Design Report: A Precision Measurement
2000 of the Reactor Antineutrino Spectrum with Sub-percent Energy Resolution, 2020,
2001 2005.08745.
- 2002 [74] for the RENO Collaboration, New results from RENO and the 5 MeV excess,
2003 AIP Publishing LLC, 2015.
- 2004 [75] Y. Abe *et al.*, Journal of High Energy Physics **2014** (2014).
- 2005 [76] Daya Bay Collaboration, D. Adey *et al.*, Phys. Rev. Lett. **123**, 111801 (2019).
- 2006 [77] M. P. Decowski, Nucl. Phys. B. **908**, 52 (2016).
- 2007 [78] The KamLAND Collaboration, A. Gando *et al.*, Phys. Rev. D **83**, 052002 (2011).
- 2008 [79] Y. Fukuda *et al.*, Phys. Rev. Lett. **81**, 1562 (1998).
- 2009 [80] K. Abe *et al.*, Nuclear Instruments and Methods in Physics Research Section
2010 A: Accelerators, Spectrometers, Detectors and Associated Equipment **737**, 253
2011 (2014).
- 2012 [81] S. Fukuda *et al.*, Nucl. Instrum. Methods Phys. Res. A **501**, 418 (2003).
- 2013 [82] Y. Itow *et al.*, (2001).
- 2014 [83] M. Jiang *et al.*, Prog. Theor. Exp. Phys. **2019** (2019).

- 2015 [84] S. Fukuda *et al.*, Nuclear Instruments and Methods in Physics Research Section
2016 A: Accelerators, Spectrometers, Detectors and Associated Equipment **501**, 418
2017 (2003), <http://www.sciencedirect.com/science/article/pii/S016890020300425X>.
- 2018 [85] Y. Nakano *et al.*, Nucl. Instrum. Methods Phys. Res. A **977**, 164297 (2020).
- 2019 [86] Hamamatsu, Hamamatsu Photonics Photomultiplier Tubes Handbook.
- 2020 [87] K. Abe *et al.*, Nucl. Instrum. Methods Phys. Res. A **1027**, 166248 (2022).
- 2021 [88] J. F. Beacom and M. R. Vagins, Phys. Rev. Lett. **93**, 171101 (2004).
- 2022 [89] L. Marti *et al.*, Nucl. Instrum. Methods Phys. Res. A **959**, 163549 (2020).
- 2023 [90] L. Marti *et al.*, (2019).
- 2024 [91] T. Tanimori *et al.*, IEEE Transactions on Nuclear Science **36**, 497 (1989).
- 2025 [92] Super-Kamiokande Collaboration, J. Hosaka *et al.*, Phys. Rev. D **73**, 112001
2026 (2006).
- 2027 [93] H. Nishino *et al.*, Nucl. Instrum. Methods Phys. Res. A **610**, 710 (2009).
- 2028 [94] S. Yamada *et al.*, IEEE Transactions on Nuclear Science **57**, 428 (2010).
- 2029 [95] S. Yamada, Y. Hayato, Y. Obayashi, and M. Shiozawa, New online system
2030 without hardware trigger for the Super-Kamiokande experiment, in *2007 IEEE*
2031 *Nuclear Science Symposium Conference Record*, IEEE, 2007.
- 2032 [96] G. Carminati, Phys. Procedia **61**, 666 (2015).
- 2033 [97] P. A. Čerenkov, Phys. Rev. **52**, 378 (1937).
- 2034 [98] I. Frank and I. Tamm, Coherent visible radiation of fast electrons passing
2035 through matter, in *Selected Papers*, pp. 29–35, Springer Berlin Heidelberg, Berlin,
2036 Heidelberg, 1991.
- 2037 [99] The T2K Collaboration, KEK Proposal (2001),
2038 <http://neutrino.kek.jp/jhfnu/loi/loi.v2.030528.pdf>.
- 2039 [100] Y. Itow *et al.*, (2001), hep-ex/0106019.
- 2040 [101] The K2K Collaboration and S. H. Ahn, (2001), hep-ex/0103001.
- 2041 [102] The T2K Collaboration, KEK Proposal (2006), <http://j->

- 2042 parc.jp/researcher/Hadron/en/pac_0606/pdf/p11-Nishikawa.pdf.
- 2043 [103] T2K Collaboration, K. Abe *et al.*, Phys. Rev. Lett. **112**, 061802 (2014),
2044 <https://link.aps.org/doi/10.1103/PhysRevLett.112.061802>.
- 2045 [104] NINJA Collaboration, T. Fukuda *et al.*, Proposal for precise measurement of
2046 neutrino-water cross-section in NINJA physics run, Proposal for J-PARC and
2047 KEK, 2017.
- 2048 [105] T. Ovsianikova *et al.*, Physics of Particles and Nuclei **48**, 1014 (2017),
2049 <https://doi.org/10.1134/S1063779617060478>.
- 2050 [106] M. Antonova *et al.*, Journal of Instrumentation **12**, C07028 (2017),
2051 <http://stacks.iop.org/1748-0221/12/i=07/a=C07028>.
- 2052 [107] The T2K Collaboration, K. Abe *et al.*, Phys. Rev. D **102**, 012007 (2020).
- 2053 [108] K. Abe *et al.*, Progress of Theoretical and Experimental Physics **2021** (2021).
- 2054 [109] The T2K Collaboration, K. Abe *et al.*, Nuclear Instruments
2055 and Methods in Physics Research Section A: Accelerators, Spectrometers,
2056 Detectors and Associated Equipment **659**, 106 (2011),
2057 <http://www.sciencedirect.com/science/article/pii/S0168900211011910>.
- 2058 [110] K. Matsuoka *et al.*, Nuclear Instruments and Methods in Physics Research Section
2059 A: Accelerators, Spectrometers, Detectors and Associated Equipment **624**, 591
2060 (2010), <http://www.sciencedirect.com/science/article/pii/S016890021002098X>.
- 2061 [111] K. Abe *et al.*, Phys. Rev. D. **103** (2021).
- 2062 [112] T. Vladislavljevic, *Predicting the T2K neutrino flux and measuring oscillation parameters* Springer theses, 1 ed. (Springer Nature, Cham, Switzerland, 2020).
- 2064 [113] D. Beavis, A. Carroll, and I. Chiang, (1995).
- 2065 [114] P.-A. Amaudruz *et al.*, Nuclear Instruments and Methods in Physics Research
2066 Section A: Accelerators, Spectrometers, Detectors and Associated Equipment
2067 **696**, 1 (2012).
- 2068 [115] N. Abgrall *et al.*, Nuclear Instruments and Methods in Physics Research Section
2069 A: Accelerators, Spectrometers, Detectors and Associated Equipment **637**, 25
2070 (2011).

- 2071 [116] S. Assylbekov *et al.*, Nuclear Instruments and Methods in Physics Research
2072 Section A: Accelerators, Spectrometers, Detectors and Associated Equipment
2073 **686**, 48 (2012).
- 2074 [117] D. Allan *et al.*, Journal of Instrumentation **8**, P10019 (2013).
- 2075 [118] F. Vannucci, Advances in High Energy Physics **2014**, 1 (2014).
- 2076 [119] UA1 magnet sets off for a second new life, 2022.
- 2077 [120] S. Aoki *et al.*, Nuclear Instruments and Methods in Physics Research Section
2078 A: Accelerators, Spectrometers, Detectors and Associated Equipment **698**, 135
2079 (2013).
- 2080 [121] M. Yokoyama *et al.*, Nuclear Instruments and Methods in Physics Research
2081 Section A: Accelerators, Spectrometers, Detectors and Associated Equipment
2082 **622**, 567 (2010).
- 2083 [122] K. Suzuki *et al.*, Progress of Theoretical and Experimental Physics **2015**, 53C01
2084 (2015).
- 2085 [123] S. Brooks, A. Gelman, G. L. Jones, and X.-L. Meng, *Handbook of Markov Chain
2086 Monte Carlo* (CRC Press, 2011).
- 2087 [124] W. R. Gilks, S. Richardson, and D. J. Spiegelhalter, *Markov Chain Monte Carlo in
2088 Practice* (Chapman & Hall/CRC Interdisciplinary Statistics, 1995).
- 2089 [125] C. Wret, *Minimising systematic uncertainties in the T2K experiment using near-
2090 detector and external data*, PhD thesis, Imperial College London, 2018.
- 2091 [126] K. E. Duffy, *Measurement of the Neutrino Oscillation Parameters $\sin^2 \theta_{23}$, Δm_{32}^2 ,
2092 $\sin^2 \theta_{13}$, and δ_{CP} in Neutrino and Antineutrino Oscillation at T2K*, PhD thesis, Oriel
2093 College, University of Oxford, 2016.
- 2094 [127] T. Bayes, Rev. Phil. Trans. Roy. Soc. Lond. **53**, 370 (1764).
- 2095 [128] N. Metropolis, A. W. Rosenbluth, M. N. Rosenbluth, A. H. Teller, and E. Teller,
2096 Journal of Chemical Physics **21** (1970).
- 2097 [129] W. K. Hastings, Biometrika **57** (1970).
- 2098 [130] J. Dunkley, M. Bucher, P. G. Ferreira, K. Moodley, and C. Skordis, Mon. Not. R.
2099 Astron. Soc. **356**, 925 (2005).

- ²¹⁰⁰ [131] Particle Data Group *et al.*, Prog. Theor. Exp. Phys. **2020** (2020).
- ²¹⁰¹ [132] H. Jeffreys, *The Theory of Probability* Oxford Classic Texts in the Physical Sciences
²¹⁰² (, 1939).
- ²¹⁰³ [133] R. E. Kass and A. E. Raftery, J. Am. Stat. Assoc. **90**, 773 (1995).
- ²¹⁰⁴ [134] T. Böhlen *et al.*, Nuclear Data Sheets **120**, 211 (2014),
²¹⁰⁵ <http://www.sciencedirect.com/science/article/pii/S0090375214005018>.
- ²¹⁰⁶ [135] R. Brun *et al.*, *GEANT: Detector Description and Simulation Tool; Oct 1994*CERN
²¹⁰⁷ Program Library (CERN, Geneva, 1993), <http://cds.cern.ch/record/1082634>,
²¹⁰⁸ Long Writeup W5013.
- ²¹⁰⁹ [136] T2K Collaboration, K. Abe *et al.*, Phys. Rev. D **87**, 012001 (2013).
- ²¹¹⁰ [137] C. Zeitnitz and T. Gabriel, Nuclear Instruments and Methods in Physics Research Section A: Accelerators, Spectrometers, Detectors and Associated Equipment **349**, 106 (1994),
²¹¹¹ <http://www.sciencedirect.com/science/article/pii/0168900294906130>.
- ²¹¹² [138] N. Abgrall *et al.*, Physical Review C **84** (2011).
- ²¹¹³ [139] N. Abgrall *et al.*, Physical Review C **85** (2012).
- ²¹¹⁴ [140] N. Abgrall *et al.*, Nuclear Instruments and Methods in Physics Research Section
²¹¹⁵ A: Accelerators, Spectrometers, Detectors and Associated Equipment **701**, 99
²¹¹⁶ (2013), <http://www.sciencedirect.com/science/article/pii/S016890021201234X>.
- ²¹¹⁷ [141] HARP Collaboration, M. Apollonio *et al.*, Phys. Rev. C **80**, 035208 (2009),
²¹¹⁸ <https://link.aps.org/doi/10.1103/PhysRevC.80.035208>.
- ²¹¹⁹ [142] A. Fiorentini *et al.*, T2K Technical Note **217** (2017).
- ²¹²⁰ [143] B. Blau *et al.*, Nuclear Physics B - Proceedings Supplements **113**, 125 (2002).
- ²¹²¹ [144] S. Haino *et al.*, Physics Letters B **594**, 35 (2004).
- ²¹²² [145] NASA, U.S. Standard Atmosphere, 1976, 1976.
- ²¹²³ [146] S. Roesler, R. Engel, and J. Ranft, The Monte Carlo Event Generator DPMJET-III,
²¹²⁴ in *Advanced Monte Carlo for Radiation Physics, Particle Transport Simulation and*
²¹²⁵ *Applications*, pp. 1033–1038, Springer Berlin Heidelberg, 2001.

- ²¹²⁸ [147] K. Niita *et al.*, Radiation Measurements **41**, 1080 (2006).
- ²¹²⁹ [148] T. Sanuki *et al.*, Physics Letters B **541**, 234 (2002).
- ²¹³⁰ [149] P. Achard *et al.*, Physics Letters B **598**, 15 (2004).
- ²¹³¹ [150] Y. Hayato and L. Pickering, The European Physical Journal Special Topics **230**, 4469 (2021).
- ²¹³²
- ²¹³³ [151] Y. Hayato, Acta Physica Polonica B **40** (2009).
- ²¹³⁴ [152] C. L. Smith, Physics Reports **3**, 261 (1972),
²¹³⁵ <http://www.sciencedirect.com/science/article/pii/0370157372900105>.
- ²¹³⁶ [153] O. Benhar, A. Fabrocini, and S. Fantoni, Nuclear Physics A **497**, 423 (1989).
- ²¹³⁷ [154] R. Bradford, A. Bodek, H. Budd, and J. Arrington, Nuclear Physics B - Proceedings Supplements **159**, 127 (2006),
²¹³⁸ <http://www.sciencedirect.com/science/article/pii/S0920563206005184>,
²¹³⁹ Proceedings of the 4th International Workshop on Neutrino-Nucleus Interactions in the Few-GeV Region.
- ²¹⁴⁰
- ²¹⁴¹
- ²¹⁴² [155] A. A. Aguilar-Arevalo *et al.*, Physical Review D **81** (2010).
- ²¹⁴³ [156] R. Gran, J. Nieves, F. Sanchez, and M. J. V. Vacas, Phys. Rev. D **88**, 113007 (2013),
²¹⁴⁴ <https://link.aps.org/doi/10.1103/PhysRevD.88.113007>.
- ²¹⁴⁵ [157] C. Berger and L. M. Sehgal, Phys. Rev. D **76**, 113004 (2007).
- ²¹⁴⁶ [158] C. Berger and L. M. Sehgal, Phys. Rev. D **79**, 053003 (2009),
²¹⁴⁷ <https://link.aps.org/doi/10.1103/PhysRevD.79.053003>.
- ²¹⁴⁸ [159] T. Sjöstrand, Computer Physics Communications **82**, 74 (1994).
- ²¹⁴⁹ [160] C. Bronner and M. Hartz, Tuning of the Charged Hadrons Multiplicities for Deep
²¹⁵⁰ Inelastic Interactions in NEUT, in *Proceedings of the 10th International Workshop on*
²¹⁵¹ *Neutrino-Nucleus Interactions in Few-GeV Region (NuInt15)*, Journal of the Physical
²¹⁵² Society of Japan, 2016.
- ²¹⁵³ [161] M. Glück, E. Reya, and A. Vogt, The European Physical Journal C **5**, 461 (1998).
- ²¹⁵⁴ [162] A. Bodek and U.-k. Yang, Axial and Vector Structure Functions for Electron- and
²¹⁵⁵ Neutrino- Nucleon Scattering Cross Sections at all Q^2 using Effective Leading
²¹⁵⁶ order Parton Distribution Functions, 2010.

- ²¹⁵⁷ [163] A. Bodek and U.-K. Yang, (2010).
- ²¹⁵⁸ [164] S. Gollapinni, (2016).
- ²¹⁵⁹ [165] E. S. P. Guerra *et al.*, Phys. Rev. D **99**, 052007 (2019).
- ²¹⁶⁰ [166] GEANT4, S. Agostinelli *et al.*, Nucl. Instrum. Meth. **A506**, 250 (2003).
- ²¹⁶¹ [167] R. Brun, F. Bruyant, M. Maire, A. C. McPherson, and P. Zanarini, (1987).
- ²¹⁶² [168] K. Abe *et al.*, Physical Review Letters **121** (2018).
- ²¹⁶³ [169] K. Abe *et al.*, Physical Review D **91** (2015).
- ²¹⁶⁴ [170] R. Patterson *et al.*, Nuclear Instruments and Methods in Physics Research Section A: Accelerators, Spectrometers, Detectors and Associated Equipment **608**, 206 (2009).
- ²¹⁶⁷ [171] e. a. S. Berkman, T2K Technical Note **146** (2013).
- ²¹⁶⁸ [172] e. a. A. Himmel, T2K Technical Note **219** (2015).
- ²¹⁶⁹ [173] F. a. James, (1998), CERN Program Library Long Writeups.
- ²¹⁷⁰ [174] e. a. D. Barrow, T2K Technical Note **326** (2020).
- ²¹⁷¹ [175] A. Maghrabi, A. Aldosari, and M. Almutairi, Advances in Space Research **68**, 2941 (2021).
- ²¹⁷³ [176] Super-Kamiokande Collaboration, K. Abe *et al.*, Phys. Rev. D **97**, 072001 (2018),
²¹⁷⁴ <https://link.aps.org/doi/10.1103/PhysRevD.97.072001>.
- ²¹⁷⁵ [177] Particle Data Group, J. Beringer *et al.*, Phys. Rev. D **86**, 010001 (2012).
- ²¹⁷⁶ [178] Y. N. and, Journal of Physics: Conference Series **888**, 012191 (2017).
- ²¹⁷⁷ [179] M. Jiang, *Study of the neutrino mass hierarchy with the atmospheric neutrino data collected in Super-Kamiokande IV*, PhD thesis, Kyoto University, 2019.
- ²¹⁷⁹ [180] P. Machado, H. Schulz, and J. Turner, Physical Review D **102** (2020).
- ²¹⁸⁰ [181] T2K Collaboration, K. Abe *et al.*, Phys. Rev. Lett. **112**, 181801 (2014).
- ²¹⁸¹ [182] R. Wendell, *Three Flavor Oscillation Analysis of Atmospheric Neutrinos in Super-Kamiokande*, PhD thesis, University of North Carolina, 2008.

- ²¹⁸³ [183] R. G. Calland, A. C. Kaboth, and D. Payne, **9**, P04016 (2014).
- ²¹⁸⁴ [184] R. Wendell, <http://www.phy.duke.edu/raw22/public/Prob3++/>.
- ²¹⁸⁵ [185] F. Kallenborn, C. Hundt, S. Böser, and B. Schmidt, Computer Physics Communications **234**, 235 (2019).
- ²¹⁸⁶
- ²¹⁸⁷ [186] L. Warsame, MaCh3 Analysis Progress.
- ²¹⁸⁸ [187] A. M. Dziewonski and D. L. Anderson, Phys. Earth Planet. Inter. **25**, 297 (1981).
- ²¹⁸⁹ [188] S. Bourret, J. A. B. Coelho, and V. V. E. and, Journal of Physics: Conference Series **888**, 012114 (2017).
- ²¹⁹⁰
- ²¹⁹¹ [189] C. Rott, A. Taketa, and D. Bose, Scientific Reports **5** (2015).
- ²¹⁹² [190] K. Hagiwara, N. Okamura, and K. ichi Senda, Journal of High Energy Physics **2011** (2011).
- ²¹⁹³
- ²¹⁹⁴ [191] D. Typinski, Earth Gravity, <http://www.typnet.net/Essays/EarthGravGraphics/EarthGrav.pdf>, Accessed: 24-06-2022.
- ²¹⁹⁵
- ²¹⁹⁶ [192] e. a. D. Barrow, T2K Technical Note **425** (2022).

²¹⁹⁷ List of Figures

| | | |
|---------------------|---|----|
| ²¹⁹⁸ 1.1 | The cross-section of neutrinos from various natural and man-made sources as a function of neutrino energy. Taken from [24] | 10 |
| ²²⁰⁰ 1.2 | The solar neutrino flux as a function of neutrino energy for various fusion reactions and decay chains as predicted by the Standard Solar Model. Taken from [25]. | 11 |
| ²²⁰³ 1.3 | Left panel: The atmospheric neutrino flux for different neutrino flavours as a function of neutrino energy as predicted by the 2007 Honda model (“This work”) [42], the 2004 Honda model (“HKKM04”) [43], the Bartol model [41] and the FLUKA model [45]. Right panel: The ratio of the muon to electron neutrino flux as predicted by all the quoted models. Both figures taken from [42]. | 13 |
| ²²⁰⁹ 1.4 | A diagram illustrating the definition of zenith angle as used in the Super Kamiokande experiment [46]. | 13 |
| ²²¹¹ 1.5 | Prediction of $\nu_e, \bar{\nu}_e, \nu_\mu, \bar{\nu}_\mu$ fluxes as a function of zenith angle as calculated by the HKKM model [44]. The left, middle and right panels represent three values of neutrino energy, 0.32GeV, 1.0GeV and 3.2GeV respectively. Predictions for other models including Bartol [41], Honda [42] and FLUKA [45] are given in [46]. | 14 |
| ²²¹⁶ 1.6 | Constraints on the atmospheric oscillation parameters, $\sin^2(\theta_{23})$ and Δm_{23}^2 , from atmospheric and long baseline experiments: SK [51], T2K [52], NO ν A [53], IceCube [54] and MINOS [55]. Figure taken from [56]. | 15 |
| ²²¹⁹ 1.7 | Reactor electron antineutrino fluxes for ^{235}U (Black), ^{238}U (Green), ^{239}Pu (Purple), and ^{241}Pu (Orange) isotopes. The inverse β -decay cross-section (Blue) and corresponding measurable neutrino spectrum (Red) are also given. Top panel: Schematic of Inverse β -decay interaction including the eventual capture of the emitted neutron. This capture emits a γ -ray which provides a second signal of the event. Taken from [68]. | 18 |
| ²²²⁵ 1.8 | A schematic diagram of the Super-Kamiokande Detector. Taken from [82]. | 22 |

| | | | |
|------|------|--|----|
| 2226 | 1.9 | The location of “standard PMTs” (red) inside the SK detector. Taken from [80]. | 25 |
| 2227 | | | |
| 2228 | 1.10 | Schematic view of the data flow through the data acquisition and online system. Taken from [94]. | 29 |
| 2229 | | | |
| 2230 | 1.11 | The cross-section view of the Tokai to Kamioka experiment illustrating the beam generation facility at J-PARC, the near detector situated at a baseline of 280m and the Super Kamiokande far detector situated 295km from the beam target. | 32 |
| 2231 | | | |
| 2232 | | | |
| 2233 | | | |
| 2234 | 1.12 | The near detector suite for the T2K experiment showing the ND280 and INGRID detectors. The distance between the detectors and the beam target is 280m. | 33 |
| 2235 | | | |
| 2236 | | | |
| 2237 | 1.13 | Top panel: Bird’s eye view of the most relevant part of primary and secondary beamline used within the T2K experiment. The primary beamline is the main-ring proton synchrotron, kicker magnet, and graphite target. The secondary beamline consists of the three focusing horns, decay volume, and beam dump. Figure taken from [109]. Bottom panel: The side-view of the secondary beamline including the focusing horns, beam dump and neutrino detectors. Figure taken from [110]. | 35 |
| 2238 | | | |
| 2239 | | | |
| 2240 | | | |
| 2241 | | | |
| 2242 | | | |
| 2243 | | | |
| 2244 | 1.14 | The Monte Carlo prediction of the energy spectrum for each flavour of neutrino (ν_e , $\bar{\nu}_e$, ν_μ and $\bar{\nu}_\mu$) in the neutrino dominated beam FHC mode (Left) and antineutrino dominated beam RHC mode (Right) expected at SK. Taken from [111]. | 36 |
| 2245 | | | |
| 2246 | | | |
| 2247 | | | |
| 2248 | 1.15 | Top panel: T2K muon neutrino disappearance probability as a function of neutrino energy. Middle panel: T2K electron neutrino appearance probability as a function of neutrino energy. Bottom panel: The neutrino flux distribution for three different off-axis angles (Arbitrary units) as a function of neutrino energy. | 38 |
| 2249 | | | |
| 2250 | | | |
| 2251 | | | |
| 2252 | | | |
| 2253 | 1.16 | The components of the ND280 detector. The neutrino beam travels from left to right. Taken from [109]. | 39 |
| 2254 | | | |
| 2255 | 1.17 | Comparison of data to Monte Carlo prediction of integrated deposited energy as a function of track length for particles that stopped in FGD1. Taken from [114]. | 40 |
| 2256 | | | |
| 2257 | | | |

| | | |
|------|--|----|
| 2258 | 1.18 Schematic design of a Time Projection Chamber detector. Taken from [115]. | 42 |
| 2259 | 1.19 The distribution of energy loss as a function of reconstructed momentum for charged particles passing through the TPC, comparing data to Monte Carlo prediction. Taken from [115]. | 42 |
| 2260 | | |
| 2261 | | |
| 2262 | 1.20 A schematic of the P0D side-view. Taken from [116]. | 43 |
| 2263 | 1.21 Left panel: The Interactive Neutrino GRID on-axis Detector. 14 modules are arranged in a cross-shape configuration, with the center modules being directly aligned with the on-axis beam. Right panel: The layout of a single module of the INGRID detector. Both figures are recreated from [109]. | 46 |
| 2264 | | |
| 2265 | | |
| 2266 | | |
| 2267 | | |
| 2268 | 2.1 Example of using Monte Carlo techniques to find the area under the blue line. The gradient and intercept of the line are 0.4 and 1.0 respectively. The area found to be under the curve using one thousand samples is 29.9 units. | 51 |
| 2269 | | |
| 2270 | | |
| 2271 | | |
| 2272 | 2.2 The area under a line of gradient 0.4 and intercept 1.0 for the range $0 \leq x \leq 10$ as calculated using Monte Carlo techniques as a function of the number of samples used in each repetition. The analytical solution to the area is 30 units as given by the red line. | 52 |
| 2273 | | |
| 2274 | | |
| 2275 | | |
| 2276 | 2.3 Three MCMC chains, each with a stationary distribution equal to a Gaussian centered at 0 and width 1 (As indicated by the black dotted lines). All of the chains use a Gaussian proposal function but have different widths (or 'step size σ '). The top panel has $\sigma = 0.1$, middle panel has $\sigma = 0.5$ and the bottom panel has $\sigma = 5.0$. | 57 |
| 2277 | | |
| 2278 | | |
| 2279 | | |
| 2280 | | |
| 2281 | 2.4 The log-likelihood from the fit detailed in DB: Link to AsimovA Sensitivity Section as a function of the number of steps accumulated in each fit. Many independent MCMC chains were run in parallel and overlaid on this plot. The red line indicates the 1×10^5 step burn-in period after which the log-likelihood becomes stable. | 58 |
| 2282 | | |
| 2283 | | |
| 2284 | | |
| 2285 | | |

| | | |
|---------------|---|----|
| 2286 2.5 | Left: The two dimensional probability distribution for two correlated parameters x and y . The red distribution shows the two dimensional probability distribution when $0 \leq x \leq 5$. Right: The marginalised probability distribution for the y parameter found when requiring the x to be bound between $-5 \leq x \leq 5$ and $0 \leq x \leq 5$ for the black and red distribution, respectively. | 61 |
| 2292 3.1 | The NEUT prediction of the ν_μ -H ₂ O cross-section overlaid on the T2K ν_μ flux. The charged current (black, solid) and neutral current (black, dashed) inclusive, charged current quasi-elastic (blue, solid), charged current 2p2h (blue, dashed), charged current single pion production (pink), and charged current multi- π and DIS (Purple) cross-sections are illustrated. Taken from [150]. | 67 |
| 2298 3.2 | Illustration of the various processes which a pion can undergo before exiting the nucleus. Taken from [164]. | 69 |
| 2300 3.3 | Event displays from Super Kamiokande illustrating the “crisp” ring from a muon and the typically “fuzzier” electron ring. Each pixel represents a PMT and the color scheme denotes the accumulated charge deposited on that PMT. Figures taken from [172]. | 71 |
| 2304 3.4 | The electron/muon PID separation parameter for all sub-GeV single-ring events in SK-IV. The charged current (CC) component is broken down in four flavours of neutrino ($\nu_\mu, \bar{\nu}_\mu, \nu_e$ and $\bar{\nu}e$). Events with positive values of the parameter are determined to be electron-like. | 75 |
| 2308 3.5 | The variation of the measured dark rate as a function of date, broken down by PMT type. The SK-IV and SK-V periods span September 2008 to May 2018 and January 2019 to July 2020 respectively. The break in measurement between 2018 corresponds to the period of tank repair and refurbishment. Figure adapted from [174]. | 77 |
| 2313 3.6 | Comparison of the measured raw charge deposited per event from the stopping muon data samples between SK-IV (Blue) and SK-V (Red), split by the primary muon subevent and the associated decay electron subevent. | 78 |

| | | |
|------|---|----|
| 2317 | 3.7 The distribution of the reconstructed momentum from the muon ring divided by the distance between the reconstructed muon and decay elec- tron vertices as found in the stopping muon data sets of SK-IV (Black) and SK-IV (Red). Only events with one tagged decay electron and con- sidered. A Gaussian fit is considered in the range [2.0, 2.4] MeV/cm and illustrated as the solid curve. | 79 |
| 2323 | 3.8 The χ^2 difference between the SK-IV and SK-V reconstructed muon momentum divided by range when the SK-V is modified by the scaling parameter α . Both additive (Blue) and multiplicative (Black) scaling factors have been considered. In practice, the additive scaling factor actually uses the value of $(\alpha - 1.0)$ | 80 |
| 2329 | 3.9 A depiction of the topology patterns for fully-contained (FC), partially- contained (PC) and up-going muon (Up- μ) samples included in this analysis. | 81 |
| 2335 | 3.10 The predicted neutrino flux of the fully contained (FC) sub-GeV and multi-GeV, partially contained (PC) and upward-going muon (Up- μ) events. The prediction is broken down by the $\nu_x \rightarrow \nu_e$ prediction (top left), $\nu_x \rightarrow \nu_\mu$ prediction (top right) and $\nu_x \rightarrow \nu_\tau$ prediction (bottom). All systematic dials are set to their nominal values and the Asimov A oscillation parameters are assumed. | 83 |
| 2342 | 4.1 An “Oscillogram” that depicts the $P(\nu_\mu \rightarrow \nu_e)$ oscillation probability as a function of neutrino energy and cosine of the zenith angle. The zenith angle is defined such that $\cos(\theta_Z) = 1.0$ represents neutrinos that travel from directly above the detector. The four-layer constant density PREM model approximation is used and Asimov A oscillation parameters are assumed. | 87 |
| 2348 | 4.2 The effect of δ_{CP} for atmospheric neutrinos given in terms of the neu- trino energy and zenith angle. The oscillogram compares the $P(\nu_\mu \rightarrow \nu_e)$ oscillation probability for a CP conserving ($\delta_{CP} = 0.0$) and CP violating ($\delta_{CP} = -1.601$) value of δ_{CP} . The other oscillation parameters assume the “Asimov A” oscillation parameter set given in Table 4.1. | 89 |

| | | |
|---------------|---|----|
| 2348 4.3 | An illustration of the matter-induced effects on the oscillation probability, given as a function of neutrino energy and zenith angle. The top row 2349 of panels gives the $P(\nu_e \rightarrow \nu_e)$ oscillation probability and the bottom 2350 row illustrates the $P(\bar{\nu}_e \rightarrow \bar{\nu}_e)$ oscillation probability. The left column 2351 highlights the oscillation probability in a vacuum, whereas the middle 2352 and right column represents the oscillation probabilities when the four 2353 layer fixed density PREM model is assumed. All oscillation probabilities 2354 assume the “Asimov A” set given in Table 4.1, but importantly, the right 2355 column sets an inverted mass hierarchy. The “matter resonance” effects 2356 at $E_\nu \sim 5\text{GeV}$ can be seen in the $P(\nu_e \rightarrow \nu_e)$ for normal mass hierarchy 2357 and $P(\bar{\nu}_e \rightarrow \bar{\nu}_e)$ for inverted hierarchy. | 90 |
| 2359 4.4 | The oscillation probability for beam neutrino events given as a function 2360 of neutrino energy. All oscillation parameters assume the “Asimov A” 2361 set given in Table 4.1 unless otherwise stated. Each panel represents a 2362 change in one of the oscillation parameters whilst keeping the remaining 2363 parameters fixed. | 91 |
| 2364 4.5 | The number of electron-like events in the FHC and RHC operating 2365 mode of the beam, as a function of the oscillation probabilities. Both 2366 normal hierarchy (Solid) and inverse hierarchy (Dashed) values of 2367 Δm_{23}^2 are given. | 92 |
| 2368 4.6 | The oscillation probability $P(\nu_\mu \rightarrow \nu_e)$, given as a function of neutrino 2369 energy and zenith angle, which highlights an example of the “fast” 2370 oscillations in the sub-GeV upgoing region. | 94 |
| 2371 4.7 | Illustration of the averaging procedure for $N = 2$. The oscillation 2372 probabilities calculated on the finer left binning are averaged to obtain 2373 the oscillation probabilities in the coarser right binning. These averaged 2374 oscillation probabilities with the coarser binning are then applied to 2375 each event during the fit. | 96 |
| 2376 4.8 | Event rate of the SubGeV_elike_0dcy sample as a function of the num- 2377 ber of sub-divisions per coarse bin. Each subplot represents the event 2378 rate of the sample at a different oscillation parameter set (thrown from 2379 the PDG priors). The red line in each subplot represents the mean of the 2380 event rate over the different values of sub-divisions for that particular 2381 oscillation parameter throw. | 98 |

| | | | |
|------|------|---|-----|
| 2382 | 4.9 | Variance of event rate for each atmospheric sample as a function of the number of sub-divisions per coarse bin. The solid red line indicates the 0.1% threshold and the dashed red line is a graphical indication of the variance at a sub-division $N = 10$ | 99 |
| 2386 | 4.10 | Variance of sample likelihood, when compared to ‘Asimov data’ set at Asimov A, for each atmospheric sample as a function of the number of sub-divisions per coarse bin. The solid red line indicates the 0.1% threshold and the dashed red line is a graphical indication of the variance at a sub-division $N = 10$ | 100 |
| 2391 | 4.11 | The oscillation probability, $P(\nu_\mu \rightarrow \nu_e)$ (top row) and $P(\nu_e \rightarrow \nu_e)$ (bottom row), given as a function of neutrino energy and zenith angle. The left column gives the “fine” binning used to calculate the oscillation probabilities and the right column illustrates the “coarse” binning used to reweight the MC events. The fine binning choice is given with $N = 10$, which was determined to be below threshold from Figure 4.9 and Figure 4.10. | 101 |
| 2405 | 4.12 | The calculation time taken to both calculate the oscillation probabilities and fill the “coarse” oscillograms, following the technique given in section 4.2, for the CUDAProb3 and ProbGPU (Red) calculation engines. CUDAProb3 has both a GPU (Blue) and CPU (Black) implementation, where the CPU implementation is multithreaded. Therefore, 8-threads (solid) and 40-threads (dashed) configurations have been used. Prob3, which is a CPU single-thread implementation has a mean step time of 1.142s. | 103 |
| 2406 | 4.13 | The density of the Earth given as a function of the radius, as given by the PREM model (Black) and the constant density four-layer approximation (Blue), as used in the official SK-only analysis. | 104 |

- 2409 4.14 The oscillation probability, $P(\nu_\mu \rightarrow \nu_e)$ (top row) and $P(\nu_e \rightarrow \nu_e)$ (bot-
 2410 tom row), given as a function of neutrino energy and zenith angle.
 2411 The left column gives probabilities where the constant $Z/A = 0.5$
 2412 approximation which is used in the official SK-only analysis. The mid-
 2413 dle column gives the probabilities where the more accurate $Z/A =$
 2414 $[0.468, 0.498]$ values as given in Table 4.2. The right column illustrates
 2415 the difference in oscillation probability between the two different tech-
 2416 niques. 106
- 2417 4.15 The density of the Earth given as a function of the radius, as given by
 2418 the PREM model (Black), the constant density four-layer approxima-
 2419 tion (Blue), as used in the official SK-only analysis, and the quadratic
 2420 approximation of the PREM model (Red). 107
- 2421 4.16 The oscillation probability, $P(\nu_\mu \rightarrow \nu_e)$ (top row) and $P(\nu_e \rightarrow \nu_e)$ (bot-
 2422 tom row), given as a function of neutrino energy and zenith angle. The
 2423 left column gives probabilities where the four-layer constant density ap-
 2424 proximation is used. The middle column gives the probabilities where
 2425 the density is integrated over the trajectory, using the quadratic PREM
 2426 approximation, for each $\cos(\theta_Z)$ is used. The right column illustrates the
 2427 difference in oscillation probability between the two different techniques. 109
- 2428 4.17 The oscillation probability, $P(\nu_\mu \rightarrow \nu_e)$ (top row) and $P(\nu_e \rightarrow \nu_e)$ (bot-
 2429 tom row), given as a function of neutrino energy and zenith angle. The
 2430 left column gives probabilities where a fixed production height of 25km
 2431 is used. The middle column gives the probabilities where the produc-
 2432 tion height is analytically averaged. The right column illustrates the
 2433 difference in oscillation probability between the two different techniques. 113

List of Tables

| | | | |
|------|-----|--|-----|
| 2435 | 1.1 | The various SK periods and respective live-time. The SK-VI live-time is calculated until 1 st April 2022. SK-VII started during the writing of this thesis. | 21 |
| 2438 | 1.2 | The trigger thresholds and extended time windows saved around an event which were utilised throughout the SK-IV period. The exact thresholds can change and the values listed here represent the thresh- olds at the start and end of the SK-IV period. | 30 |
| 2442 | 1.3 | The threshold momentum and energy for a particle to generate Cherenkov light in ultrapure water, as calculated in Equation 1.17 in ultrapure water which has refractive index $n = 1.33$ | 31 |
| 2445 | 2.1 | Jeffreys scale for strength of preference for two models A and B as a function of the calculated Bayes factor ($B_{AB} = B(A/B)$) between the two models [132]. The original scale is given in terms of $\log_{10}(B(A/B))$ but converted to linear scale for easy comparison throughout this thesis. | 63 |
| 2449 | 4.1 | Reference values of the neutrino oscillation parameters for two different oscillation parameter sets. | 92 |
| 2451 | 4.2 | Description of the four layers of the Earth invoked within the average constant density approximation of the PREM model [187]. | 104 |
| 2453 | 4.3 | The quadratic polynomial fits to the PREM model for four assumed layers of the PREM model. The fit to calculate the coefficients is given in [192], where $x = R/R_{Earth}$ | 107 |